Investigating new approaches for mapping groundwater systems in karstic carbonate bedrock: A case study in the Early Silurian formations of the Niagara Escarpment cuesta, southern Ontario, Canada.

by

Elizabeth Haldane Priebe

A thesis
presented to the University of Waterloo
in fulfillment of the
thesis requirement for the degree of
Doctor of Philosophy
in
Earth Sciences

Waterloo, Ontario, Canada, 2019

Examining Committee Membership

The following served on the Examining Committee for this thesis. The decision of the Examining Committee is by majority vote.

External Examiner	NAME: Dr. Ian Clark Title: Professor, Dept. of Earth and Environmental Sciences University of Ottawa
Supervisors	NAME: Dr. David Rudolph Title: Professor and Chair Dept. of Earth and Environmental Sciences NAME: Dr. Richard Jackson Title: Adjunct Professor Dept. of Earth and Environmental Sciences
Internal Member	NAME: Dr. Shaun Frape Title: Professor Dept. of Earth and Environmental Sciences NAME: Dr. Mario Coniglio Title: Professor Dept. of Earth and Environmental Sciences
Internal-external Member	NAME: Dr. James Craig Title: Associate Professor Dept. of Civil and Environmental Engineering
Other Member(s)	NAME: Dr. Richard Amos Title: Adjunct Professor Dept. of Earth and Environmental Sciences

Author's Declaration

I hereby declare that I am the sole author of this thesis. This is a true copy of the thesis, including any required final revisions, as accepted by my examiners.

Abstract

The Ontario Geological Survey conducts geoscience mapping that is designed to support groundwater resource investigations across the province. Recent geological mapping in the Early Silurian carbonate bedrock in southern Ontario has revealed significant geological complexity. Such complexity and the resultant heterogeneity prompted the Ontario Geological Survey to fund this research, which comprises the development of new approaches for improving groundwater characterization in these settings. This research is motivated by the desire to more successfully identify groundwater resource exploration targets and to more effectively map large, regional groundwater flow systems in karstic carbonate bedrock. This thesis is organized in two research themes. The first theme focusses on understanding the spatial relationships between hydraulic conductivity and geology, while the second theme comprises an investigation into geochemical tools and modeling for regional-scale flow systems characterization.

The first challenge that presented itself upon initiation of this research was the poor spatial coverage of hydraulic conductivity values (*K*) relative to the geological heterogeneity of the karstic, carbonate bedrock. Spatial coverage of *K* values for large-scale groundwater investigations is often poor because of the high costs associated with hydraulic testing and the large areas under investigation. Domestic water wells are ubiquitous and their well logs represent an untapped resource of information that includes mandatory specific capacity tests, from which *K* can be estimated. These specific capacity tests are routinely conducted at such low pumping rates that well losses are normally insignificant. In this study, a simple and practical approach to augmenting high-quality *K* values with reconnaissance-level *K* values from water well specific capacity tests was assessed. This assessment was conducted by making comparisons at two different scales: study area-wide (600 km^2) and in a single geological formation within a portion of the study area (200 km^2). Results of the comparisons demonstrate that reconnaissance-level *K* estimates from specific capacity tests approximate the ranges and distributions of the high-quality *K* values. Sufficient detail about the physical basis and assumptions that are invoked in the development of the approach are presented so that it can be applied with confidence by practitioners seeking to enhance their spatial coverage of *K* values.

The large set of varied-quality, yet vetted, *K* values were then integrated with the geologic characterization of the carbonate bedrock to assess the relative influence of specific geologic features on hydraulic conductivity. Three geologic controls were investigated: i) proximity to bedrock valleys, ii) carbonate rock texture and iii) sequence stratigraphic breaks. Results demonstrate that high *K* values do not correlate with a single geological feature, but that they are associated with various features that have

been enhanced by carbonate dissolution. Predicting the spatial distribution of *K* in carbonate rocks requires a regional understanding of the geological history with a conceptualization of where and when waters have interacted with the bedrock to dissolve and enhance porosity through geological time. This investigation concludes with a map identifying the area with the greatest probability of encountering high *K* in the main hydrostratigraphic unit, the Gasport Formation. The map supports the selection of groundwater resource exploration targets for a local municipality. Beyond the local benefits of this work, this investigation offers an approach that can be adopted by practitioners exploring for bedrock groundwater resources or characterizing contaminant transport pathways in complex, karstic carbonate bedrock groundwater systems.

The second research theme of this thesis represents a shift towards exploring the use of geochemical tracers and modeling tools for mapping regional groundwater flow systems in the same karstic carbonate bedrock setting investigated in the first research theme. Recharge timing and controls were investigated using several isotopic and geochemical indicators of recent recharge to groundwater. Spatial trends of higher tritium are consistent with aerobic redox chemistry in the carbonate groundwater systems underlying areas of thin or permeable sediment cover. Groundwater chemical evolution beyond recharge areas was assessed with general chemistry, redox characteristics and an investigation of water-rock interaction. A comparison of strontium isotope ratios ($^{87}Sr/^{86}Sr$) in bedrock and groundwater shows that long residence times can sometimes result in the isotopic signature of the rock imprinting on the groundwater. Observed increasing Sr to Ca ratios along the groundwater flow path are likely resulting from incongruent dissolution of dolomite and the precipitation of calcite with evolution. Sulphur isotopic composition of sulphate ($\delta^{34}S_{SO4}$ and $\delta^{18}O_{SO4}$) in groundwater shows isotopic evidence of pyrite oxidation in recharge areas, and a Silurian sulphur isotopic signature where bedrock aquifers are covered by thick and low permeability sediments, downgradient of identified recharge areas. For this investigation, isotopic and hydrochemical tools provided essential lines of evidence towards the development of a conceptual model of recharge and groundwater evolution in this complex geologic setting.

The main geochemical, hydrochemical and isotopic processes that form the conceptual model were then simulated with reactive transport modeling. The reactive transport model simulates chemical changes along a hypothetical 50 km flowpath, from recharge to closed-system evolution in the carbonate bedrock aquifer system. Disagreement between simulated and observed values provided insight into possible flaws in the conceptual model. Model calibration was done manually, without the commonly applied statistical improvements of fit and sensitivity analyses. This approach provided an appropriate level of scrutiny, given that the model objective was to quantify and assess the major processes rather than perfectly simulate the field dataset. Magnesium was the only parameter for which the model results gave

a very poor approximation of the field data in both concentration levels and general trend direction. Further investigation into the controls on dissolved magnesium is required. Despite this, the poor approximation of one component is considered a positive outcome, given that model contains 16 components that are involved in many coupled hydrochemical, geochemical and isotopic processes. The simulation results indicate that the geochemical, hydrochemical and isotopic processes that form the conceptual model are reasonably well understood throughout the flow system.

Acknowledgements

First of all, I would like to thank my supervisors Dr. Dave Rudolph and Dr. Dick Jackson for agreeing to take me on as a student. As a part-time, off-campus student, the odds were stacked against me from the start. I attribute my success in large part to the guidance and support that they both provided. Many thanks to Dave for always squeezing in time for a phone call, for helping me to see the big picture and for the many pep talks along the way. My deepest gratitude extends towards Dick for sharing his breadth of knowledge, as well as for being a quick, constructive and tireless reviewer throughout. In addition, many thanks to Dick for ensuring that I was supported by the best possible team of experts. To my unofficial supervisor, Dr. Shaun Frape, I extend my gratitude for his time as we shared many conversations about geochemistry, isotopes and life. In addition, I must also thank Shaun for his irreverence, which kept me laughing, and for his kindness. To my committee members, I also extend my thanks for their input along the way. Most noteworthy is the assistance and encouragement I received from Dr. Rich Amos at all stages of my min3p work. Early in the modeling adventures, Rich joked that "if you can't model it, it's not real". The old adage that "humour is truth" was confirmed as I discovered the insight that modeling can bring to a conceptual model built on empirical observations.

I was privileged to have support from external experts during my studies, most notably from Chris Neville and Frank Brunton. I would like to thank Chris Neville for his mentorship throughout this research journey. Conversations and a special study with Chris were paramount as I investigated the topics of well hydraulics, hydraulic test analysis and the link between geology and hydraulic conductivity in the Guelph area. I continue to admire, and aspire to, his ability to communicate complex information in simple and accessible ways. Many thanks also to my colleague Frank Brunton from the Ontario Geological Survey. Way back in 2009, standing at the bottom of a quarry, Frank demonstrated how essential understanding the geology is to solving groundwater problems in carbonate bedrock. His regional sequence stratigraphic model of the study area provided the foundation for my studies, and without it, my research would not have been possible. I am grateful for the many conversations and detailed explanations of life in the Silurian seas of the study area.

Without a doubt, my research could not have been accomplished without the help of friends and family. I would like to thank my colleague and mentor Stew Hamilton for always sharing his geochemistry expertise and field skills along the way. Many thanks are also extended to my support network: Katie, Bronwyn, Sara, Kayla and Trina. Instead of delivering heavy sighs in response to my requests to discuss the minutia of my thesis, you listened with kindness and offered much needed diversions. To my parents,

many thanks for helping out with the kids during field work and for the unwavering support throughout. You are the ones who set the stage for this act, and I'll be forever grateful.

Financial assistance for this research was provided by the Ontario Geological Survey. Many thanks to Jack Parker, the (now retired) Director of the survey, for believing in me and in the importance of this work. The opportunity to pursue this degree while working at the survey has been a career changing adventure for which I am extraordinarily grateful.

Last, but not least, I would like to acknowledge the incredible amount of support that I received from my husband Aaron over the course of my studies. Thank you for your consistent patience as I navigated the long and tortuous path to completing this degree.

Dedication

I dedicate this thesis to my daughters, Laura and Claire.

Table of Contents

List of Figures

List of Tables

Chapter 1 Introduction

1.1 BACKGROUND AND MOTIVATION

Fractured and karstic carbonate bedrock aquifers around the world are described as difficult to exploit for groundwater supply because of their heterogeneity and the challenges associated with predicting the locations of the most productive geologic features (Chen et al. 2017). This heterogeneity also presents challenges for mapping regional-scale groundwater flow systems because of the discontinuous nature of the geological features that form the main regional groundwater flowpaths and the logistical and financial difficulty associated with confirming flowpath continuity (Muldoon et al. 2001). Despite these challenges, approximately 20-25% of the world's water supplies come from karstic carbonate aquifers (Ford and Williams 2007). Falling within the category of karstic aquifers are the Early Silurian carbonate groundwater systems of Ontario's Niagara Escarpment cuesta region, which form the present study area. These carbonates have been described as containing groundwater resources of significant water quantity (Funk 1979; Sibul et al. 1980; Sharp et al. 2013; Brunton et al. 2007 and Brunton 2009) and excellent water quality (MacRitchie et al. 1994; Singer et al. 2003). Despite the significance of the groundwater resources, siting new wells in these carbonate bedrock aquifers remains a challenge because of heterogeneity (David Belanger, Water Supply Program Manager, City of Guelph, personal communication 2017).

The primary motivation of this thesis is the desire to improve our understanding of complex karstic carbonate settings so that we can more successfully identify groundwater resources exploration targets and map regional-scale groundwater flow systems. With this motivation in mind, the present study is organized into two research themes. The first research theme explores the relationship between geology and hydraulic conductivity (Chapters 2 and 3). The second research theme focuses on investigating methods suitable for delineating regional-scale groundwater flow systems in karstic carbonate bedrock systems (Chapters 4 and 5).

1.2 RESEARCH THEMES AND OBJECTIVES

The first research theme focuses on understanding spatial relationships between geology and hydraulic conductivity. Hydraulic conductivity values are typically sparse relative to geological heterogeneity in the areas that comprise most municipal well-fields and even larger municipal groundwater management areas in Ontario. The objective of the research presented in Chapter 1 is to develop a solution for improving the spatial coverage of hydraulic conductivity values. In this chapter, domestic water-well

specific capacity tests are used to make hydraulic conductivity estimates and these are carefully evaluated with respect to a high-quality hydraulic conductivity dataset by conducting several comparisons. Although previous studies have presented methods for making hydraulic conductivity estimates from specific capacity tests (e.g. Theis 1963; Brown 1963; Eagon and Johe 1972; Bradbury and Rothschild 1985; Mace 1997), this is the first investigation to test the suitability of combining these with high-quality hydraulic conductivity analyses.

The improved spatial coverage of hydraulic conductivity (*K*) values from Chapter 2 supports the Chapter 3 research objective of investigating the influence of geological controls on K. In Chapter 3, a large set of *K* values, comprising high-quality *K* values and those from specific capacity tests, is integrated with a recently developed geological model (Brunton 2009). The integration of this large set of *K* values with geology enables a semi-quantitative assessment of geological features on *K*. Previous workers have identified many different geological features as correlating with high *K* zones in karst-influenced carbonate aquifers. These geological features include coarse-textured bedrock (e.g. Rovey and Cherkauer 1994a), bedding plane fractures (e.g. Muldoon et al. 2001), areas of enhanced fracturing in stress-relief zones at bedrock valley edges (e.g. Cole et al. 2009) and sequence stratigraphic breaks (e.g. Meyer et al. 2016). These are considered within the geomorphological context of the study area, with a conceptualization of where waters have interacted with rock to dissolve and enhance porosity through geologic time.

The second research theme focuses on investigating approaches for delineating regional-scale groundwater flow systems in karstic carbonate bedrock. The first objective of this research theme is to assess the utility of various hydrochemical and isotopic tracers for identifying recharge areas and mapping hydrochemical evolution (Chapter 4). Although many analogs of chemical and isotopic evolution exist for carbonate groundwater systems, the majority of these are for non-glaciated regions (e.g. Plummer 1977; Banner et al. 1989; Katz et al. 1995 a,b; Uliana et al. 2007; Seibert et al. 2017). Grasby et al. (2008) have shown that where overlain by glacial sediments, recharge water can carry the geochemical signature of the overburden deep into the underlying carbonate bedrock aquifer. In Chapter 4, the utility of commonly applied tracer tools, such as redox parameters (e.g., Champ et al. 1979), strontium isotopes (e.g. Banner et al. 1998) and sulphur isotopes (e.g. Krothe and Libra 1983), is investigated for identifying and fingerprinting recharge and evolved hydrochemical end members in glaciated, carbonate groundwater systems. The most useful tracer tools are then explored as lines of evidence for a conceptual model of the hydrochemistry and isotopic composition associated with recharge and groundwater evolution in the study area.

Following on the conceptual model of recharge and hydrochemical evolution for the study area (Chapter 4), a reactive transport model is developed to simulate the main chemical and isotopic processes occurring along one regional-scale flowpath. The objective of this modeling exercise is to assess the geochemical system as a whole, which should highlight where geochemical processes might have been misrepresentated or misunderstood in the conceptual model. Because the conceptual model was developed by isolating and investigating individual hydrochemical or isotopic processes, the reactive transport model provides a means for assessing interactions among these processes. Although reactive transport modeling has not traditionally been used to simulate chemical processes at regional-scales, the dominant chemical processes occurring in carbonate groundwater systems have recently been simulated successfully at the well-field scale (Descouvrieres et al. 2010; Seibert et al. 2017). The suitability of reactive transport modeling to regional-scale investigations is a secondary objective of the research presented in Chapter 5.

1.3 ONTARIO GEOLOGICAL SURVEY GROUNDWATER MAPPING PROGRAM DEVELOPMENT

Following the Walkerton, ON, tragedy of the year 2000, where seven people died from bacterial contamination in a municipal carbonate bedrock groundwater supply system, the Ontario government began emphasizing the importance of groundwater resources characterization and protection (O'Conner 2002). In response, the mandate and funding of the Ontario Geological Survey was enhanced to include geoscience mapping that supports groundwater resources characterization. Because karstic carbonate bedrock systems are inherently challenging to map and characterize, Ontario Geological Survey funding was provided for this thesis with the aim of supporting the development of new groundwater mapping and characterization techniques that can be applied in similar geological settings across the province of Ontario.

1.4 THESIS ORGANIZATION

This thesis comprises six chapters, with Chapters 2 through 5 addressing the specific objectives described for each research theme. Chapters 2 through 4 were written in manuscript format, prepared as stand-alone manuscripts for submission to scientific journals. Chapter 5 is presented in a traditional thesis chapter format, meaning that reference has been made to figures and ideas presented in previous chapters. Chapters 2 and 3 are published in scientific journals, with references as follows:

Priebe EH, Neville CJ, Rudolph DL (2017) Enhancing the spatial coverage of a regional high-quality hydraulic conductivity dataset with estimates made from domestic water-well specific-capacity tests. Hydrogeology Journal, 26:395-406

Priebe EH, Brunton FR, Rudolph DL, Neville CJ (2018) Geological controls on hydraulic conductivity distribution in a karst-influenced carbonate bedrock groundwater system, southern Ontario, Canada. *in press* at Hydrogeology Journal.

For the first published manuscript, EH Priebe developed the idea for the paper, conducted the data gathering and analyses and wrote and edited the manuscript. Contributions by co-authors CJ Neville and DL Rudolph consisted of participation in early discussions about the subject matter and 2-3 rounds of manuscript review, where co-authors provided technical and editorial suggestions. These suggestions were considered and incorporated where deemed appropriate by EH Priebe. Responses to the peer reviews received from Hydrogeology Journal were written by EH Priebe. Peer review comments were minor, comprising primarily of the suggestion that further information would be useful, specifically further explanation of the methods to help users of the approach and information about where similar well datasets might be available outside of Ontario.

For the second published article, EH Priebe developed the idea for the paper, conducted the data gathering and analyses and wrote and edited the manuscript. Contributions by co-authors consisted primarily of early discussions and debate about geological terminology and 2-3 rounds of manuscript review in which co-authors provided technical and editorial suggestions. These suggestions were carefully considered and incorporated where deemed appropriate by EH Priebe. Responses to the peer reviews received from Hydrogeology Journal were written by EH Priebe. The input from peer reviewers identified the need for additional discussion about the significance of the fracture network relative to the geological controls that were the focus of the investigation. In addition, peer reviewers suggested that examples of similar settings elsewhere be provided to improve the global context, or appeal, of the work.

Chapter 2
Enhancing the Spatial Coverage of a Regional High-Quality Hydraulic Conductivity Dataset with Estimates Made from Domestic Water-Well Specific-Capacity Tests

2.1 INTRODUCTION

High-quality estimates of hydraulic conductivity (*K*) values tend to be sparse relative to the large areas under investigation in regional-scale groundwater studies. Domestic well specific capacity tests, which are frequently abundant, can be used to estimate *K* (e.g., Theis 1963), and as such could potentially provide a reconnaissance-level set of supplementary *K* estimates. Domestic water wells are ubiquitous across North America, and although their associated well records commonly do not contain the information required to support rigorous hydraulic test analyses, they often contain the information required to calculate specific capacity and a related *K* value (e.g., Ontario 2003; State of California 2007). In this study, the integration of *K* values derived from specific capacity tests on domestic wells with a high-quality *K* data, determined though conventional hydraulic testing methods, is assessed through comparisons at two different scales: study area-wide (600 km^2) and in a single geological formation within a portion of the broader study area (200 km^2).

From the 1960s through the 1990s, the literature is replete with articles discussing the details of estimating *K* from specific capacity test data. Early publications focused on the development of the fundamental mathematical relation between specific capacity and *K* (e.g., Theis 1963; Brown 1963). Later articles presented approaches for improving the accuracy of *K* estimates from specific capacity by correcting for well losses, which are the drawdowns caused by factors other than frictional head loss in the formation (e.g., Eagon and Johe 1972; Bradbury and Rothschild 1985). Ignoring the influence of well losses can result in unreliable *K* values for single-well hydraulic tests that rely on the drawdown in the pumping well for their estimation. Despite this, correcting for well losses requires knowledge of parameters that are not often known and making corrections using assumed parameter values has been shown to introduce significant error (Mace 1997).

Through the 1990s, many researchers began to develop site-specific relations between *K* and specific capacity (e.g., Huntley et al. 1992; Razak and Huntley 1992; El-Naqa 1994; Mace 1997). Most of these site-specific relations were developed from hydraulic tests conducted in conventional, short-screened monitoring wells, limiting their application to other types of wells with differing geometries and pumping rates. Most *K* estimates made with these empirical relations have large degrees of uncertainty, with error margins of up to 1.4 orders of magnitude (e.g., Huntley et al. 1992; Mace 1997), calling into question the effort required to develop them.

Where previous studies focused on how to best make *K* estimates from specific capacity, what practitioners need now is a simple approach to integrate these more approximate *K* values from specific capacity tests into their high-quality *K* datasets. Such an approach is presented here. For this approach, the *K* estimates are made from specific capacity tests using the Cooper-Jacob (1946) modification of the Theis (1935) relation, following the general approach described by Theis (1963) and Driscoll (1986). Turbulent well losses are quantified using the Hantush-Bierschenk analysis (Hantush 1964; Bierschenk 1964) and determined to be insignificant, which is not surprising given the small pumping rates employed for the domestic well specific capacity tests. The suitability of integrating the high-quality *K* dataset with the *K* values from specific capacity is assessed through multiple comparisons.

2.2 METHODS

2.2.1 Study Area

The 600 km^2 study area is located in southern Ontario, Canada (Figure 2.1). The city of Guelph, a city of approximately 120,000 people, is located within the study area boundary. The primary drinking water source for the city of Guelph is groundwater, drawn from wells completed in the carbonate bedrock, specifically the Gasport Formation (Quackenbush and Gemin 2014). The carbonate bedrock is Early Silurian in age and consists of approximately 100 metres of stacked dolostones (Brunton 2009). The Gasport Formation ranges in thickness from 25 m to more than 70 m and is a confined aquifer in most areas, with flow zones overlain by lower permeability portions of the Gasport Formation itself, or by overlying carbonate bedrock formations (Brunton 2009). The findings of Priebe et al. (2017) have shown that there is great spatial variability of hydraulic conductivity in the carbonate bedrock, hence the need for additional hydraulic conductivity values in the study area.

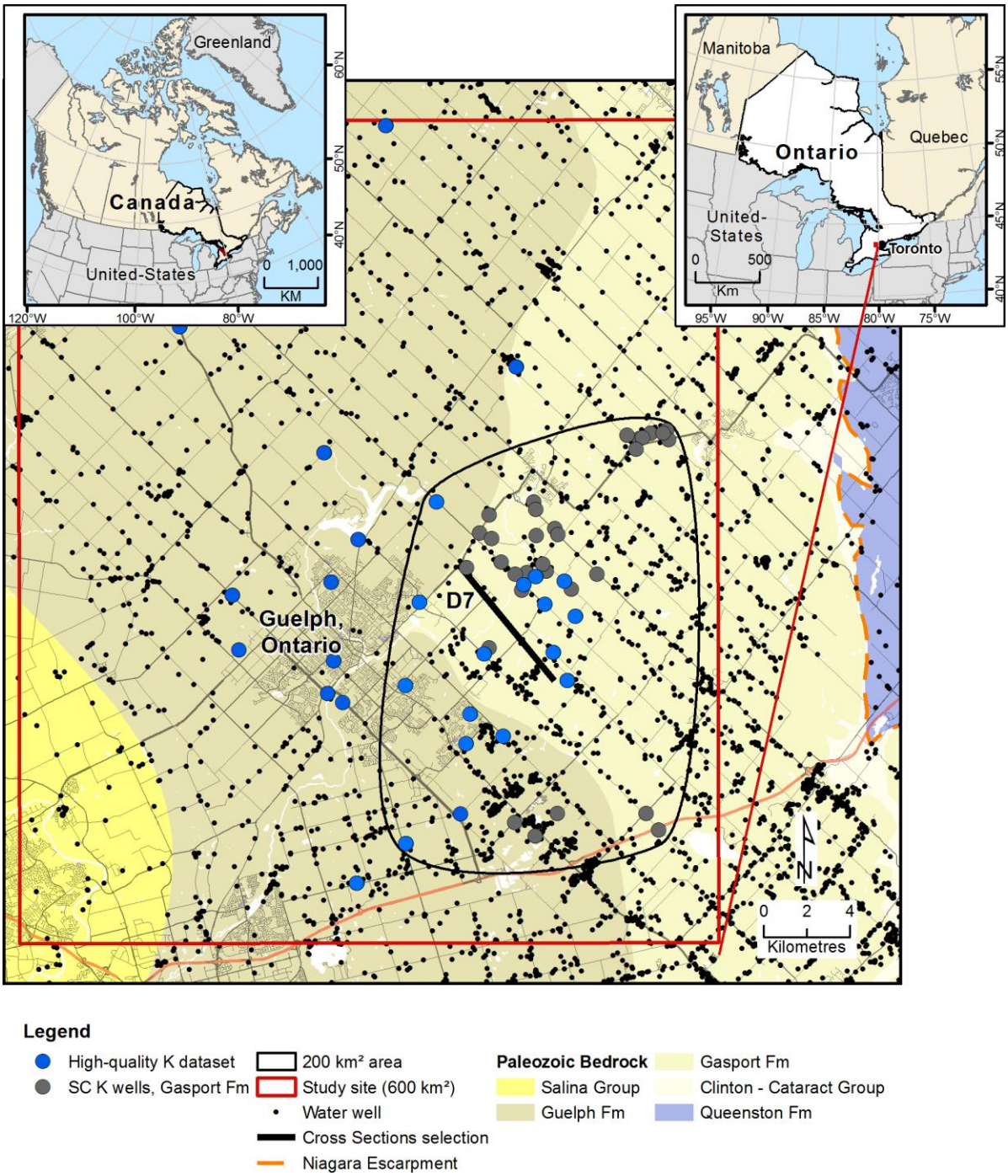

Figure 2.1. The study area is shown with the distribution of 32 monitoring wells that were used to develop the high-quality hydraulic *K* dataset (blue symbols). The distribution of 7,529 water wells that were used to develop the set of *K* estimates from domestic well specific capacity tests (the SC *K* estimates) are represented with *small black symbols*. The two sets of *K* values are compared at the study area scale (600 km^2), shown with the *red boundary*. A comparison is also conducted within a single stratigraphic formation (the Gasport Fm) at a smaller scale (200 km^2) shown with a *black boundary*. The domestic water wells used for the smaller scale comparison are represented with *grey symbols.*

2.2.2 Developing the High-Quality *K* Dataset

The high-quality *K* dataset employed in this study was created by analyzing the raw displacement data for 71 single-hole pumping and slug tests (Di Biase et al. 2006, Piersol and Petrie 2011, Di Biase and Petrie 2009 and Funk 2009) derived from a network of wells completed in carbonate bedrock within the study area. These hydraulic tests were conducted in discrete portions of wells that were isolated by packers or in monitoring wells with short well screens. The stratigraphy at each of these wells was characterized in detail by core logging and the interpretation of down-hole geophysical logs.

The data from constant-rate pumping tests were analyzed using the Cooper-Jacob method (1946). Each analysis was conducted with diagnostic insight provided by the derivative curve with the approach of Bourdet (2002). The derivative curve assists with fitting the solution to the portion of data that reflects a radial flow regime in an areally extensive aquifer (i.e., infinite-acting) and avoids the portions of the data affected by wellbore storage or boundaries. The Cooper-Jacob method (1946) has the advantage of providing a reliable transmissivity estimate despite the influence of well losses because the calculation is made with the rate of change of drawdown, which is unaffected by well losses, rather than the absolute magnitude of the drawdowns, as when matching the data with the Theis (1935) solution, for example (Meier et al. 1998; Halford et al. 2006).

The data from slug tests were analyzed with the Cooper, Bredehoeft and Papadopulos (1967) (CBP) method. The CBP method was selected because it considers compressibility in the system, adding some rigor to the analysis, and because it allows for a larger portion of the displacement data to be matched to the solution than the more commonly used zero-storage models. The prediction of storativity values that fall within a range of physically realistic values was interpreted as an indication that the analytical model used to conduct the analyses captures the major processes causing drawdown in the pumping well. A physically-realistic storativity range for the study area geology, which consists of carbonate rock formations that range from reefal to intact (Brunton 2009), was estimated from test interval information and literature values of compressibility. Typical compressibility values for the range of media encountered are reported by Younger (1993) as 10^{-9} to 10^{-11} (m-s^2/kg). The porosity range for karst-influenced carbonates is 0.05 to 0.5 (Freeze and Cherry 1979). From these values, the broad range of physically realistic specific storage values was estimated to be 10^{-5} m^{-1} to 10^{-7} m^{-1}. The storativity range was then calculated by multiplying these specific storage values with the assumed effective aquifer thickness for the site, which is 3 m.

Where a CBP analysis did not yield a physically realistic storativity estimate, a second analysis was conducted with a fixed realistic storativity value (~$3x10^{-6}$). If the second analysis did not yield an acceptable match of the CBP solution to the data, the data were analyzed with the zero-storage Bouwer

and Rice (1976) solution for a fully penetrating well in a confined aquifer. The Bouwer and Rice (1976) solution was applied to the 0.2 to 0.3 portion of the normalized drawdown, as recommended by Butler (1998).

2.2.3 Developing the Set of *K* Estimates from Specific Capacity Tests (SC *K* Estimates)

Specific capacity tests are conducted by pumping a single well at a constant rate for a known duration. The pumping rate, static water level and drawdown at test termination are documented for each specific capacity test for all water well records in Ontario, Canada (Ontario 2015), as well as for many other jurisdictions (e.g., State of California 2001). Specific capacity is the ratio of the pumping rate (Q) and the drawdown in the pumping well (s_w). To estimate K from specific capacity, the transmissivity (T) is first calculated and then converted to K.

To estimate T from specific capacity, the Cooper-Jacob (1946) modification of the Theis (1935) equation was used, with some assumptions applied. This modified equation (Cooper-Jacob 1946), which is appropriate for all but the very briefest durations of pumping, can be arranged to solve for specific capacity.

$$SC = \frac{Q}{s_w} = \frac{4\pi T}{2.303\, log_{10}\left(0.5615\frac{4Tt}{r_w^2 S}\right)} \qquad (1)$$

Equation 1 can be rearranged to solve for the transmissivity:

$$T = SC \times \frac{2.303\, log_{10}\left(0.5615\, \frac{4Tt}{r_w^2 S}\right)}{4\pi} \qquad (2)$$

All of the specific capacity tests considered in this study involved pumping from wells with 6-inch diameter screens (r_w = 0.076 m) for a 1 hour duration of pumping (t = 0.0417 d). The storativity (S) value was assumed to be 10^{-6}, midway along the range described above. Transmissivity appears twice in equations 1 and 2. To address this, Theis (1963) and Driscoll (1986) recommended specifying an assumed average T value in the right-hand side of equation 2 to enable a T estimate. They justify this step by demonstrating that the calculated T is insensitive to the assumed average T because of its place in the log-term on the right side of equation 2. An alternative approach to that of Theis (1963) and Driscoll (1986) is adopted here. Rather than specifying an assumed average T value into equation 2 to calculate T, specific capacities were plotted for the range of T values obtained from the 71 high-quality hydraulic test

analyses (Figure 2.2), which spans from 0.1 m^2/day to 1000 m^2/day with a median value of 10 m^2/day. The advantage of this approach over that of Theis (1963) and Driscoll (1986), is that the suitability of specifying an assumed average *T* into equation 2 is assessed, rather than assumed. The calculated *T* values are indicated by the *open circles* on Figure 2.2. As shown in Figure 2.2, the calculated values are approximated closely by the following simple relation between *T* and specific capacity.

$$T = 1.5 \times SC \qquad (3)$$

At the median *T* value from the high-quality tests (10 m^2/d), the simple relation of equation 3 provides a near perfect match to the calculated values (Figure 2.2). At the lower end of the known *T* range (0.1 m^2/day), the simple relation of equation 3, yields a slightly larger value of the *T*. At the upper end of the known *T* range (1000 m^2/day) the simple relation of equation 3 yields a slightly smaller value of the transmissivity. At the ends of the range, the calculated values and those estimated with equation 3 differ by a factor of about 1.2, which is considered negligible given that the known *T* range spans four orders of magnitude. The approach used here makes it possible to roughly quantify the error that can be incurred from using equation 3, whereas the approach of Theis (1963) and Driscoll (1986) requires the assumption that the error incurred from the method itself is insignificant. The assessment presented in Figure 2.2 demonstrates that estimating *T* with equation 3 is appropriate for the range of values that is likely to be encountered within the study area.

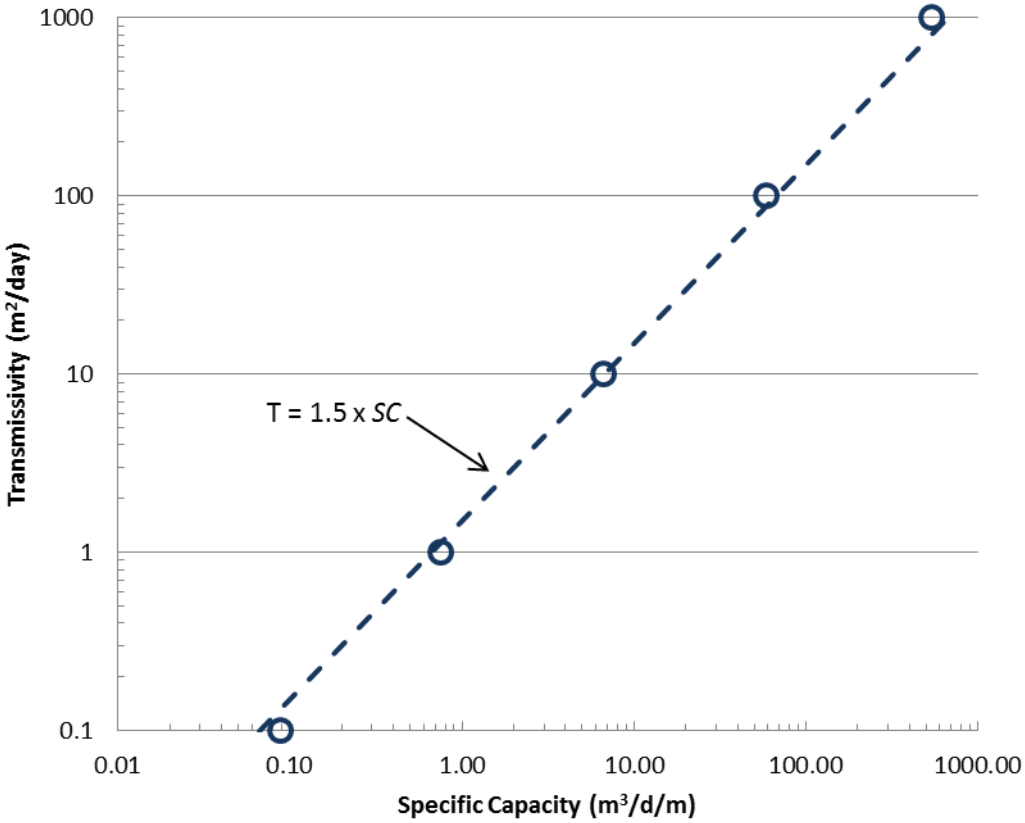

Figure 2.2. The relationship between specific capacity and transmissivity is shown. The *open circles* are the specific capacity values calculated over the transmissivity range of the high-quality tests. The *dashed line* is the simple linear relation of equation 3 (T = 1.5×SC).

In developing the simple estimator of equation 3, a storativity value was estimated from literature values, the properties of the study area geology, and from the transient calibration of a local groundwater flow model (Matrix 2014). Because of remaining uncertainty in the assumed storativity value, the sensitivity of T to the assumed storativity value was evaluated (Figure 2.3). The relationship between T and specific capacity for a range of storativity values spanning two orders of magnitude (10^{-6} to 10^{-4}) is marginal (Figure 2.3), demonstrating relative insensitivity of the relationship between T and specific capacity to the storativity value.

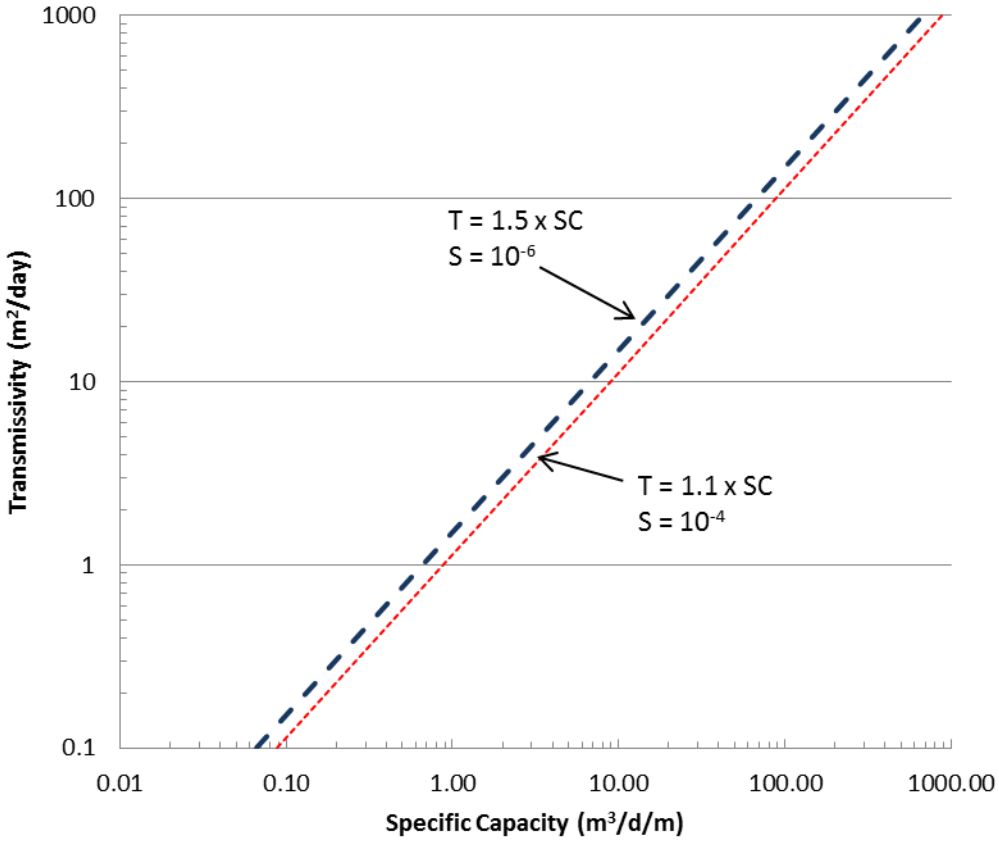

Figure 2.3. An evaluation of the sensitivity of the relationship between specific capacity and transmissivity to the storativity value. The blue dashed line represents the transmissivity estimator presented in equation 2. The red dashed line represents an estimator developed with a two-order of magnitude larger storativity value than what is considered physically reasonable for the study area geology.

With the positive results of the assessments and sensitivity analysis just presented, the *T* estimator (equation 3) was applied to estimate *T* from specific capacity values for 7,529 domestic water wells within the 600 km^2 study area (Figure 2.1). Values of horizontal hydraulic conductivity (*K*) were then calculated from the *T* values by dividing *T* with an "effective" aquifer thickness. The National Research Council (1996) noted that there is a fundamental problem in estimating *K* from *T* in fractured rock settings, as the groundwater flow occurs in narrow fracture sets rather than being distributed uniformly over the length of the open interval of a well. It is more appropriate to report *T* values rather than K values because *T* is the parameter that is estimated from most hydraulic test analyses and can be estimated without assuming an effective aquifer thickness. However, the motivation for reporting *K* values instead of *T*, is that *K* is the more fundamental quantity against which practitioners compare their own values as a frame of reference. For the present study, a uniform effective aquifer thickness of 3 m was assumed for each domestic well. The effective aquifer thickness of 3 m was selected to reflect the average length of conductive zones in the study area bedrock, with the value assumed based on empirical evidence gathered

from borehole core logging, borehole flow profiling and FLUTe™ K-profiling (Keller et al. 2014). This empirical evidence demonstrates that the major groundwater flow zones for the study area are an average of 3 m in length, with examples presented in Lee et al. (2011). The selected effective aquifer thickness is intended to reflect the conductive portions of the bedrock, to prevent *K* from being under-estimated by including additional open-borehole lengths associated with the low-permeability massive rock sections that do not contribute to groundwater flow. The assumed 3 m effective aquifer thickness also reflects the average aquifer thicknesses used to convert transmissivity to *K* for the high-quality *K* dataset.

2.2.3.1 Quantifying Turbulent Well Losses for Specific Capacity Tests

Previous workers have attempted to account for well losses in the estimation of *K* from specific capacity tests (e.g., Eagon and Johe 1972; Bradbury and Rothschild 1985). For turbulent well losses, which are proportional to the square of the pumping rate, the relatively low pumping rates of the domestic well specific capacity tests used in this study are not expected to result in significant turbulent losses. However, to be cautious, the influence of turbulent well losses on *K* estimates made from specific capacity values was assessed with a Hantush-Bierschenk analysis (Hantush 1964; Bierschenk 1964) using the results of a three-stepped pumping test. The three-stepped pumping test was conducted at a study area monitoring well that serves as a domestic well analog, with the same diameter, open-borehole construction and pumping rates as those reported for the domestic well specific capacity tests.

2.2.3.2 Placing the K Estimates from Domestic Water Well Specific Capacity Tests into the Regional Stratigraphic Framework

One of the strengths of the high-quality *K* dataset is that the stratigraphic formation/s in which the hydraulic test was conducted is known. For the SC *K* estimates to be compared with and integrated into the high-quality *K* data set, the SC *K* estimates must be also be correlated with stratigraphic formations. This has been accomplished by linking the "water found" information in the associated domestic water well record to a geologic formation. It is assumed that the most significant water producing zone in each open-hole domestic water well, and the one represented by the specific capacity test, coincides with the position in the borehole where the well driller encountered a surge of water or lost circulation of drilling muds, described on the well record as "water found" (Ontario 2015). This "water found" position marks the point in the hole where an adequate domestic water supply was intercepted, usually prompting the termination of drilling. The stratigraphic position of each SC *K* value was inferred by placing the "water found" position for each well on a geologic cross-section for the study area. This was conducted to

enable a comparison of the two sets of *K* values at the geological formation scale. An example cross section is presented in Figure 2.4.

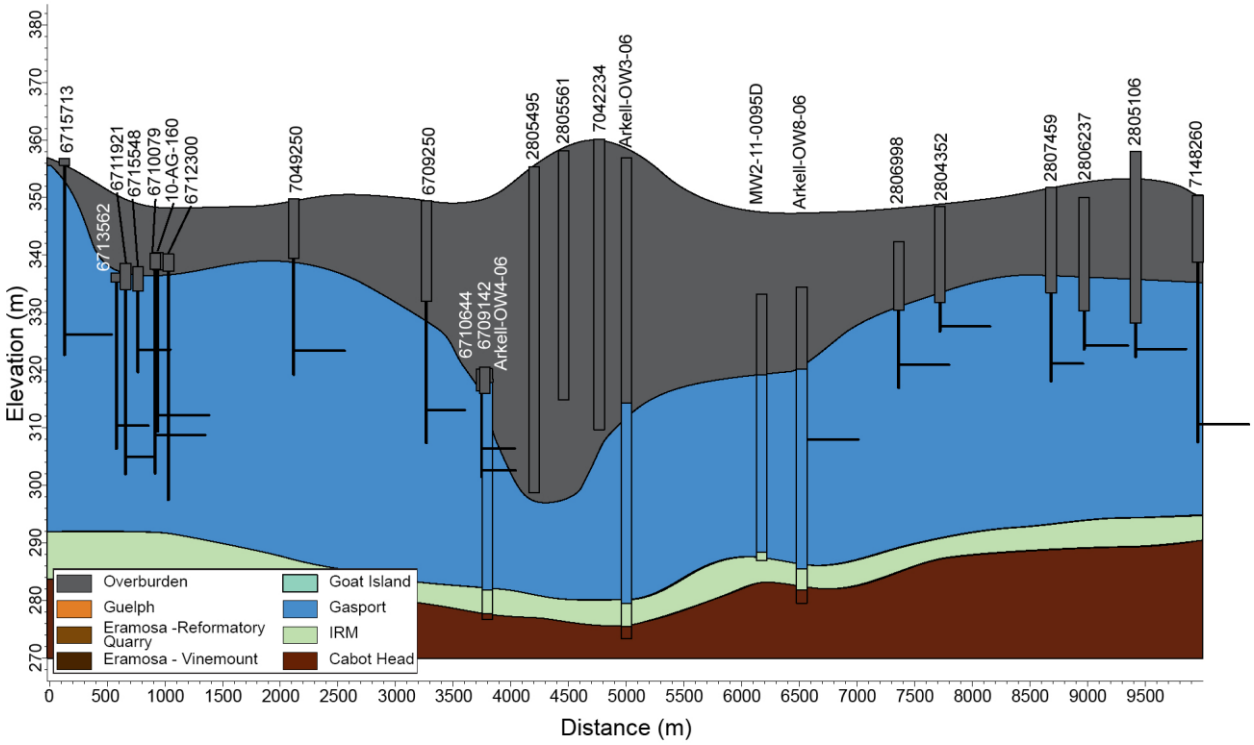

Figure 2.4. An example of one of the cross-sections (D7) used to assign stratigraphic formations to the domestic wells, and thus the SC *K* values. The "water found" positions are identified for each domestic well with a *horizontal black bar*. The stratigraphy for the high-quality wells and boreholes used to develop the stratigraphic characterization is shown with a rectangle, infilled with the formation colours in the legend. The location of cross-section D7 in the study area is shown on Figure 2.1.

2.2.4 Comparing the K Estimates from Specific Capacity Tests (SC K) with the High-Quality K Dataset

The well locations associated with the two sets of *K* values are shown in Figure 2.1, with the domestic water wells associated with the set of SC *K* estimates represented by *small black symbols* and the high-quality *K* dataset wells represented by larger *blue symbols*. The two sets of *K* values are compared at two different scales; for the entire 600 km^2 study area and in a single stratigraphic formation over a 200 km^2 portion of the study area. The study-area wide comparison was conducted as a proof-of-concept, to broadly evaluate trends in ranges and distributions for the two sets of *K* values. The second comparison was conducted in a smaller portion of the study area, within a single stratigraphic formation (the Gasport Formation), where the geology is well-characterized and consistent (Funk 2009; Brunton 2009), to assess whether the SC *K* estimates represent the formation-scale trends in *K* distribution that are observed in the high-quality *K* dataset. The method of comparison consisted of plotting the cumulative probability

distributions of log-K values for both sets of values using the Cunnane plotting position method (1978), as modified by Helsel and Hirsch (1992). The advantage of this plotting position is that normally distributed datasets plot as straight lines, which makes it easy to compare them against each other by eye rather quickly, without the need for statistical methods of comparison. Given the uncertainty inherent in the SC K estimates, the desire for simplicity in approach and the broad range of K values encountered in the study area (4 orders of magnitude), such a quick and easy comparison offered by the cumulative probability plot provides an acceptable level of rigour.

2.3 RESULTS

2.3.1 Quantifying Turbulent Well Losses for a Typical Water Well Specific Capacity Test

A three-stepped pumping test was used to quantify the turbulent well losses associated with a typical specific capacity test conducted in the study area domestic wells. Monitoring well MW06-09, in which the stepped pumping test was conducted, was used as an analog because it has the same diameter as the domestic wells and because the stepped pumping rates (39 m^3/day, 79 m^3/day, 138 m^3/day) capture the median specific capacity test pumping rate of 79 m^3/day from the 7,529 water well records. The three pumping steps are presented in a Hantush-Bierschenk plot (Figure 2.5) with pumping rate plotted against the specific drawdown (Hantush, 1964; Bierschenk 1964). Because the relationship between specific drawdown and pumping rate is linear, the Jacob (1946) model for quantifying pumping well drawdowns, and identifying the magnitude of turbulent well losses, is deemed appropriate.

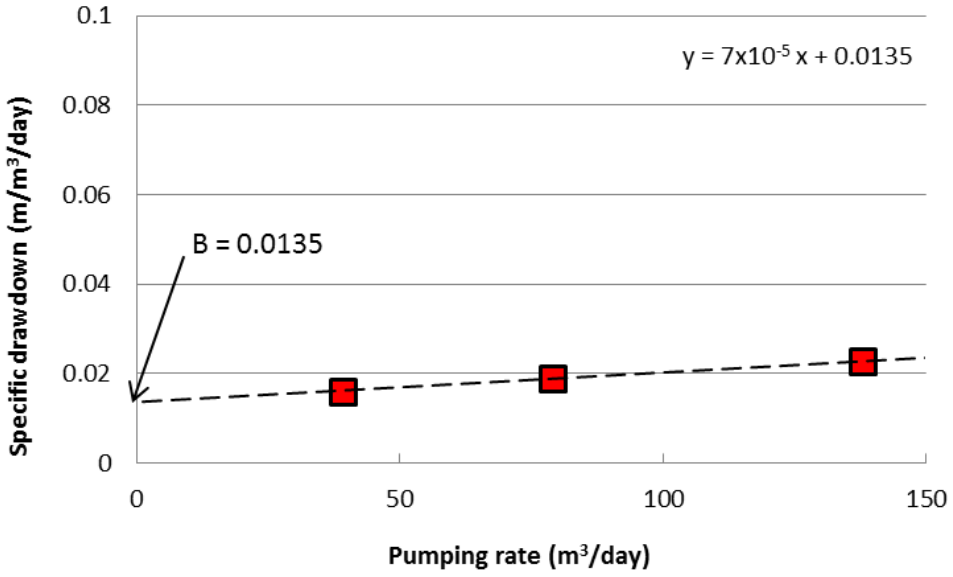

Figure 2.5. A Hantush-Bierschenk plot for a three-stepped pumping test conducted in MW06-09.

The relationship between specific drawdown and well losses is described by Jacob (1946) as:

$$\frac{s_w}{Q} = B + CQ \qquad (4)$$

Where,

s_w is the drawdown in the well (m)

Q is the pumping rate (m^3/day)

B is the formation constant (m/m^3/day)

C is the well loss coefficient (day^2/m^5).

The formation constant (B) and the well loss coefficient (C) are represented in Figure 2.5 as the y-intercept and the slope of the line, respectively. The formation constant (B) represents the inverse of the specific capacity with turbulent well losses removed. To make a K estimate that is corrected for turbulent well losses, the inverse of the B is multiplied by the transmissivity estimator of equation 3, and the transmissivity then divided by the effective aquifer thickness of 3 m.

The corrected K estimate is presented in Table 2.1 alongside the uncorrected values calculated from the specific capacity value for each pumping step, using the transmissivity estimator of equation 3. The corrected and uncorrected K estimates are essentially identical, indicating that turbulent well losses are insignificant for the study area domestic wells at the pumping rates employed.

Table 2.1. A comparison of K estimates that are corrected for turbulent well losses with uncorrected K estimates.

Pumping rate (m^3/day)	Uncorrected SC value for each pumping step (m^3/day)	Uncorrected *K* estimate for each pumping step (m/s)	Corrected *K* estimate (m/s)
39	62	$4x10^{-4}$	$4x10^{-4}$
79	53	$3x10^{-4}$	
138	44	$3x10^{-4}$	

The previous example provides empirical evidence that turbulent well losses are not an issue for this well, and likely not for typical domestic wells. Further support for this claim is presented in the following theoretical example, using the approach of Walton (1962):

$$s_w = CQ^2 \qquad (5)$$

$$s_w = 0.00012 \text{ m}$$

Where:

s_w = turbulent well loss (m)

C = well loss constant (1900 s^2/m^5)

Q = Typical pumping rate for a domestic well ($2.5x10^{-4}$ m^3/s)

The typical pumping rate for a domestic well in Ontario is 4 US gallons per minute, or $2.5x10^{-4}$ m^3/s (Ontario 1996). The well loss constant provided is the suggested typical value for a properly constructed and developed well (Walton 1962). The drawdown in the well that can be attributed to turbulent well losses is 0.00012 m, which is only a small portion of the total drawdown and would thus have no effect on the hydraulic parameter estimate. This theoretical example and the empirical one presented above demonstrate the insignificance of turbulent well losses on typical domestic wells, confirming that they need not be accounted for in the development of the SC *K* estimates.

2.3.2 Study-Area Scale Comparison of *K* Estimates (600 km^2)

The study-area scale comparison was conducted as a first step, to assess the ranges and distributions of *K* for the two sets of values. To facilitate the comparison, the high-quality *K* dataset (n = 71) and the set of SC *K* estimates (n = 7,529) are presented on cumulative probability plots (Figure 2.6). Both sets of *K* values approximate straight lines, indicating log-normal distributions, which is the commonly observed trend for *K* datasets (Neuman 1982). The geometric means of the two sets of *K* estimates, which are identified at the 50% cumulative probability point, differ by a factor of about 2.5 and the SC *K* set of estimates has a smaller standard deviation than the high-quality *K* dataset (see Table 2.2). At the high end of the *K* range, above $1x10^{-4}$ m/s, the distributions for the two sets of *K* estimates are nearly

indistinguishable, but below this threshold, the two distributions appear to diverge. Because both sets of *K* values are log-normally distributed, and the geometric means vary within the same order of magnitude, this is considered a good correlation. Given the many assumptions that are incorporated into the *T* estimator presented in equation 3, this correlation of means and distributions is a promising outcome in the context of the study area *K* range, which spans over four orders of magnitude.

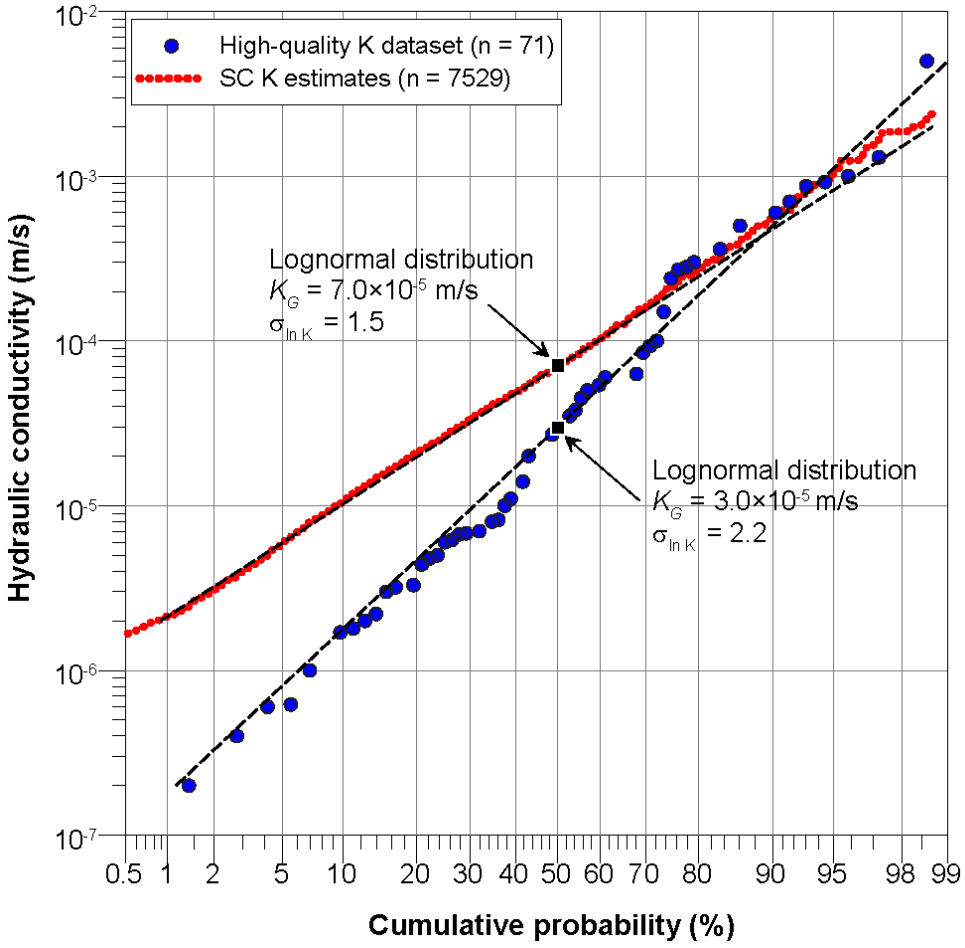

Figure 2.6. The cumulative probability distributions for the SC K estimates (*red symbols*) and the high-quality *K* dataset (*blue symbols*) are presented. The normal distribution lines for both sets of estimates are presented as *dashed black lines.* The geometric mean *K* values (K_G) are symbolized with black squares.

Table 2.2. A comparison of the two sets of *K* estimates for the 600 km^2 study area.

	Sample size	**Geometric Mean *K* (m/s)**	**Standard Deviation (ln *K*)**
High-quality *K* dataset	71	$3x10^{-5}$	2.2
SC *K* estimates	7,529	$7x10^{-5}$	1.5

While the two sets of *K* estimates match well at the high end of the *K* range, the comparatively smaller standard deviation observed for the set of SC *K* estimates can be attributed to an absence of *K* estimates at the lower end of the *K* range. This absence of low estimates for the SC *K* likely reflects the purpose of a domestic well. Domestic water wells must encounter sufficient yield to support the needs of the water user. Experienced well drillers know enough about the areas in which they drill to avoid locations where the formations are not sufficiently transmissive to support a domestic supply; therefore, the SC *K* estimates do not contain values at the low end of the *K* range. In contrast, the high-quality *K* dataset consists of the analyses of hydraulic tests conducted in monitoring wells installed within both aquitards and aquifers, resulting in the broader associated range of *K* values observed in this dataset. To account for the inherent differences in the two sets of *K* values, a second comparison has been conducted between the SC *K* estimates and a truncated version of the high-quality *K* dataset (Figure 2.7). In this comparison, the low *K* values of the high-quality *K* dataset, those less than 10^{-5} m/s, have been removed and a new cumulative probability plot generated. Because the high-quality K dataset has been truncated in Figure 2.7 for the purpose of presenting a hypothetical comparison, the plot should not be considered as a test of normality. With the low *K* values removed for the high-quality *K* dataset, the *K* distributions are essentially the same.

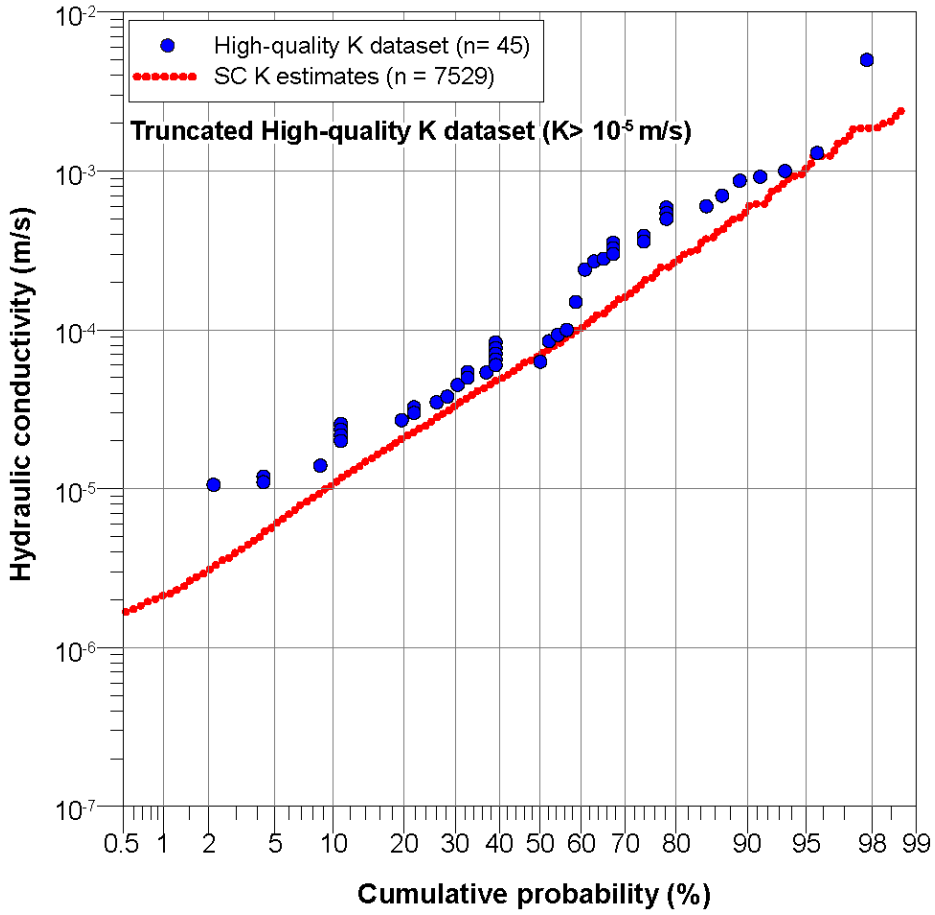

Figure 2.7. The cumulative probability distributions for the SC *K* estimates (*red symbols*) and a truncated version of the high-quality *K* dataset (*blue symbols, stacked to show duplicates*) are presented. The high-quality *K* dataset was truncated below 10^{-5} m/s.

The results of this study-area wide comparison are an effective proof-of-concept, suggesting that the SC *K* estimates might be used to improve data coverage for broad evaluations of spatial *K* trends. Consideration of the differences between the two sets of *K* estimates at the low end of the *K* range, such as the comparison presented in Figure 2.7, can be made to support the use of the SC *K* values to supplement a high-quality *K* dataset.

2.3.3 Comparison of *K* Values in a Single Geologic Formation in a 200 km^2 Portion of the Study Area

A comparison of the two sets of *K* values was also conducted in a single stratigraphic formation, the Gasport Formation, in a 200 km^2 portion of the study area (Figure 2.1). The lithology of the Gasport Formation is consistent within the limits of this 200 km^2 portion of the study area (Brunton 2009), which is the reason for the selection of this area for the comparison. The Gasport Formation is generally the sub-cropping or out-cropping geological formation in this area, limiting the likelihood of cross-

formational flow. The wells used for this comparison were selected by confirming that the stratigraphic position of the well screens for the high-quality wells and boreholes, as well as the "water found" positions of the domestic wells are in the Gasport Formation. Study-area wide, the Gasport Formation produces the majority of the local domestic and municipal water supplies (Quackenbush and Gemin 2014).

For this comparison, the *K* distributions for the two sets of estimates correlate very well, with the significant overlap in *K* distributions making it difficult to distinguish between them (Figure 2.8). Both sets of *K* values approximate log-normal distributions quite well despite the relatively small sample sizes. Like the study-area scale comparison presented above, the SC *K* estimates have a slightly smaller standard deviation than the high-quality *K* dataset, similarly owing to an absence of values reported for the very low end of the *K* range (Table 2.3, Figure 2.8). When compared with the *K* distributions for the entire study area (Figure 2.6), the *K* distributions for just the Gasport formation (Figure 2.8), for this 200 km^2 area, fall within a narrower range with smaller standard deviations and higher *K* trends. The excellent correlation between both *K* distributions presented in Figure 2.8, suggests that SC *K* estimates can be combined with the high-quality dataset to improve data coverage for groundwater investigations at the stratigraphic formation scale, which is relevant to municipal well-field scale investigations.

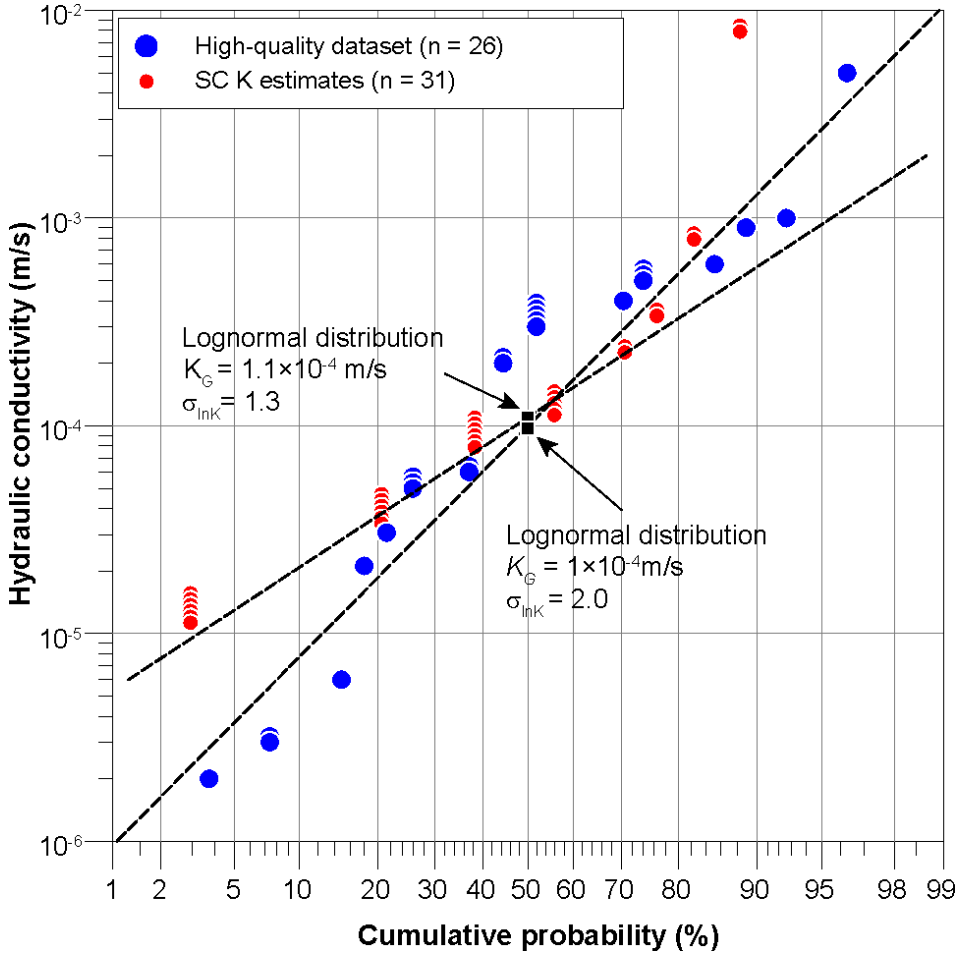

Figure 2.8. Cumulative probability distributions for the high-quality *K* dataset (*blue symbols*) and the set of SC *K* estimates (*red symbols*) are shown for wells drawing water from the Gasport formation in a 200 km^2 portion of the study area. Overlapping data points are shown with *stacked symbols*. The log-normal distributions for both sets of *K* values are shown as *black dashed lines*. The geometric mean *K* values (K_G) are symbolized with black squares.

Table 2.3. A comparison of the high-quality *K* values with the set of specific capacity estimates for a 200 km^2, portion of the study area with hydraulic tests and specific capacity tests conducted in one geologic formation.

	Sample size	**Geometric Mean *K* (m/s)**	**Standard Deviation (ln *K*)**
High-quality *K* dataset	26	1x10^{-4}	2.0
SC *K* estimates	34	1.1x10^{-4}	1.3

2.4 DISCUSSION AND CONCLUSIONS

This investigation was driven by a need for more *K* estimates in a regional-scale study area, which led to a search for additional sources of information. Domestic water wells are ubiquitous across much of North America, and they are often excluded from analyses because they do not directly contain the hydraulic testing or hydraulic parameter information that is needed by most practitioners. This study demonstrates

that with a simple transmissivity estimator and a reliable conceptual hydrogeological model to inform aquifer thickness assumptions, a less-rigorous but spatially extensive set of *K* estimates can be generated from domestic well specific capacity tests. The less-rigorous SC *K* estimates developed here broadly mirror *K* estimates made using high-quality methods at multiple scales despite the inherent differences in hydraulic testing and analysis. Although the two sets of *K* values do not match perfectly, the trends and distributions are sufficiently close (geometric means that vary by up to ~ 2.5 times) to support their incorporation. The compatibility of the two sets of *K* values for this study is much better than the order of magnitude level of error achieved with the empirical relationships developed by others for fractured carbonate rock aquifers (Huntley et al. 1992; Mace 1997).

Incorporation of the less-rigorous SC *K* into the high-quality *K* dataset is supported by scale-relevant comparisons so that areas where the less rigorous *K* estimates do not reflect the high-quality values can be identified. For example, the results of this investigation demonstrate that the SC *K* estimates do not mirror the high-quality *K* values at the low end of the *K* range, an artifact of the nature and purpose of the domestic wells versus monitoring wells, that must be considered. Detailed knowledge of the study area geology, as it relates to the effective aquifer thickness, improved the compatibility of the two sets of *K* estimates. Understanding the predominance of horizontally- dominant groundwater flow in relatively narrow channels is essential to the selection of an appropriate aquifer thickness for developing the SC *K* estimates in fractured bedrock.

Previous investigators have attempted to account for well losses in their estimation of transmissivity from specific capacity. In the authors' opinion, this level of refinement is not warranted. First, the parameters that are required to quantify well losses are generally not available. Second, the nonlinear component of the well losses is likely to be small at the pumping rates that are typical for domestic wells. The use of a simple relationship between transmissivity and specific capacity, like the one developed here, is more appropriate as it does not suggest an accuracy in the analysis that is unsupported by the available data. In this study, the significance of turbulent well losses has been assessed by considering data from a single, three-step test. For the data considered, the well losses had a negligible effect on the transmissivity estimate.

This study describes the development and testing of a simple and effective method for improving the coverage of *K* values between and beyond locations of high-quality hydraulic tests. The emphasis of this method is on making simple *K* estimates using low-cost and commonly available domestic well databases, and evaluating their compatibility with a more reliable, high-quality *K* dataset by conducting scale-relevant comparisons. The method generally consists of developing a linear relationship between *T*

and SC, applying this relationship to estimate *T* from SC for a large set of publically available domestic water well data, and converting these *T* values to *K* with knowledge of the aquifer, if desired. Comparisons between high-quality *K* values and those developed from domestic SC tests can be conducted to evaluate the reliability of the lesser quality *K* values for any purpose. In this investigation, it has been demonstrated that the SC *K* values are quite reliable, even at the geologic formation scale. Among many possible applications to groundwater characterization, practitioners can apply this approach for enhanced coverage of *K* values to help guide exploration for groundwater resources in areas that have not been developed extensively or to help place local-scale studies in their appropriate regional-scale context.

Chapter 3

Geologic Controls on Hydraulic Conductivity in a Karst-Influenced Carbonate Bedrock Groundwater System in Southern Ontario, Canada

3.1 INTRODUCTION

Exploring for groundwater supplies in Paleozoic carbonate bedrock is challenging, largely owing to spatial stratigraphic variability and the isolated and discontinuous nature of dissolution-enhanced features that have formed over different time scales. Despite these challenges, Paleozoic carbonate-dominated and karstic successions form important bedrock aquifers in North America (e.g., Rivera 2013; Ford 1987; Sun et al. 1997), and across the world (e.g., Chen et al. 2018). Conventionally, the nature of fracture networks within carbonate bedrock has been identified as having a significant influence on the occurrence of zones of high groundwater productivity and fracture distribution and has frequently been used to direct groundwater development (Singhal and Gupta 2010; Muldoon et al. 2001; Cooke et al. 2006; Michalski and Britton 1997; Parker et al. 2018). While incorporating the presence and associated influence of fracture features where applicable, this investigation identifies and quantifies the influence of three additional specific geological controls on the hydraulic conductivity of carbonate bedrock by integrating a large hydraulic conductivity dataset within a detailed, three-dimensional geological framework of Early Silurian carbonate bedrock of the Niagara Escarpment of southern Ontario, Canada (Figure 3.1). The uncommonly large set of hydraulic conductivity values compiled for this study permits a reasonably quantitative examination of the effects of geological features on hydraulic conductivity. In contrast, many previous studies have relied primarily on predictions derived from borehole logs and/or borehole geophysical tools (e.g., Muldoon et al. 2001; Brunton 2009; Perrin et al. 2011) or extrapolations of isolated hydraulic conductivity estimates to large study areas (e.g., Michalski and Britton 1997; Muldoon et al. 2001; Cole et al. 2009).

The three geological controls investigated here are: 1) proximity to bedrock valleys; 2) carbonate rock texture; and 3) sequence stratigraphic breaks. These three geological controls were selected for investigation because they have been interpreted, by borehole flow-profiling and heat-pulse logging (Lee et al. 2011), detailed core logging (Brunton 2009), sequence stratigraphic mapping (Brunton and Brintnell 2011; Brunton et al. 2012) and well capacity analyses (Cole et al. 2009) as comprising the most conductive groundwater flow features in the study area. Previous studies have identified one or more of these geological features as being a major control on hydraulic conductivity in similar carbonate bedrock sites across North America. The hydrogeological effects of increased fracturing in the stress release zone

at bedrock valley margins has been described for the Appalachian Valley in West Virginia, USA (Wyrick and Borchers 1981). The significance of rock textures, particularly in coarsely crystalline Paleozoic-age carbonate lithofacies, on the occurrence of highly conductive zones has been described for the Silurian dolomites of Milwaukee County, Wisconsin, USA, by Rovey and Cherkauer 1994 (a, b). Sequence stratigraphic breaks of varying duration have been identified as being the main control on flow zone occurrences in the Cambrian-Ordovician, carbonate-siliciclastic setting of Dane County, Wisconson (Meyer et al. 2016). Sequence stratigraphic breaks are generally horizontal and they have a mechanical component to their formation, similar to the bedding plane fractures described by others (Muldoon et al. 2001; Cooke et al. 2006; Michalski and Britton 1997). However, the duration of exposure at sequence breaks may span hundreds of thousands to millions of years and are often associated with physical and chemical erosion (paleokarst), such as those observed in the present study area (Brunton 2009).

Following an individual assessment of the three identified geologic controls on hydraulic conductivity in these carbonate rocks, they are subsequently assessed together spatially, within the geomorphologic and geological context of the region. This final integrative step is essential to provide insight into why hydraulic conductivity varies spatially with changes in geology and geomorphology, supporting the selection of local groundwater resource exploration targets. This study aims to investigate the relationship between hydraulic conductivity and these geologic characteristics of carbonate bedrock while developing an approach that can be adapted to similar karstic carbonate bedrock groundwater flow systems globally.

3.2 GEOLOGY AND HYDROGEOLOGY OF THE STUDY AREA

The approximately 600 km^2 study area lies on the eastern margin of a regionally-extensive Paleozoic bedrock cuesta known as the Niagara Escarpment (Figure 3.1a). The Lockport Group comprises, in ascending order: the Gasport, Goat Island, Eramosa, and Guelph formations, with the stratigraphy shown in (Figures 3.2a, 3.2b). The stratigraphic nomenclature presented in Figure 2 has evolved from older stratigraphic classifications (e.g. Armstrong and Carter 2010) to incorporate and reflect North American and global revisions of Early Silurian stratigraphy described by Brett (1995), Cramer et al. (2011) and Brunton et al. (2012). The most significant changes to the stratigraphic nomenclature in the Michigan basin is the adoption of the Lockport as a Group, which represents an extension of the lithologic and stratigraphic nomenclature revisions for the Appalachian Basin made by Brett (1995).

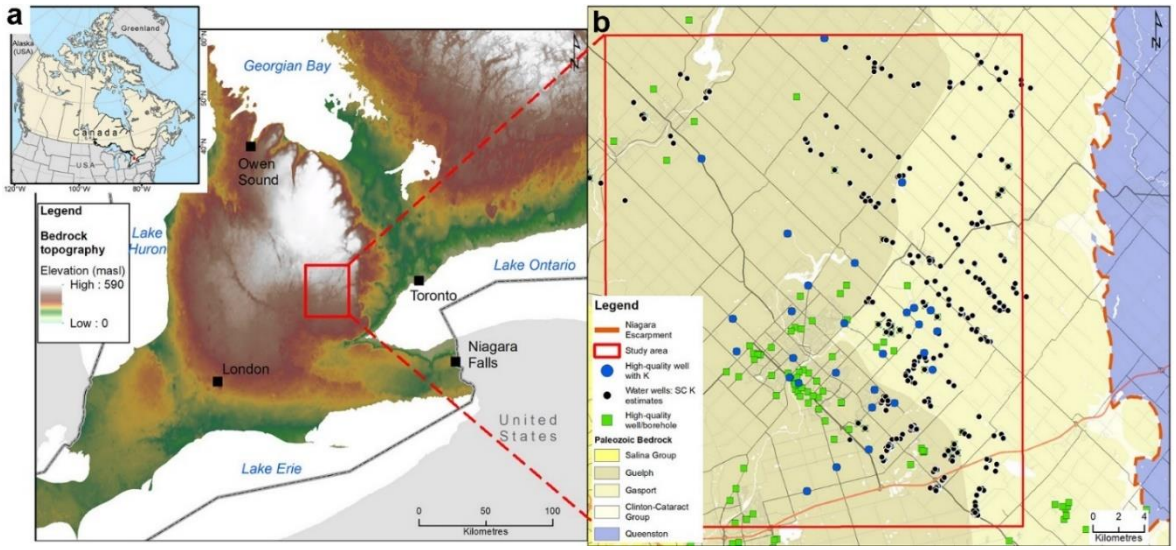

Figure 3.1. **a** The location of the study area (*red rectangle*) overlying the bedrock topography of southern Ontario. The Niagara Escarpment is evident just east of the study area, identified as a rapid drop in elevation. **b** Enlargement of the study area, showing the locations of the wells and boreholes associated with the geological and hydraulic conductivity data sets for this study. There are three types of wells represented in **b**; the high-quality wells/boreholes with detailed stratigraphic characterization are symbolized with *green squares* and *blue dots*. The *green squares* represent locations with detailed stratigraphic characterization and no high-quality *K* values. The *blue dots* represent locations with detailed stratigraphic characterization and high-quality *K* values. Wells with reconnaissance level *K* estimates developed from specific capacity tests are symbolized with *black circles*. All of these are shown overlying the top of the Silurian bedrock formations. The Niagara Escarpment is represented with an *orange dashed line along the right-hand side of the figure.*

The Lockport Group is an approximately 100 metre thick package of marine carbonates that display metre to decametre-scale shallowing-upward cycles and sequence stratigraphic breaks that are of variable hydrostratigraphic significance across the study area. The carbonate depositional cycles are largely the result of vertical (temporal) transitions from transgressive (open-marine) to regressive (more restricted marine) conditions on a formation-scale, with karstic intervals that vary spatially and temporally in relation to the sequence stratigraphic architecture (Figure 3.2a; Brunton et al. 2012). The stratigraphic variability and preservation of the Lockport Group is the result of a complex interplay between short-lived tectonic activity (tectophases – Ettensohn 1994), forebulge migration, paleogeography, sea level fluctuations and variable paleo-karstification (Ettensohn and Brett 1998, 2002; Brunton et al. 2012). Despite this complex interplay of tectonics and sedimentation, the strata display a predictable stratigraphic architecture that has been revealed through the detailed logging and sampling of cores and the examination of outcrops (Figure 3.1b; 3.2a).

Large bedrock valleys and/or re-entrants occur in the Paleozoic strata across much of southern Ontario, including the study area (Karrow 1973; Eyles et al. 1997; Gao 2011). The most commonly held view of their formation is polygenetic, with valleys initially having formed pre-glacially, resulting from millions

of years of physical and chemical erosion of vertical bedrock lineaments, and fractures that shaped the cuesta geomorphology. Following this, bedrock valleys were modified by physical and hydraulic carving or erosion by ice, subglacial meltwaters and subsequent variable infilling of Quaternary sediments during the past few million years of Laurentide ice sheet activity in southern Ontario (Straw 1968; White and Karrow 1971; Karrow 1973; Eyles et al. 1997; Sharpe et al. 2013; Bajc et al. 2017).

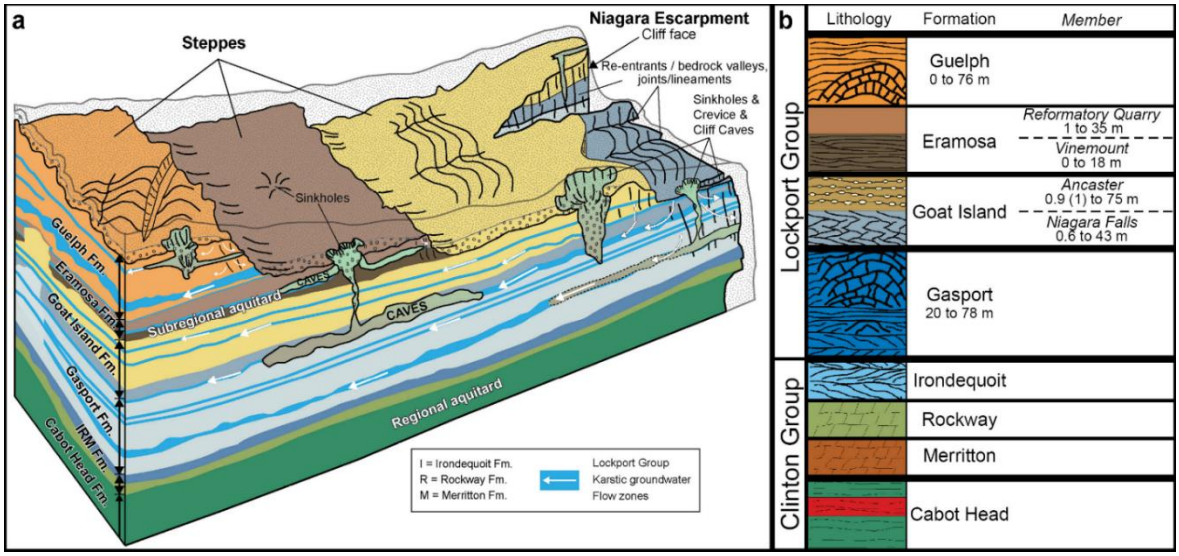

Figure 3.2. **a** A schematic of the conceptual hydrogeological model of the Early Silurian, Lockport Group carbonate bedrock of the Niagara Cuesta, presented in N-NE orientation. The geologic and geomorphologic features (e.g. bedrock formations, karst features) are not to scale, but are meant to capture the variety of bedrock and karst features observed within the study area. The Guelph and Eramosa formations tend to form smaller cliffs, or steppes, away from the main Niagara Cuesta scarp face. The schematic depicts more penetrative vertical joints/lineaments near the escarpment margin in the stress relief zone. Groundwater flow zones are depicted with white arrows. The development of the conceptual hydrogeological model is described in detail by Brunton (2009) and Brunton and Britnell (2011). **b** The stratigraphic section of the Early Silurian carbonate bedrock within the study area, with a range of thicknesses for each geological formation or member (modified from Brunton 2009).

The glacial sediments that overlie the bedrock in the study area comprise parts of the Guelph drumlin field and the Paris Moraine (Chapman and Putnam 1984). Overburden cover is thin or absent near the edge of the Niagara Escarpment and where bedrock topography is highest. In some areas, overburden cover may exceed 100 metres in thickness where it infills bedrock valleys like the Rockwood buried valley (Figure 3.2a; Greenhouse and Karrow 1994; Gao et al. 2006). Although some domestic overburden wells exist in the study area, the majority of domestic and municipal groundwater use is from the carbonate bedrock (Sharpe et al. 2013).

A conceptual hydrogeological model for the Lockport Group (Brunton et al. 2007; Banks and Brunton 2017) describes groundwater flow as occurring within discrete, horizontally-oriented features that represent sequence stratigraphic breaks of varying duration within formations or at formational contacts,

representing longer time breaks (Figure 3.2a). A number of the sequence stratigraphic breaks reflect the greatest contrast in depositional and diagenetic character of strata immediately below and above the sequence break, creating loci for dissolution enhancement (Brunton and Brintnell 2011). The Early Silurian sedimentologic, stratigraphic and tectonic history, specifically concerning how and when sequence breaks formed, provides an important context for understanding the present-day carbonate bedrock groundwater systems of the study area. Sequence stratigraphic models are difficult to establish for stacked carbonate successions deposited on the craton side of foreland basins, as is the case for this study area (*see* McLaughlin et al. 2008; Brett 1995, 1998; Brunton et al. 2012). Sequences are variably thick packages of sedimentary strata that record between 0.5 to 3 Ma intervals of the relative falls and rises of sea level and sediment deposition/erosion, and the interplay between tectonic uplift/subsidence, eustasy (global sea-level changes) and sedimentation (Vail et al. 1991; Ettensohn 1994; Brett 1995, 1998; Schlager 2005). In carbonate-dominated ramp depositional environments like that of the study area, sequences may be divided into three phases: the lowstand, transgressive, and high-stand systems tracts (Brett 1995, 1998; McLaughlin et al. 2008), each delimited below by a discontinuity, referred to here as a sequence stratigraphic break or sequence break. Intermittent tectonic activity caused the carbonate strata to be uplifted and eroded, resulting in the development of sequence breaks of varying duration (Brunton et al. 2012). Because sequence breaks can represent long breaks in deposition, the bedrock may display evidence of physical and chemical erosion (paleokarstification or diagenesis) prior to subsequent deposition of overlying geological units. These sequence stratigraphic breaks can often resemble bedding plane features, however, their formation tends to represent time breaks of generally greater duration than background marine deposition and storm-based (event bed) depositional processes.

These Early Silurian age Paleozoic strata are under a regional stress field, resulting from the slow westward plate tectonic movement of North America with the opening of the Atlantic Ocean, which began more than 200 Ma ago (Zoback 1992). Despite this, based on the compilation provided in Figure 25 in Armstrong and Carter (2010), there are no known faults crossing the Early Silurian bedrock of the study area. Over the past few hundred million years, differential erosion of younger Devonian and Late Silurian-age strata that were previously overlying the Early Silurian rocks of the study area, has resulted in the development of a series of broad arcuate karstic cuesta steppes within the Mid-Continent region of North America (Brunton et al. 2012). Stress relief or distress, in the form of penetrative vertical and horizontal fractures, joints, and crevices (extending through a number of formations) have formed proximal to the main Niagara Escarpment cliff face, and downdip in lower relief steppes, and along walls in re-entrants and bedrock valleys within the Niagara Escarpment cuesta (Figure 3.2a; see discussions in Ferguson and Hamel 1981; Gross and Engelder 1991; Eyles and Scheidegger 1995). All of the Early

Silurian dolostone units that make up the Niagara Escarpment and cuesta display evidence of vertical and subhorizontal brittle stress-relief or distressed fracturing (Kunert et al. 1998). The origin of some of the fractures and joints is difficult to discern due to the many possible mechanisms of their formation. Fractures and joints can result from mechanical breakage associated with the burial and subsequent erosion of overlying strata, as well as from horizontal plate tectonic-induced stress field (e.g. Baird and McKinnon 2007), or due to the last few million years of glacial loading and unloading (e.g. Straw 1968). Detailed examination of outcrops at the cuesta margin and within bedrock valleys on the cuesta steppes within the study area, combined with core examination, optical and acoustic televiewer and video logs of boreholes from more than one hundred wells (*see* Figure 3.1b for core locations), has revealed that the degree of vertical and horizontal mechanical fracturing decreases away from the Niagara Escarpment and bedrock valley walls into the competent bedrock (Figure 3.2a; Brunton 2009; Brunton and Brintnell 2011; Brunton et al. 2012). Borehole hydraulic investigations conducted in the study area including flow profiling, packer testing and conductivity profiling, has further revealed that the main groundwater flow zones in the Lockport Group occur predominantly at sequence breaks within the stratigraphic architecture and not within mechanical breaks (Brunton and Brintnell 2011; Lee et al. 2011).

The conceptual model of groundwater flow zones presented in Figure 3.2a forms the basis for local source water protection groundwater studies (e.g., Piersol and Petrie 2011; Matrix Solutions 2014). The less conductive units of the Lockport Group comprise the lower (Vinemount) member of the Eramosa Formation and the lower member of the Goat Island Formation (Niagara Falls) (Figure 3.2b; Brunton 2009; Brunton and Brintnell 2011). Vertical hydraulic conductivity estimates for the low hydraulic conductivity units range between 10^{-8} m/s to 10^{-9} m/s, inferred from the calibration of groundwater models (Matrix Solutions 2014). In contrast, the hydraulic conductivity estimates for the more conductive Lockport Group formations are as high as 10^{-2} m/s,but vary over a wide range ($\sigma_{\ln K} = 2.2$; Priebe et al. 2017a).

3.2.1 Karst in the Study Area

When investigating the groundwater resources in any carbonate setting, karst, referring to dissolution-enhanced (enlarged) features, must be a consideration. The presence of surface karst in the study area has been discussed for more than a century (e.g., Panton 1889; Weber 1960; MacGregor 1976; Kunert et al. 1998). Brunton and Dodge (2008) summarized the general distribution and character of karst along the Niagara Escarpment region of Ontario and noted that there is more extensive karstification near and along the edge of the scarp face. A similar observation was made by Cole et al. (2009), who observed evidence of karstificiaton in the bedrock at valley margins. Recent subsurface investigations conducted in the

study area, many of which have included video, optical and acoustic-televiewer logging, have revealed that dissolution-enhanced features are widely distributed to significant depths below the water table (Gautrey 2004; Brunton et al. 2007; Brunton and Dodge 2008; Cole et al. 2009; Brunton et al. 2012). It has been suggested that dissolution-enhanced features that comprise the main groundwater flow zones are limited to a thin zone at the bedrock surface (Perrin et al. 2011) and/or in a thicker zone in the middle of the Gasport Formation (Perrin et al. 2011 and Cole et al. 2009). Brunton (2009) identified karst features at particular stratigraphic positions throughout the Lockport Group succession, not just at the surface or middle of the Gasport Formation, and borehole flow testing revealed that many of these represent groundwater flow zones (Figure 3.2a). Despite all of the characterization work conducted in the area, groundwater flow features are not consistently present across the study area, which makes exploring for groundwater resources a challenge (David Belanger, Water Supply Program Manager, City of Guelph Water Services Department, personal communication, 2017).

3.3 METHODS

3.3.1 Development of Two Sets of Variable-Quality Hydraulic Conductivity Estimates

Two sets of hydraulic conductivity (*K*) values have been used for this investigation. The first is a high-quality dataset comprising 71 *K* values developed from the analysis of hydraulic testing conducted in 32 monitoring wells (Figure 3.1b, *blue circles*). Detailed geological characterization was conducted for the 32 monitoring wells associated with the high-quality *K* dataset. The hydraulic tests analyzed to make the high-quality *K* dataset include single-hole pumping and slug tests that were conducted in short-interval monitoring wells or in discrete intervals of the rock isolated between packers. Hydraulic test intervals ranged from 3m to 10m. Pumping test analyses were conducted with the Cooper-Jacob (1946) method, with diagnostic insight provided by the derivative curve to ensure that the solution was matched to the portion of the data during which conditions approximated an infinite-acting, radial flow regime. Slug test analyses were conducted with the method of Cooper, Bredehoeft and Papadopulos (1967). Where a good match could not be achieved with this method, the Bouwer and Rice (1976) solution for a fully penetrating well in confined aquifer was used. Detailed descriptions and the complete analyses for each *K* value in the high-quality data are provided in Priebe et al. (2017a).

A second set of reconnaissance-level *K* estimates was generated to enhance the spatial coverage of *K* values across the study area beyond the coverage provided by the high-quality *K* dataset. The second set of *K* values was developed using the specific capacity (*SC*) data from domestic water wells, following the approach described by Priebe et al. (2017b). The compatibility of the two *K* datasets was assessed by

comparing the cumulative probability distributions of the two sets of *K* values (Figure 3.3). These cumulative probability plots were created using methods described by Helsel and Hirsch (1992), whereby the log *K* values were ranked and plotted against the standard log-normal distributions. As shown in Figure 3.3a, the two sets of *K* values match well at the high *K* range, but not at the low *K* range, below 10^{-5} m/s. In Figure 3.3b, the low *K* values (< 10^{-5} m/s) for the high-quality dataset have been removed and the cumulative probability distribution re-plotted. This truncated version of the high-quality *K* dataset provides an excellent match to the distribution of the *SC K* estimates (Figure 3.3b). The difference between the two datasets arise because the domestic wells associated with the *SC K* estimates must encounter sufficient yield for the domestic user and therefore the set of *SC K* estimates does not have any low *K* values. The high-quality data include *K* estimates on all strata, including low-yield zones, leading to some *K* estimates in the low range. Removing the low *K* values from the high-quality *K* dataset levels the two sets of values. From these comparisons, it is clear that the *SC K* data provide reliable reconnaissance-level estimates that reflect the ranges and distributions observed in the high-quality *K* data set for $K > 10^{-5}$ m/s.

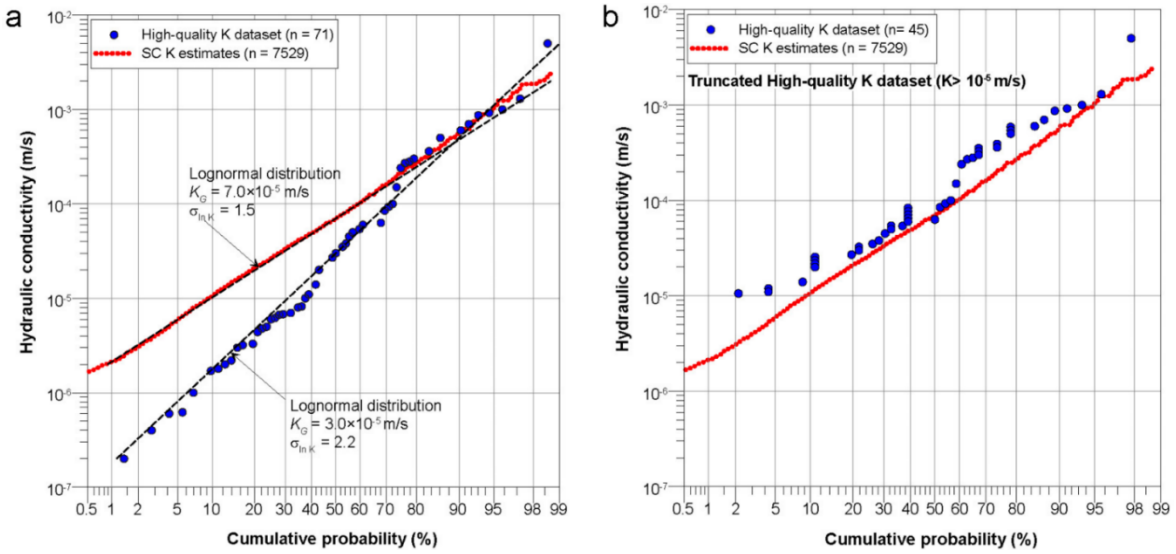

Figure 3.3. **a** The cumulative probability distributions for the *SC K* estimates (*red symbols*) and the high-quality *K* dataset (*blue symbols*). The normal distribution lines for both sets of estimates are presented as dashed black lines**.** **b** The cumulative probability distributions for the *SC K* estimates (*red symbols*) and a truncated version of the high-quality *K* dataset to remove conductivity tests below 10^{-5} m/s (*blue symbols, stacked to show duplicates*) for improved compatibility (modified from Priebe et al. 2017b)

Supported by the good correlation presented in Figure 3.3, the *SC K* estimates significantly enhance the spatial coverage of the high-quality *K* dataset (Figure 3.1). Because this is an investigation that focuses on aquifer geological features associated with high *K*, incorporation of these reconnaissance-level values is not detrimental to the outcome of the assessments.

3.3.2 Geological Characterization

The stratigraphy for 177 high-quality boreholes and wells (*green squares and blue dots* in Figure 1B) was confirmed using a combination of core logging (utilizing principles of sedimentology, stratigraphy, rock characterization, paleoecology, sequence stratigraphy, biostratigraphy, chemostratigraphy and lithogeochemistry), review of down-hole camera videos, incorporation of optical and acoustic televiewer, geophysical (gamma) logs, as well as carbonate petrography. The carbonate rock texture of each formation within the Lockport Group is reported in Brunton (2009).

3.3.3 Identification of Buried Bedrock Valleys

Previous maps of buried valley locations have been made at various scales in and around the study area (e.g., Karrow 1973; Eyles et al. 1993; Greenhouse and Karrow 1994; Gao et al 2006; Gao 2011). The development of these maps relied to a lesser extent on geophysics for valley mapping and to a larger extent on interpretations made from surface features (e.g., outcrops) or on public well information of variable quality from more than a decade ago. For this investigation, a new bedrock topographic surface was generated using the most recent subsurface information to support the identification of buried bedrock valleys and the mapping of previous workers was used to inform the interpretations. The bedrock topographic surface was created using two datasets: the database of domestic water well records (WWRs) from the Ontario Ministry of Environment and Climate Change, and the high-quality geological dataset of 177 boreholes and wells of this investigation. Prior to use, the approximately 50,000 bedrock wells in the WWR within the study area were vetted using a series of queries to eliminate wells with incorrectly reported lithologies (e.g., granites), locations (e.g., incorrect township) and errors in units of measurement (e.g., the database reports depths in metres, and the WWR reports depths in feet). The vetting process was conducted iteratively, generating and improving upon the bedrock surface by evaluating and correcting, or eliminating individual records in areas where the interpolated bedrock surface showed unreasonably steeply sloped topographies (slopes >10%). Careful evaluation of each WWR was undertaken in areas where the steeply sloping interpolated bedrock surface coincided with areas where bedrock valleys had been mapped by others or where the general orientation of potential valleys matched that of the valleys already mapped by others (Karrow 1973; Eyles et al. 1993; Gao 2011). The WWR vetting process resulted in the elimination of approximately 50% of the wells in the study area, and the manual correction of approximately 1000 individual records, leaving 25,000 WWRs for bedrock surface interpolation. Once the bedrock surface interpolation was completed with WWRs, it was further refined with the incorporation of the 177 high-quality wells and boreholes of this investigation.

The inverse-squared distance-weighted (IDW) method of the standard nearest neighbour type (Watson & Philip 1985), was used to generate the interpolated bedrock surface. The advantage of this method lies in its ability to control the influence of distance between points on the surface rather than smooth them out. Early attempts to generate the surface by kriging resulted in a surface that smoothed the abrupt changes in bedrock topography associated with bedrock valleys, whereas the IDW method preserved these anomalies to a greater extent. In the northern half of the study area, the depths and locations of buried bedrock valleys were further confirmed by the work of Burt and Dodge (2016), which incorporated seismic refraction lines orthogonal to a presumed valley position and deep overburden drilling when generating their modeled bedrock surface.

Buried valley thalwegs (i.e., the lines connecting the deepest parts of the bedrock valley) were first identified manually from the IDW interpolated bedrock surface. Following this, the thalweg positions were confirmed, where possible, by identifying individual WWRs that penetrate deeply in overburden without encountering bedrock. After the buried bedrock valleys were mapped, the depth and stratigraphic position of thalweg penetration was assessed using the detailed stratigraphic descriptions provided in 21 cross-sections, each cut orthogonally to one of the valleys. The stratigraphic picks of the 177 high-quality wells and boreholes form the geological foundation for this interpretation.

Although the stratigraphy for the high-quality *K* dataset is known, the stratigraphy for the wells associated with the *SC K* values is not. To assess the influence of buried valleys on hydraulic conductivity for each stratigraphic formation, the stratigraphy of the WWRs of the *SC K* values were assigned by reviewing the WWRs within the nearest of the 21 cross-sections. The *SC K* values were assigned a stratigraphic formation by tying the elevation of the 'water found' position, from the WWR, to the stratigraphy at that same elevation. The "water found" position marks the elevation where the water well driller encountered significant groundwater flow, usually signalling that an adequate domestic water supply had been encountered (Ontario 2015).

3.4 RESULTS

The two sets of *K* values, the *SC K* and the high-quality *K*, are used selectively to test the influence of fracturing near buried bedrock valleys, carbonate rock texture and sequence stratigraphic breaks on *K*. Table 3.1 outlines which sets of *K* values were used to investigate each of these three geological controls.

Table 3.1. Summary of the source and number (*n*) of hydraulic conductivity (*K*) values used for each component of the investigation.

Source	*SC K* values (*n*)	High-quality *K* values (*n*)
Bedrock valley investigation	279	71
Carbonate rock texture investigation		71
Sequence stratigraphic breaks		40

3.4.1 Evaluating the Influence of Fracturing and Dissolution Enhancement Near Buried Bedrock Valleys on K Distribution

For the buried valley component of the study, the influence of proximity to buried valley on *K* is investigated. Previous studies (Wyrick and Borchers 1981) and site observations (Brunton et al. 2012) indicate that increased fracturing in the stress release zone in bedrock at valley margins might increase *K* in these areas. These fractures could have been conduits for water flow, promoting karst development in these features, as was suggested for the area by Cole et al. (2009).

Five bedrock valleys were identified during the bedrock topographic mapping (Lines A to E in Figure 3.4). With the exception of one in the southeast that is oriented southeast to northwest (valley E), all of the identified buried bedrock valleys follow the same northeast to southwest orientation. The northeast to southwest orientation of the bedrock valleys is orthogonal to the underlying Michigan rift zone and generally sub-parallel to the Algonquin Arch (Eyles and Scheidegger 1995), which has been more recently described as the forebulge migration zone (Brunton et al. 2012). The trend is likely a response to the regional tectonic stress field in the Precambrian basement structures, which controls the joint set and valley orientations in these brittle carbonates (Baird and McKinnon 2007; Brunton et al. 2012).

In the northwest portion of the study area, at valleys A and B, the Guelph Formation sub-crops and the valley thalwegs penetrate to the contact between the Guelph Formation and either the underlying Goat Island or Eramosa formation, depending on location. The thalwegs of valleys C, D and E, in the eastern portion of the study area, appear to penetrate to different stratigraphic positions within the Gasport Formation. Cole et al. (2009) identified a correlation between well capacity and proximity to buried valley C, the Rockwood buried valley.

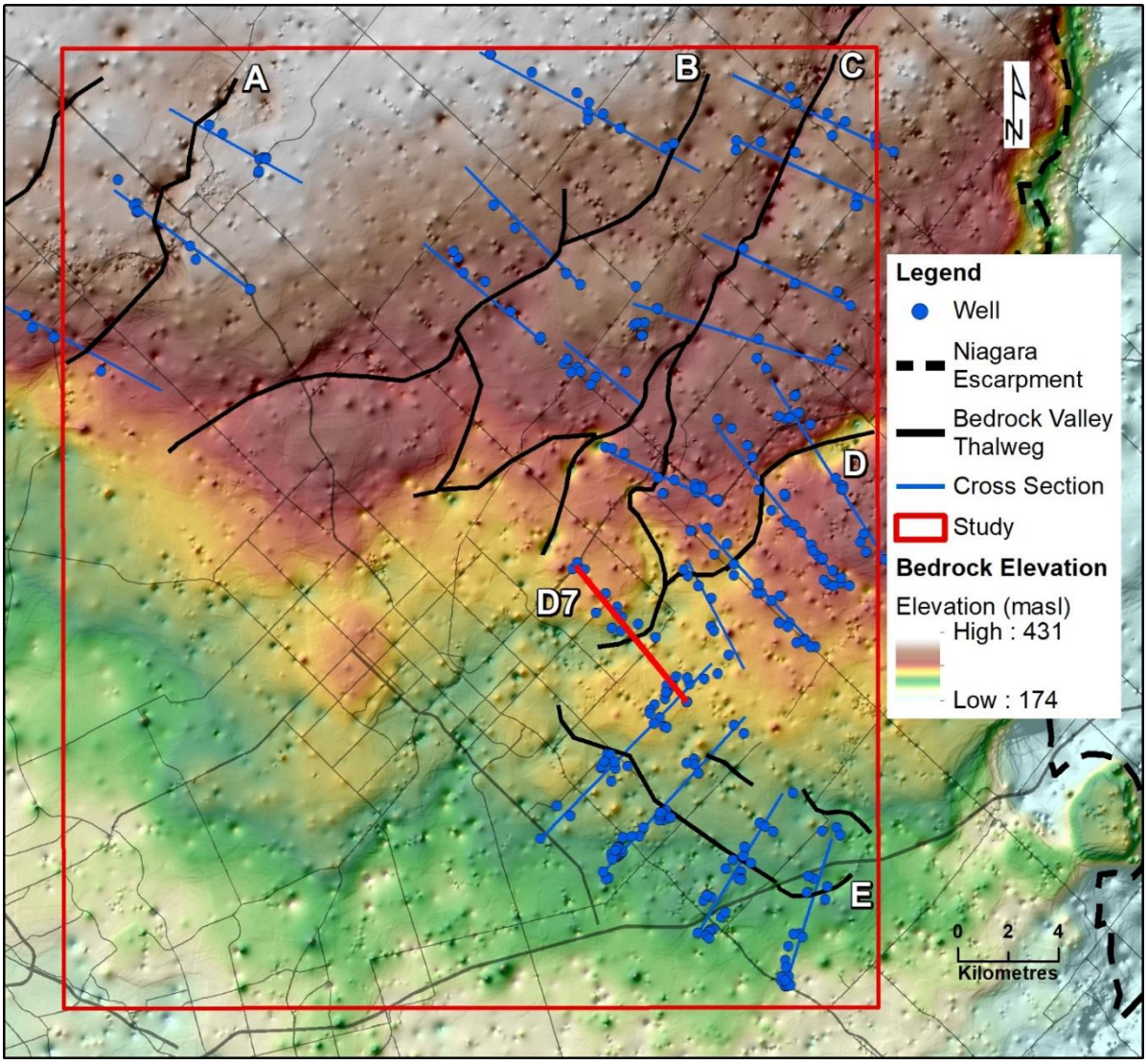

Figure 3.4. The interpolated bedrock surface and the delineation of buried bedrock valleys for this study, indicated with *black lines*. The buried bedrock valleys are labelled A through E, clockwise from the northwest. Twenty-one cross-sections have been drawn perpendicular to the buried bedrock valleys, and these are represented with *blue lines*. The wells used to construct the cross sections are presented as *blue circles* and are either monitoring wells or domestic wells. They are used to assess the influence on *K* of proximity-to-thalweg. Cross-section D7, presented in Figure 5, is shown as a *red line*.

Cross-section D7 (Figure 3.5) is presented as an example of the 21 cross-sections developed for this investigation, with its location shown on Figure 3.4 (*red line*). The deepest of the well driller's "water found" positions is represented for each well with a horizontal *black bar*, and these appear to be concentrated in a ~20 m thick zone in the middle of the Gasport Formation, with approximately 15 m of Gasport Formation above this zone. This ~ 20m thick interval is indicated in Figure 3.5 by the *transparent rectangle*. From Figure 3.5, it appears as though there is no consistent elevation or stratigraphic position within the geological formation at which a major groundwater flow zone occurs.

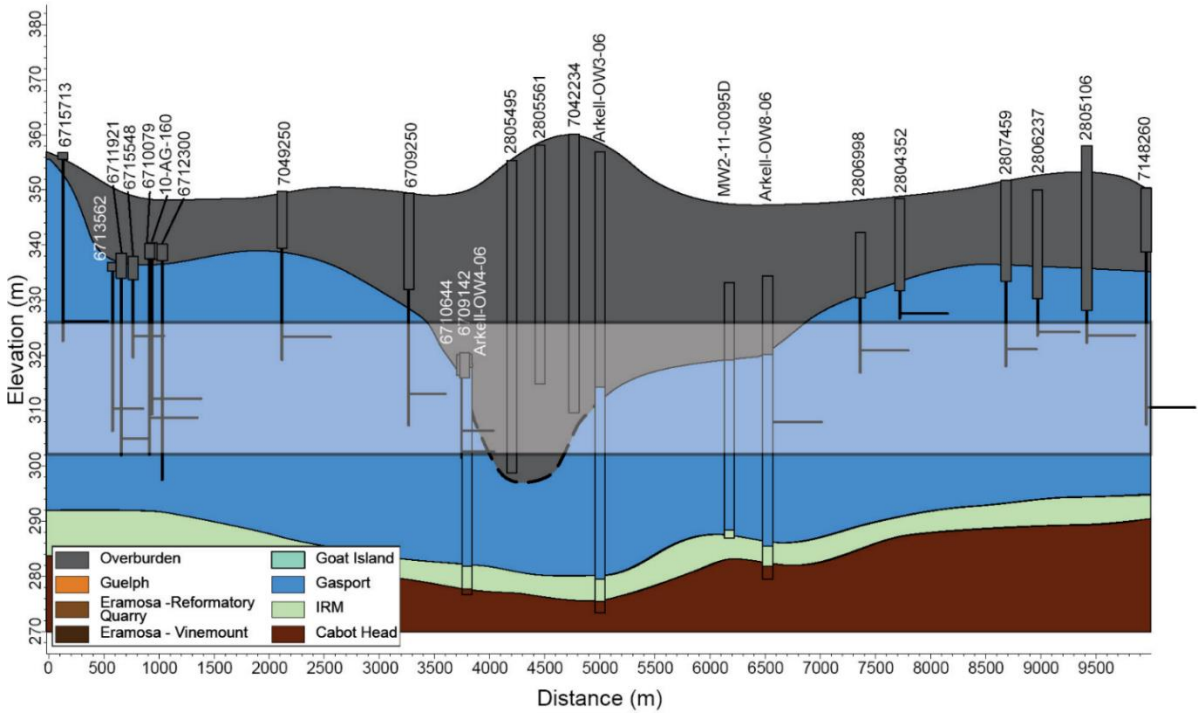

Figure 3.5. Cross-section D7 is one of the cross-sections generated for valley D, with the location shown on Figure 3.4. All cross-sections were generated using a 1 km buffer on either side of the surface trace of the cross section within which all wells with associated *K* estimates were included. The *horizontal black bar* at each well marks the depth of the "water found" position from the domestic water well records, with all of these encompassed within the *transparent rectangle*. Deep overburden wells located in the modelled valley helped to constrain the position of the valley thalweg. Modified from Priebe et al. (2017b)

The top of the Gasport Formation has been described in the study area as a productive aquifer, consisting of weathered and incompetent rock (Perrin et al. 2011) and the Early Silurian carbonate bedrock has been more broadly described as such regionally (Singer et al. 2003). However, based on Figure 3.5, the top of bedrock does not appear to form the main groundwater producing zone, but rather, most domestic wells are drawing water from deeper within this geologic unit. Domestic wells in the bedrock adjacent to the other four valleys also show a trend of deeper 'water found' positions, with domestic wells extending well below the bedrock surface (Table 3.2). A summary of the findings from each valley is presented in Table 3.2 with some general observations.

Table 3.2. Summary of stratigraphic position of the valley thalwegs

Valley ID	Stratigraphic position of valley thalwegs	'Water found' position trend	Deepest elevation in each valley (masl)
A	Within the Guelph Formation, or at the contact between the Guelph and Goat Island formations	Bottom of the Guelph Fm (*n* = 16 wells)	330
B	At the contact between the Guelph Formation and the underlying formation (either Eramosa or the Goat Island formation, depending on location).	Bottom of the Guelph Fm (*n* = 20 wells)	345
C*	In the north, the valley thalweg extends to the base of the Guelph Formation where it is the sub-cropping formation. In the southern part of this valley, the Guelph Formation is not present, and the thalweg reaches the bottom of the Gasport Formation.	Middle to bottom of the Gasport Fm (*n* = 47 wells)	295
D	The middle of the Gasport Formation.	Middle of the Gasport Fm (*n* = 70 wells)	310
E	At the contact between the Gasport Formation and the overlying formation (either the Eramosa or the Goat Island formation, depending on location).	Gasport Fm contact (*n* = 77 wells)	290

*Valley C is the same as the Rockwood Valley described by Cole et al. (2009)

The relationship between *K* and the proximity of bedrock wells to the valley thalwegs is assessed in Figure 3.6 for valleys A-E. Best-fit lines are included only where a trend can be inferred, to facilitate an assessment of the relationship between *K* and distance from thalweg for each valley. From the plots in Figure 3.6, it is clear that there is significant variance in the *K* values for the wells near each valley, and that this variance is not well accounted for with a linear regression model. Very weak correlations are shown for valley A and valley B, with very low correlation coefficients. These poor correlations could be caused by the relatively small number of *K* values available for these valleys, compared with those for the other valleys. The sets of *K* values shown with distance from the thalwegs of valleys C, D and E are too scattered to approximate any trends. Based on the results presented in Figure 3.6, there is no clear trend of increasing well capacity with proximity to valley, contrary to the suggestion of Cole et al. (2009) related to the Rockwood buried valley (valley C).

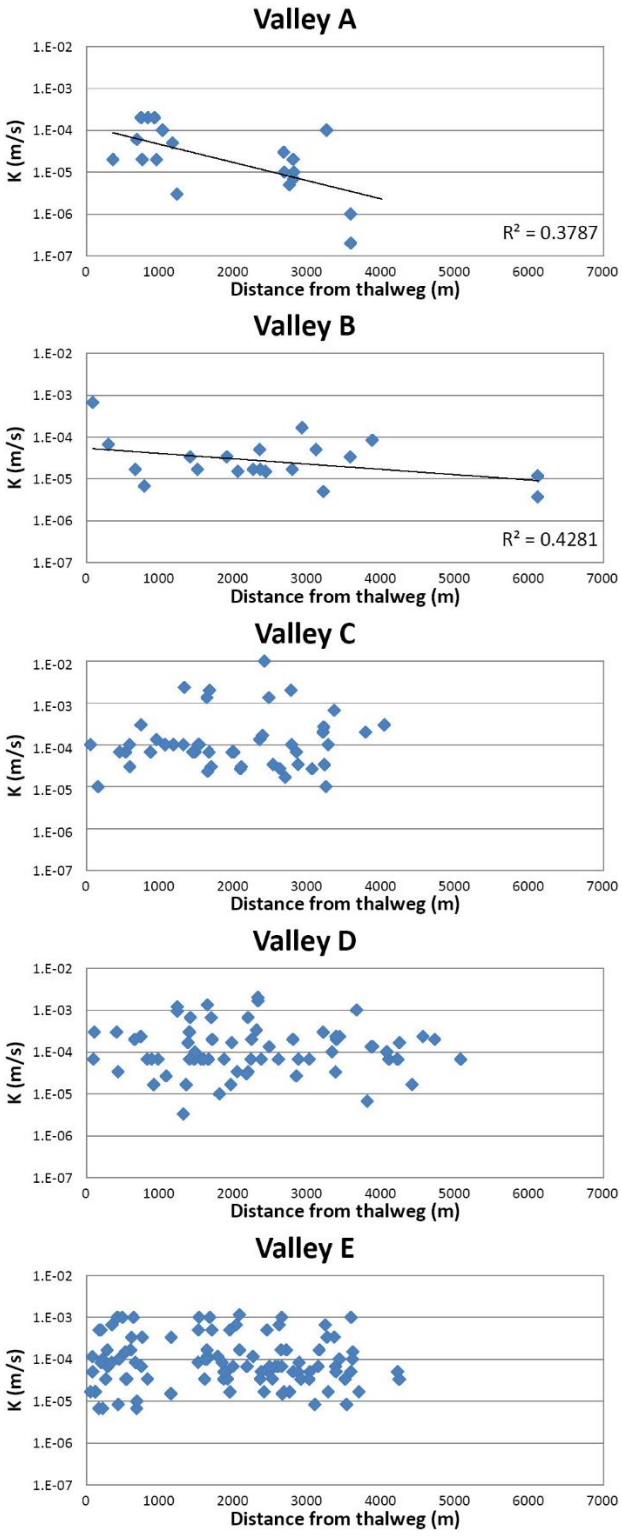

Figure 3.6. Hydraulic conductivity values (*K*, m/s), estimated from hydraulic tests conducted in bedrock wells plotted against orthogonal distance between each well location and the axis of the nearest buried valley. This is done for each of the five valleys (A through E). The valley locations are shown on Figure 3.4.

The greatest *K* values are observed for wells adjacent to valleys C D and E, which penetrate to the middle and base of the Gasport Formation, respectively (Table 3.2). Although the geometric mean *K* values are the same for valleys C and D (K_G = 1x10^{-4} m/s), valley C has a much higher *K* variability yielding an order of magnitude greater standard deviation (2x10^{-3} m/s) than valley D. A lower *K* tendency is observed for bedrock wells in the Gasport Formation adjacent to valley E (K_G = 8x10^{-5} m/s), which only penetrates into the upper Gasport Formation. The results of this assessment have shown that there is no evident influence of buried valleys on *K* distribution in adjacent carbonate bedrock. Instead, what has been observed is variability in *K* trends between different geological formations, with the Gasport Formation showing the highest *K* trend. The absence of influence of valley proximity on K may be related to infilling of the enhanced fracture zone at the valley margin with glacial sediments.

Prior to infilling with glacial sediments, bedrock valleys were conduits for dissolution-enhancement. The more deeply a valley is incised, the greater the opportunity for karst development across a wider portion of the bedrock formations adjacent to that valley, such as the deep karst described by Kunert et al (1998) and Cole et al. (2009) for valley C. According to Dreybrodt (1996), under large hydraulic gradients, such as those generated toward a deep valley channel or away from a tall glacier, dissolution-enhancement can result in dramatic enlargement of primary and secondary porosity, with the greatest dissolution occurring at the discharge location. Although no direct trend between *K* and proximity to bedrock valleys was identified here, the role of bedrock valleys as conduits for dissolution enhancement remains a factor for consideration when assessing spatial trends in *K* across the study area.

3.4.2 Evaluating the Influence of Carbonate Rock Texture on K Distribution

The influence of carbonate rock texture on *K* distribution is evaluated by comparing the cumulative probability distributions of *K* for each individual Lockport Group formation. Only the high-quality *K* dataset is used for this assessment (*see* Table 3.2). The *SC K* estimates were excluded for this investigation because the stratigraphic characterizations for those wells are not as accurate as those for the high-quality *K* dataset. Although there is some overlap in textures between formations (e.g, the Gasport, basal Goat Island, and Guelph formations all contain lithofacies with coarsely crystalline textures), each formation has a sufficiently distinct combination of rock textures for this investigation to be instructive. Probability distributions of *K* for the Lockport Group formations are shown in Figure 3.7, with statistics presented in Table 3.3 alongside texture classifications and lithofacies descriptions.

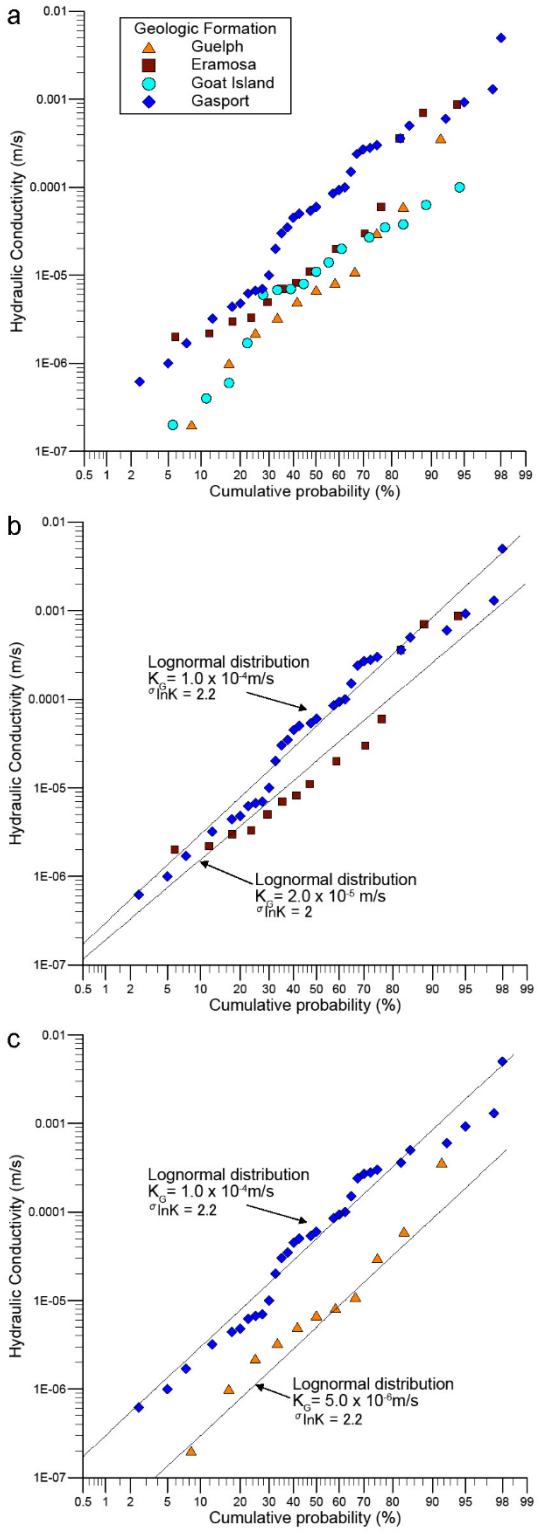

Figure 3.7. **a** The cumulative probability distribution of *K* values for each of the Lockport Group formations, with the legend showing the formations in descending order of depth**.** **b** A comparison of the cumulative probability distributions of *K* for the Eramosa and Gasport formations. **c** A comparison of the cumulative probability distributions of *K* for the Gasport and Guelph formations.

The cumulative probability distributions of *K* for each of the formations are similar, despite differences in rock texture (Figure 3.7a). Each *K* distribution approximates a log-linear trend, indicating log-normal distributions, which is the commonly observed trend for *K* datasets (Neuman 1982). The Gasport Formation, with the most uniformly coarsely crystalline texture, has the highest associated *K* values (Figure 3.7 a,b,c) as well as the highest geometric mean *K* ($5x10^{-5}$ m/s) (Table 3.3). The cumulative probability distribution of *K* for the most uniformly fine-textured formation, the Eramosa, appears to be very similar to that of the distribution for the Gasport Formation (Figure 3.7b) despite texture differences. The Eramosa Formation also has the second highest geometric mean *K* of all of the formations ($2x10^{-5}$ m/s) (Table 3.3). The Guelph Formation, with textures ranging from coarsely crystalline in the basal reef mound phases, to finely crystalline in upper lagoonal cycles, has the lowest *K* distribution of the Lockport Group formations and also the lowest K_G ($5x10^{-6}$ m/s). The two Lockport Group formations with the most distinctly different *K* distributions are the Gasport and Guelph formations (Figure 3.7c), with K_G values for these two datasets differing by an order of magnitude (Table 3.3). Standard deviations are similar for all formations, regardless of the uniformity of their textures (Table 3.3).

Table 3.3. Texture descriptions and statistics from lognormal cumulative probability distribution of *K* for each Lockport Group formation.

Lockport Group Formation.	Sample number	Standard Deviation (ln K)	Geometric Mean K (m/s)	Carbonate Texture, by Formation and Member (from Brunton 2009)	Lithofacies descriptions (from Brunton 2009)
Guelph	11	2.2	$5x10^{-6}$	Fine to coarsely crystalline: lagoonal wackestone and crinoidal grainstone	Sponge and crinoidal reef mounds, overlain by lagoonal carbonate muds.
Eramosa	17	2.0	$2x10^{-5}$	Fine to medium crystalline (Reformatory Quarry Member): lagoonal wackestones and mudstones	Stromatolitic facies overlain by hummocky/swaley cross-stratified deposits with small reef mounds.
Goat Island	20	2.0	$7x10^{-6}$	Coarsely crystalline (Niagara Falls Member) to finely crystalline (Ancaster Member)	Niagara Falls Member consists of a well cemented crinoindal grainstone. The overlying Ancaster Member is thin to medium bedded, and sponge-bearing.
Gasport	40	2.2	$5x10^{-5}$	Coarsely crystalline: packstone to grainstone	Shallowing upward cycles consisting of well cemented crinoid-tabulate coral mounds overlain by shelly coquina reefs in some locations.

The higher *K* values for the Gasport Formation, compared with the other formations, can likely be partially attributed to matrix dissolution with its coarse texture, a trend that was observed in coarse textured rocks investigated by Rovy and Cherkauer (1994a). However, if coarse textures were the only

cause of high *K*, the *K* distribution for the Gasport Formation would only contain high *K* values, which would have resulted in a small standard deviation. The large standard deviation of *K* for the Gasport and Eramosa formations, despite their uniform coarsely crystalline and finely crystalline textures respectively, suggests factors (e.g. fractures, karst features) beyond just texture are influencing the *K* trends. Brunton (2009) observed significant karst dissolution along bedding plane fractures in the Reformatory Quarry Member of the Eramosa Formation, the prevalence of which having been attributed to its uniform, finely crystalline texture. For the Gasport Formation, the high *K* trends may be associated with either the dissolution of the coarse textured bedrock, or associated with paleokarstic sequence boundaries which have been identified as main flow zones in this formation (Brunton 2009; Brunton and Brintnell 2011). The results of this integrative texture and *K* investigation suggest that although rock texture likely influences *K*, it is not clearly the only or the most significant factor controlling *K* trends of the Lockport Group formations. These results are in contrast to the investigations of Rovy and Cherkauer (1994 a,b), who determined that texture was the primary controlling factor on *K*, and that the coarsest textured carbonates were associated with the highest hydraulic conductivities.

3.4.3 Evaluating the Influence of Sequence Stratigraphic Breaks on Hydraulic Conductivity Distribution

The Gasport Formation was selected for this part of the investigation because it exhibits variability in the distribution and character of karstification at sequence stratigraphic breaks, offering a good opportunity to test the influence of this phenomenon on *K* values. The Gasport Formation is also the most important bedrock water supply source for the local municipality, the city of Guelph (Brunton et al. 2007; Piersol and Petrie 2011). Hydraulic conductivity varies significantly within the Gasport Formation (Priebe et al. 2017a), as does the productivity of existing municipal supply wells, making the siting of new wells in this formation challenging (David Belanger, Water Supply Program Manager, City of Guelph Water Services Department, personal communication, 2017).

In the southeast portion of the study area, the Gasport Formation comprises two kinds of reefal facies, described by Brunton (2009) as well-cemented crinoidal-packstone and tabulate coral reef mound cycles that are capped by karstic and bleached shelly coquina lithofacies. In core samples, the sequence stratigraphic breaks at the tops of the shelly coquina reef cycles show evidence of karst (Brunton 2009). Groundwater flow is conceptualized as being concentrated at the sequence breaks atop each package of these reef cycles (Brunton 2009). In the northwest portion of the study area, the Gasport Formation comprises well-cemented crinoidal reef mounds but without the shelly coquina reef facies, nor the karst development observed in the southeast.

This analysis was conducted with the high-quality *K* dataset, which consists of forty *K* estimates for the Gasport Formation (Priebe et al. 2017a). The *K* values for the Gasport Formation are shown spatially, in plan view, with the change in sequence breaks marked with a *dashed blue line*, separating the study area into southeast and northwest (Figure 3.8). Hydraulic conductivity values are generally greater in the southeastern portion of the study area than they are in the northwest. The spatial occurrence of high *K* values in the southeast roughly correlates with the limit of dissolution enhanced, often paleokarstic, sequence breaks at the shelly coquina reef tops in the same area (dashed line, Figure 3.8).

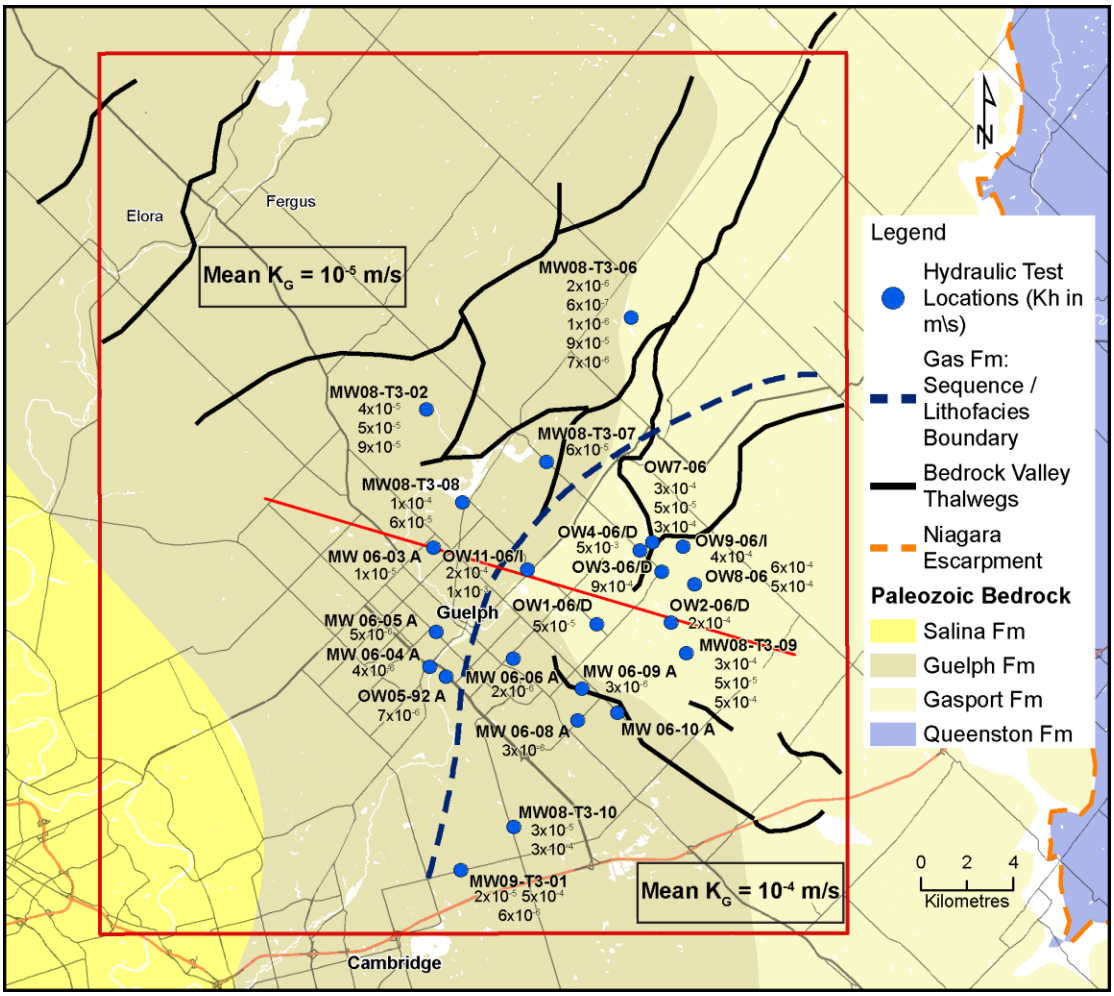

Figure 3.8. Hydraulic conductivity values in the Gasport Formation, in m/s, are shown with well locations symbolized with *blue circles*. Where more than one *K* value is presented for one well, these *K* values have been estimated from multiple packer tests conducted in that well. The *K* values are superimposed on the Paleozoic stratigraphy. The *dashed blue line* denotes the inferred change in sequence stratigraphy and lithofacies, separating the study area into northwest and southeast areas. The red line shows the location of the cross-section presented in Figure 3.10.

The cumulative probability distributions of *K* values for the Gasport Formation in the northwest and southeast are compared in Figure 3.9, with two distinct distributions observed (Figure 3.9). The geometric means of the two log-normal *K* distributions differ by an order of magnitude (Figure 3.9). The standard deviation for the southeast log-normal *K* distribution (σ_{lnK} = 2.2) is larger than the value for the northwest values (σ_{lnK} = 1.7). Although *K* values for the southeast can be as low as those observed in the northwest, *K* values greater than 10^{-4} m/s are only observed for the southeast.

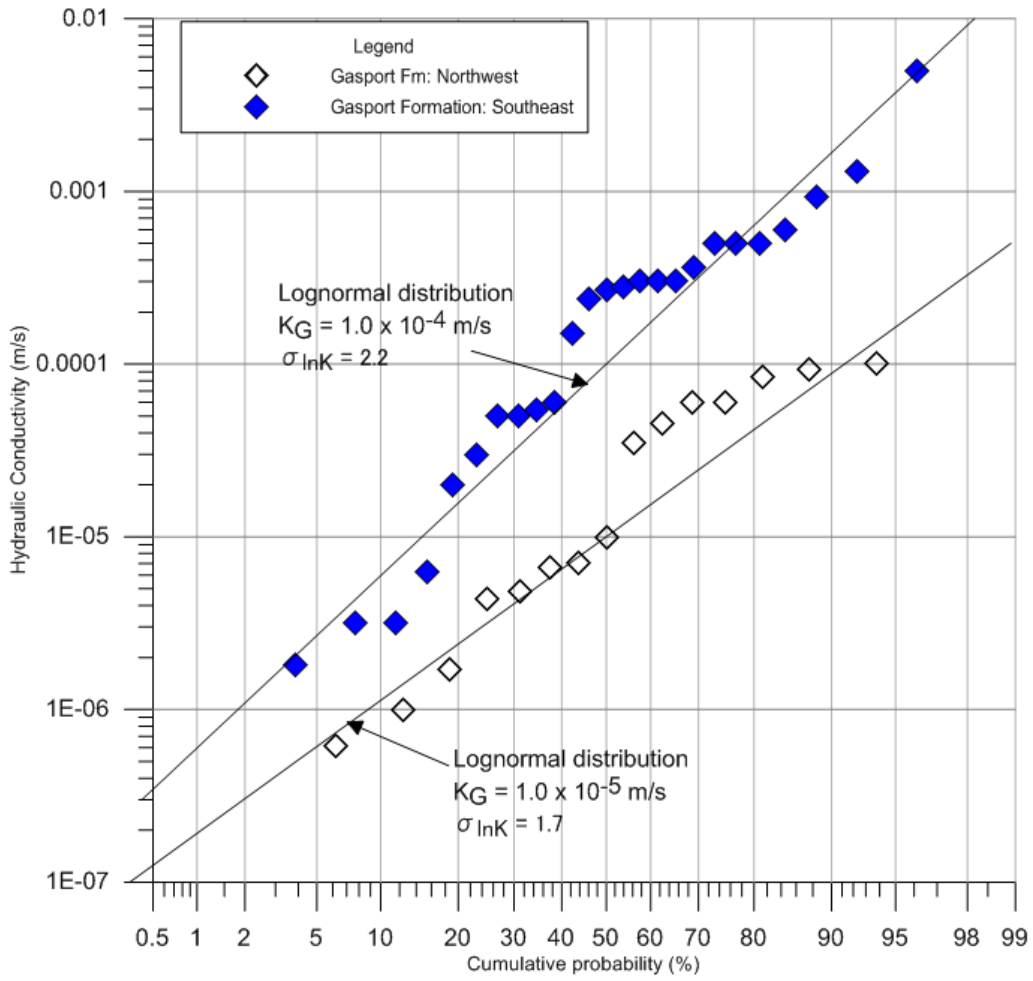

Figure 3.9. Cumulative probability distributions of *K* within the Gasport formation using the high-quality *K* dataset, with values identified by northwest (*open diamond* symbols) and southeast (*blue diamond* symbols) areas.

The data presented in Figure 3.9 show that there is a greater probability of encountering higher *K* bedrock in the southeast portion of the study area than in the northwest. The two characteristics unique to the southeast, compared with the northwest, are the presence of the shelly coquina facies and the occurrence of paleokarst surfaces at sequence stratigraphic breaks within these facies. The higher *K* values in the southeast can be attributed to the presence of these karstic sequence stratigraphic breaks, and not the coarser grain size associated with the shelly coquina facies itself. The relationship between permeability and carbonate rock texture, as developed by Lucia (1983), suggests that the slight change in texture observed between the two Gasport Formation facies, crinoids in the northwest (packstone texture) and shelly coquinas in the southeast (grainstone texture), would not, of itself, result in a permeability change large enough to cause the observed significant differences in *K* between these two areas.

3.5 EVALUATING THE COMBINED INFLUENCE OF GEOLOGICAL FEATURES ON K DISTRIBUTION

The three geological features that have been investigated individually so far, are now evaluated together to assess their combined influence on *K* distribution in the Gasport Formation. To facilitate this, the cumulative probability distributions of *K* in Figure 3.9 are described within the context of Figure 3.10, which is a northwest to southeast oriented cross-section A-A' with location indicated by the red line in Figure 3.8. As shown in Figure 3.9, the *K* profile in the southeast is higher than in the northwest, with values in the northwest never exceeding 10^{-4} m/s in contrast to the southeast where most do. In the previous section, this is attributed to the karstic sequence stratigraphic breaks. However, when considered within the geomorphological context of the study area, it becomes evident that many geological controls are contributing to the observed high *K* trend. The differing *K* distributions between the southeast and northeast can be partially attributed to the difference in exposure of the Gasport Formation between the two areas (Figure 3.10). In the southeast, the Gasport Formation is sub-cropping/outcropping, and in the northwest it is entirely overlain by one or more formations. Exposure of the Gasport Formation in the southeast means it has received a greater flux of recharge waters through geological time, thus promoting carbonate dissolution. In the northwest, infiltration to the Gasport Formation has been impeded by overlying formations (Goat Island FM, Eramosa FM), which have reduced recharge flux and the opportunity for permeability enhancement due to carbonate dissolution.

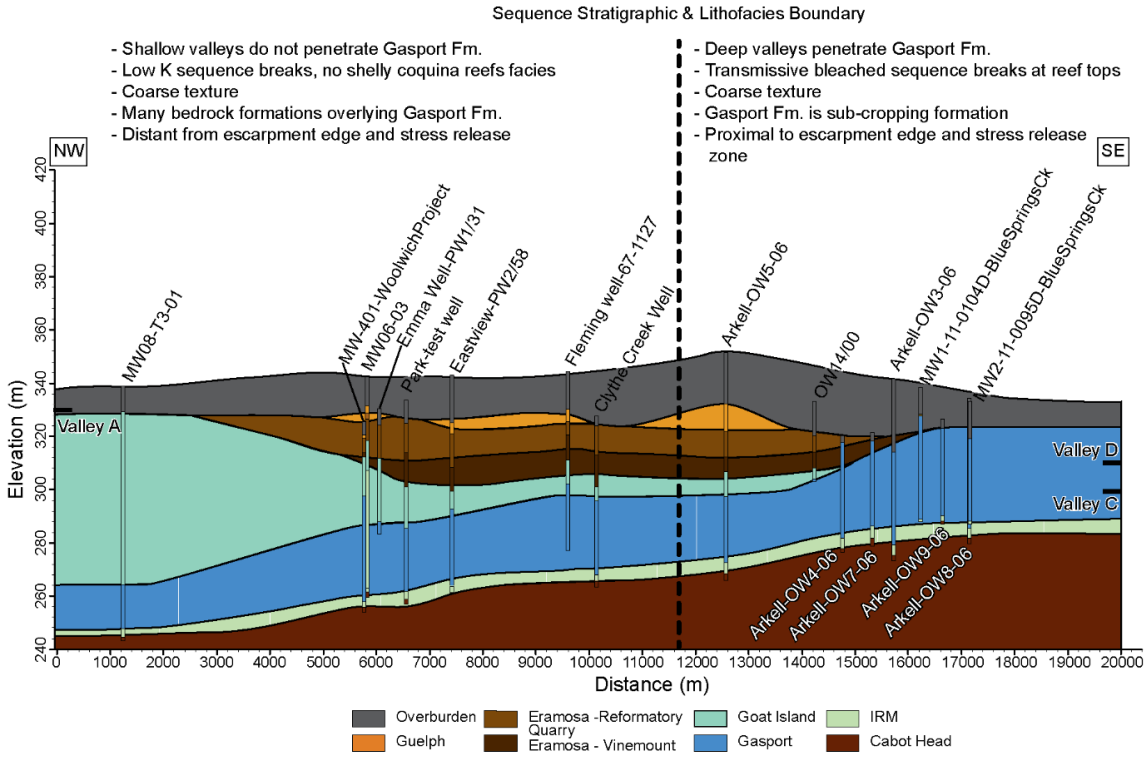

Figure 3.10. Cross-section A-A' through the centre of the study area (location of the section is shown on Figure 3.8). The dashed line towards the middle of the cross-section represents the lithofacies and sequence stratigraphic change within the Gasport Formation. The deepest elevations of incised buried valleys are shown on the cross-section margins. A comprehensive list of the differences in geological characteristics of the Gasport Formation between the northwest and southeast areas is presented at the top of the figure.

The Gasport Formation is very different in appearance between the northwest and southeast portions of the study area, and these differences also provide insight into the differences in *K* observed in Figure 3.9. Two sections of core from the Gasport Formation are shown in Figure 3.11, one from the southeast (well OW4-06, location on Figure 3.8), taken from 20 to 36 m below ground surface (bgs); and the other from the northwest (well MW08-T3-02, location on Figure 3.8), taken from 65.5 to 75 m bgs. The core from the southeast (Figure 3.11a) shows evidence of karstification throughout, which manifests as bleaching (whitish colouring) and rust staining, from iron precipitation, primarily at sequence stratigraphic breaks. The southeast core (Figure 3.11a) shows more breaks in general than the core from the northwest (Figure 3.11b), with some of these being purely mechanical, caused by the relatively closer proximity to the stress release zones along the edge of the Niagara Escarpment and nearby buried bedrock valleys. Based on the down-hole hydraulic testing of Brunton and Brintnell (2011) and Lee et al. (2011), not all discontinuities were determined to be as significant to groundwater flow as the karstic sequence stratigraphic breaks observed in this area. Vertical fractures or joints, which are more frequent in the southeast (Brunton 2009; Brunton and Brintnell 2011; Brunton et al. 2012) have likely served as

important conduits supporting karstification of the main horizontal flow zones occurring at sequence stratigraphic breaks in this area.

The core from the northwest (Figure 3.11b) has fewer breaks and is unoxidized and unweathered, which is manifested in its bluish hue, reflecting microbially-precipitated diagenetic pyrites in the rock matrix (Brunton et al. 2007). The smaller number of fractures observed in the northwest, compared to the southeast, has been attributed by Brunton et al. (2012) to be due its increased distance from the Niagara Escarpment and the bedrock valley edges.

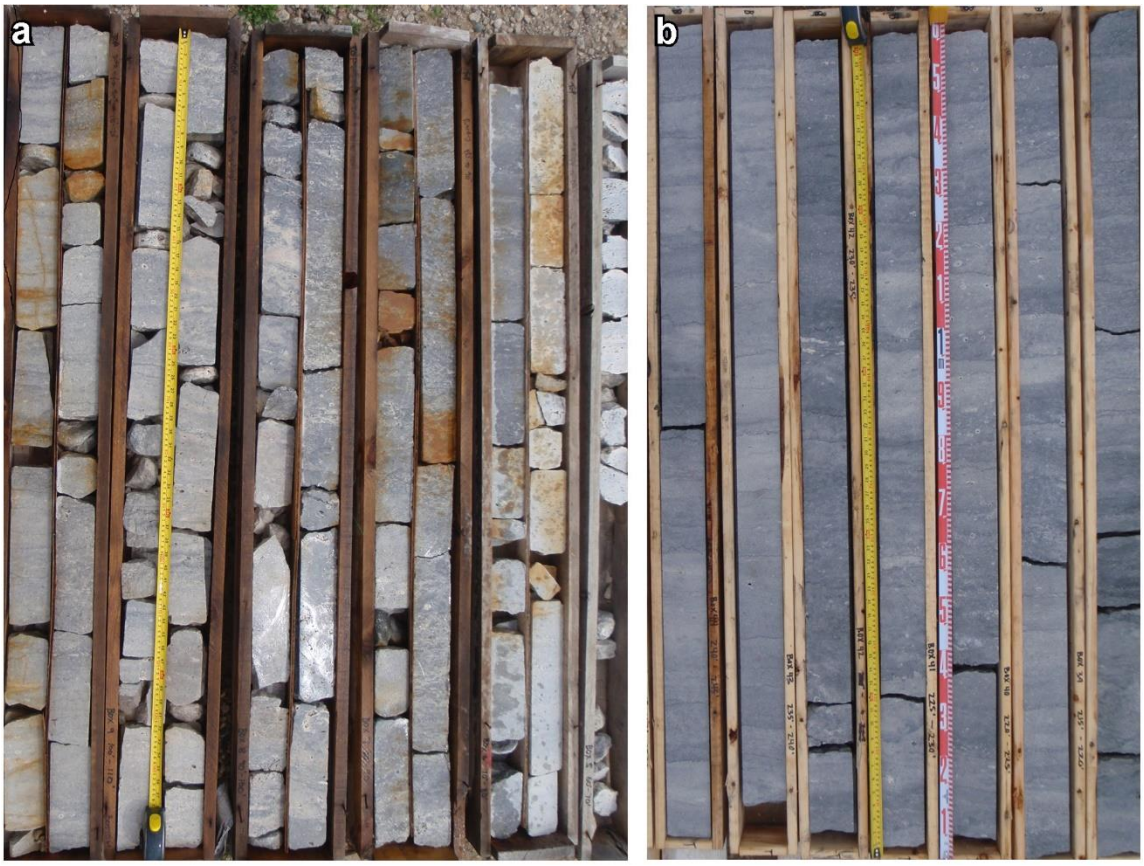

Figure 3.11. a A Gasport Formation core for the southeast area monitoring well OW4-06. The top right corner of **a** is 20 m below ground surface (bgs), descending back and forth along each section of core until the 37 m bgs level is reached at the bottom left corner of the photo**. b** A Gasport Formation core from the northwest area, taken from monitoring well MW08-T3-02, from 65.5 to 75 m bgs. The top right corner of **b** is 65.5 m bgs, descending back and forth until 75 m bgs at the bottom left corner of the photo. The locations of OW4-06 and MW08-T3-02 are shown on Figure 3.8.

Prior to infilling with glacial sediments, bedrock valleys provided conduits for meteoric and glacial water flux and loci for underdrainage of carbonate units through geologic time, promoting carbonate dissolution. The thalwegs for buried valleys C and D penetrate to the bottom and centre of the Gasport Formation, respectively, in the southeast portion of the study area (Figure 3.10, thalweg depths on SE

cross-section margin). Although proximity to buried valleys was not explicitly correlated with high *K*, it is still likely that they have influenced *K* by providing conduits for dissolution enhancement within coarse textured matrices or along sequence stratigraphic breaks in the southeast Gasport Formation. In contrast, bedrock valleys in the northwest only penetrate into the Guelph Formation and the underlying formations (Eramosa or Goat Island), and do not penetrate sufficiently deeply to cut through the Gasport Formation. As a result, the northwest valleys have not been conduits for recharge flux and dissolution enhancement in the Gasport Formation in this area, which is likely one of the reasons for the lower *K* trend observed for the Gasport Formation in the northwest.

The correlation between higher *K* and coarser textures that was described by others (Rovey and Cherkauer (1994 a,b) was not identified for the Gasport Formation. Because the Gasport Formation is consistently coarsely textured across the entire study area, the differences in the *K* distributions observed between the northwest and southeast cannot be attributed to texture. However, even though texture is not the dominant control on high *K* in the Gasport Formation, it is possible that dissolution enhancement in the consistently coarsely crystalline rock texture is a contributing factor to the high *K* trend.

The difference in *K* trends between the southeast and northwest Gasport Formation makes sense within the geological and geomorphological context of the study area. In the southeast, more frequent vertical jointing, as well as the deep bedrock valleys, have provided access points for recharge waters to enter the entire Gasport Formation and dissolve and enhance various conduits. These conduits comprise sequence stratigraphic breaks, and to a lesser extent, mechanical breaks and the rock matrix itself. In the northwest, the Gasport is overlain by several stratigraphic units that impede recharge flux. In addition, recharge flux is further impeded by the less frequent jointing and fracturing in the northwest, and the absence of bedrock valleys penetrating the Gasport Formation. And finally, the dissolution enhanced sequence stratigraphic breaks atop the shelly coquina facies are absent in the northwest.

3.6 SUMMARY AND CONCLUSIONS

The influence of bedrock valleys, carbonate rock textures and sequence stratigraphic breaks on *K* have been investigated independently and their combined influence has been evaluated conceptually for a single stratigraphic formation, within the geological and geomorphological context of the study area. The results of this investigation demonstrate that hydraulic conductivity is not controlled by one dominant geological feature, but rather by how the stratigraphic architecture varies in relation to where water has had access to the bedrock for dissolution-enhancement since deposition. The highest *K* values are associated with karstic sequence stratigraphic breaks in coarse textured bedrock where vertical conduits (joints and bedrock valleys) penetrate deeply and are most frequent. Consideration of both the inherent

characteristics of the bedrock as well as its location within a geomorphological context is essential to support predictions of where high *K* bedrock will be encountered.

There are many similar carbonate groundwater systems in basin settings where controls on *K* distributions can reasonably be expected to be the same as those observed here. In North America, examples include the Edwards-Trinity aquifers in the Edwards Plateau of Texas, USA (Ardis and Barker 1993), or the carbonate groundwater systems downdip of the Pembina Escarpment of the Williston Basin in Manitoba, Canada (Ford 1983; Grasby and Betcher 2002). Because the carbonate bedrock geology in these areas is similar to those of the present study area, the approach presented here should assist researchers in these areas to address some of the challenges of working in inherently complex, heterogeneous karst groundwater systems. Similar detailed integrative studies in these areas should lead to the identification of geological features associated with high K and how they change in space, as well as the development of maps that show areas where probability of encountering high K areas is greatest. Water managers must also consider that areas of high K do not always correlate with adequate storage for water supply and hydraulic testing is required. The intent here is to guide the selection of well targets. The integration of hydraulic testing results within a detailed geological framework has provided insight into the reasons why spatial variability of *K* is observed in certain areas and in particular geologic formations. This insight informs both groundwater exploration efforts and contaminant transport studies by predicting where, geographically and stratigraphically, high *K* bedrock will be encountered. Locally, the results of this study inform the city of Guelph of where the probability of encountering high K bedrock in the Gasport Formation is the greatest (*see* Figure 3.8).

The short-interval hydraulic test data used here were assembled from the privately owned data collection of the local municipality, the city of Guelph, which depends on groundwater for its water supplies. Local municipalities are storehouses of such information, and like the city of Guelph, they are likely willing to share with research partners where study objectives align. In addition to these high-quality data, a carefully vetted set of *K* values from domestic well specific capacity tests provided hydraulic information in areas of sparse coverage (Priebe et al. 2017b). The domestic well hydraulic data were obtained from a public database (Ontario 2015). Similar databases exist elsewhere and represent low cost data sources for investigating groundwater resources (e.g. State of California 2001; British Geological Survey 2017).

Chapter 4
Using Isotopic Tracers and Hydrochemistry to Map Recharge Areas and Groundwater Evolution in a Regional-Scale Carbonate Bedrock Groundwater System.

4.1 INTRODUCTION

The Early Silurian-age, Lockport Group carbonate bedrock hosts one of the most productive and best quality groundwater supplies in southern Ontario, Canada (Funk 1979; Sibul et al.1980; MacRitchie et al. 1994; Singer et al. 2003; Brunton et al. 2007; Sharpe et al. 2013). These carbonates are regionally extensive, relatively flat-lying and slightly dipping (Armstrong and Carter 2010), with potentiometric surfaces suggesting long, regional flow paths (Priebe and Brunton 2016). Despite these characteristics, which suggest an ease of understanding, these groundwater systems are complex, owing in part to the role that the glacial sediments play in controlling recharge distribution and the chemistry of recharging waters. In addition to the complexity presented by the glacial sediment cover, the Lockport Group carbonates contain karstic features throughout the study area, such as sequence stratigraphic breaks, fractures near scarps and valleys, and dissolution-enhanced coarse-textured facies (Brunton 2009; Priebe et al. 2018). Considering the geological and hydrogeological complexity of the carbonate groundwater system described by Priebe et al. (2018), it is reasonable to expect groundwater flow systems with varied flow-zone continuity and differing groundwater-residence times, which complicate assessments of hydrochemical evolution.

Many excellent analogs of hydrochemical evolution in carbonate groundwater systems exist worldwide (e.g., Plummer 1977; Edmunds and Walton 1983; Banner et al. 1989; Katz et al. 1995ab; Uliana et al. 2007; Li et al. 2010; Xie et al. 2013) and the major chemical processes in open and closed carbonate groundwater systems (Freeze and Cherry 1979) have been described for these analogs. The two most commonly used tools for characterizing water-rock interaction in carbonates are strontium isotopes ($^{87}Sr/^{86}Sr$) (e.g. Banner and Hanson 1990; Uliana et al. 2007; Li et al. 2010; Xie et al. 2013) and to a lesser extent, sulphur isotopes ($\delta^{34}S_{SO4}$ and $\delta^{18}O_{SO4}$) (e.g. Krothe and Libra 1983; Li et al. 2010; Jiminez-Madrid et al. 2017; Seibert et al. 2017). Strontium isotopes are excellent tracers in carbonate bedrock groundwater systems because the strontium isotope signature of the bedrock largely remains unchanged after deposition, with that signature controlled by the source of strontium (i.e., granitic terrains or

hydrothermal fluids) and also because they do not fractionate at the low temperatures of modern fresh groundwater systems. Unlike strontium isotopes, sulphur isotopes fractionate in modern fresh groundwater systems, and they do so in predictable ways that provides information about redox processes and relative groundwater residence times. The utility of strontium and sulphur isotopes for understanding water-rock interaction and geochemical evolution in groundwater has been well demonstrated for carbonate groundwater systems in non-glaciated settings (e.g. Krothe and Libra 1983; Banner and Hanson 1990; Uliana et al. 2007; Li et al. 2010; Xie et al. 2010; Jiminez-Madrid et al. 2017; Seibert et al. 2017). However, the utility of strontium and sulphur isotopes tools for characterizing carbonate bedrock groundwater systems that have glacial cover, where the geochemistry and properties of the glacial sediments may vary spatially, is not well studied, and is investigated here.

Although the Lockport Group carbonate bedrock is present across most of southwestern Ontario, it only contains significant and high-quality groundwater resources in the sub-crop and out-crop zone along the Niagara Escarpment (Brunton et al. 2007), which forms the boundary of this investigation (Figure 4.1). Many hydrogeological studies have been conducted at smaller scales, well-field to watershed, within the study area under a provincially regulated source water protection program (SWP) (Conservation Ontario 2017; Ontario 2017a). Study areas for SWP follow watershed boundaries and the suitability of these topographic boundaries for managing the bedrock groundwater resources, particularly for mapping recharge-areas, is assessed in this investigation. Perceived competition between the water-bottling industry and municipalities for the Lockport Group groundwater resources has recently prompted the Ontario provincial government to place a moratorium on issuing water bottling permits and has provoked an interest in improving regional bedrock groundwater characterization (Ontario 2017b). As local to global water quantity and allocation issues continue to mount, water managers are relying on scientific investigation, such as the present study, to support problem solving and policy development (SciVal 2011).

4.2 GEOLOGIC AND HYDROGEOLOGIC SETTING

The area under investigation is 8000 km^2 and is bounded in the north by the Bruce Peninsula and Lake Huron, to the east by the erosional edge of the Niagara Escarpment cuesta, to the south by the Algonquin Arch (Figure 4.1), which is the approximate Michigan basin boundary, and to the west by the sub-cropping of the younger strata of the Late Silurian, Salina Group evaporites (study area boundary in black, Figure 4.1). The western boundary marks a change in hydrostratigraphy as well as a deterioration of water quality associated evaporite deposits within the Lockport Group (Singer et al. 2003).

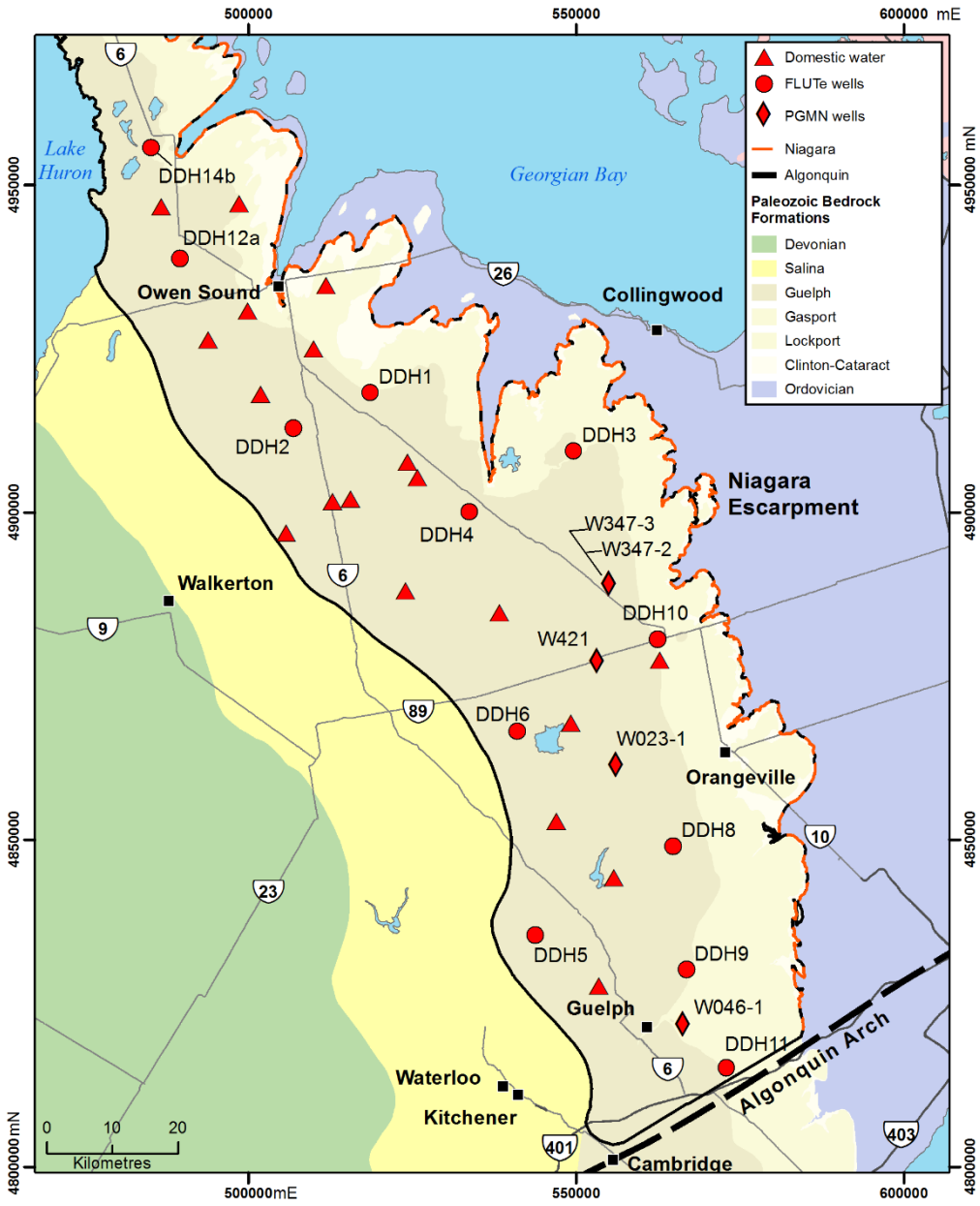

Figure 4.1. The study area is shown with groundwater sampling and water level measurement locations represented by *red symbols*, shown overlying the Paleozoic bedrock. Groundwater samples were collected from three different types of wells, with each type represented with a different *red* symbol. These well types consist of multi-depth monitoring wells (FLUTe construction), which contain between 3 and 6 sampling ports (*red circles*), Ontario Provincial Groundwater Monitoring Network of wells (PGMN, *red diamonds*) and domestic water supply wells (*red triangles*). The study area boundary is represented by the *black line*, with the Niagara Escarpment shown with a *dashed red line* in the east. Figure modified from Priebe and Brunton (2016).

4.2.2 Glacial History and Quaternary Geology

The last glacial maximum occurred during the Quaternary Period, approximately 20,000 years ago, when the Laurentide Ice Sheet covering most of Canada and the northern United States (Barnett 1992). The Catfish Creek Till was deposited during this time and is a key regional stratigraphic marker in southwestern Ontario (Bajc and Shirota 2007; Bajc and Dodge 2011), comprising a low permeability, over-consolidated, stony to stony sandy silt till that overlies older sediments or bedrock (Burt 2017). Lobation of the Laurentide Ice Sheet occurred with glacial retreat, resulting in three main ice lobes covering the study area; the Lake Simcoe lobe from the northeast, the Georgian Bay lobe from the northwest and the Ontario lobe from the south-southwest (Cowan et al. 1978). Each lobe incorporated different bedrock sources into the glacial sediment deposits, which has resulted in geographically varied recharge area sediment geochemistry (Barnett 1992). The main interlobate zone, representing the boundary of ice advance for each of the lobes, occurs roughly near a bedrock topographic high near the centre of the study area called the Dundalk Dome (Chapman and Putnam 1984, Figure 4.2). The advance and retreat of these three lobes, post-last glacial maximum, has resulted in the deposition of till unit/s overlying the Catfish Creek Till, the erosion of glacial sediments by meltwater, in many places down to bedrock, as well as the deposition of coarse-grained glaciofluvial and outwash deposits (Barnett 1992).

4.2.3 Bedrock Geology and Geochemistry

The Early Silurian, Lockport Group carbonates consist of the following stratigraphic formations in descending order; Guelph, Eramosa, Goat Island and Gasport (Figure 4.2). The Lockport Groups is underlain, in descending order, by the Irondequoit, Rockway and Merritton formations and the Cabot Head shale (Brunton 2009, Brunton and Brintnell 2011, Brunton et al. 2012). The Irondequoit, Rockway and Merritton formations are considered one unit for this investigation and referred to as the IRM (Figure 4.2). The Lockport Group of the study area is an approximately 100 m thick succession of stacked marine carbonates (Brunton 2009). Of particular interest to geochemical and isotopic interpretations for this study area the locations and types of sulphur and carbonate mineralogy that could potentially interact with groundwaters. The uppermost unit, the Guelph Formation, is a high-purity dolomite, containing very low silica levels, with localized sphalerite and galena mineralization (Brunton et al. 2007). The underlying Eramosa Formation is a uniformly crystalline dolomite that contains localized arsenic-bearing framboidal pyrites, as well as galena (Brunton et al. 2007), and is also described as petroliferous (Armstrong and Carter 2010). The Goat Island and Gasport formations are medium to coarsely crystalline dolomites that are reported to contain sulphate mineralization, as well as localized microcrystalline pyrites in the matrix of the coarser-textured lithofacies (Brunton et al. 2007). The study

area lies within the Michigan basin, and the Paleozoic bedrock formations dip gently toward the Michigan basin centre, southwest of the study area, at 3.5 to 12 m/km (Armstrong and Carter 2010).

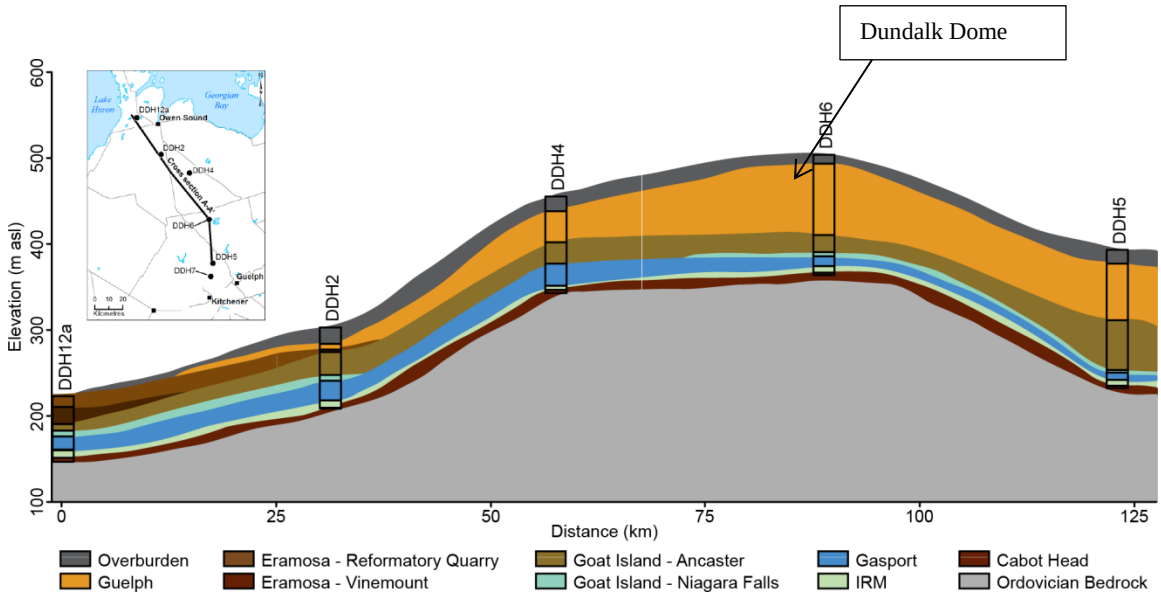

Figure 4.2. Approximately north to south cross-section through the study area. The Dundalk Dome is a bedrock and topographic high located roughly at the centre of the study area (modified from Priebe and Brunton 2016).

4.2.4 Hydrogeology

Groundwater in the Lockport Group carbonates has previously been described as flowing southwest, following the dip direction of the bedrock towards the Michigan basin centre (Sharpe et al. 2013). In their assessment, Sharpe et al. (2013) considered the Lockport Group carbonates as one hydrostratigraphic unit, with no differentiation of groundwater flow between individual stratigraphic formations. In their preliminary assessment, Priebe and Brunton (2016) describe groundwater flow in the Guelph Formation, as being radial, corresponding to the Dundalk Dome topographic high.

Regarding recharge areas, Sharpe et al. (2013) very broadly described recharge to the Lockport Group carbonates as occurring in areas of exposed bedrock, near the Niagara Escarpment edge. Additional, more detailed assessments of recharge areas at the watershed and sub-watershed scales were conducted across the study area to meet the requirements of the provincial Source Water Protection program (Clean Water Act, 2006, S.O. 2006, c. 22). Recharge areas in each watershed or sub-watershed were delineated based on the properties of the upper 3 metres of glacial sediments, and the recharge rates then estimated by calibrating a surface water flow model with continuous streamflow measurements, or by equating stream baseflow with total recharge (AquaResources 2009; Grey-Sauble Conservation Authority 2015). Recharge areas delineated for the Source Water Protection Program were made solely based on model

calibration results, with no field observations. Although these approaches ensure that the volume of recharge within a model domain is realistic, the absence of field observations of recharge through various soil and sediment brings uncertainty to recharge area mapping (AquaResources 2009).

4.3 METHODS

4.3.1 Groundwater Sampling and Hydrostratigraphic Unit Identification

Sixty-seven groundwater samples were collected from 35 sampling stations during July and August of 2016 (Figure 4.1). The stations consist of 12 multi-depth monitoring wells (FLUTe well construction), with 3 to 6 sampling ports at different depths, 5 Provincial Groundwater Monitoring Network (PGMN) wells and 19 domestic bedrock wells. Domestic bedrock wells were selected carefully, based on location, well type and quality, which were confirmed by reviewing the associated well records from the Ontario Ministry of Environment and Climate Change water well record database. Newer domestic wells (drilled in the past 10 years) and deep bedrock wells (more than 15 m into bedrock) were favoured. Water levels were collected from domestic wells and monitoring wells prior to sampling in June 2016, and monitoring wells were surveyed with a Trimble R8 TSC2, for top of well casing elevation.

Field parameters, consisting of pH, oxidation-reduction potential (later converted to Eh), electrical conductivity, dissolved oxygen and temperature, were monitored with a YSI 600XLM™ multi-parameter sonde in a flow-through cell prior to the collection of each sample, with sampling carried out once field parameters had stabilized. A field QA/QC program was undertaken to support an evaluation of analytical accuracy and precision. The QA/QC program consisted of the collection of 1 blank, 4 duplicate pairs and 6 standards, representing 15% of the total number of samples submitted for analysis. For redundancy, dissolved oxygen was measured with the YSI 600 XLM™ as well as analyzed using the Winkler titration method. Bicarbonate concentrations were calculated from alkalinity, which was measured in the field using the digital titration method of the HACH 16900-01 kit. Hydrogen sulfide was also measured in the field using the HACH model 2238-01 methylene-blue test kit. The test kit requires that a methylene blue spiked sample be matched to a colour spectrum, providing a 0.01 ppm detection limit. Groundwater samples were collected from domestic wells using dedicated electrical submersible pumps. Sample collection from monitoring wells was conducted with either dedicated submersible pumps, low flow displacement systems, or foot-valve pumps. Sample preservation and handling followed the Ontario Geological Survey groundwater sampling protocols as described by Hamilton (2015), which are consistent with those of the USGS (Wilde et al. 1998).

Hydrostratigraphic units (HSUs) within the Lockport Group were first defined at each of the 12 multi-depth monitoring wells (FLUTe well construction) by identifying the most transmissive units at these locations, based on borehole flow profiling and discrete hydraulic testing between packers (Lee et al. 2011). For the domestic and PGMN wells, where borehole flow and hydraulic testing were not available, HSUs were defined by identifying the stratigraphic position from which each well draws the majority of its water supply. This was done by projecting the "water found" field from the provincial water well record into the regional stratigraphic model of Brunton (2009). This approach was appropriate given the predictability of the Silurian bedrock, which is relatively flat-lying and devoid of folds or faults (Armstrong and Carter 2010). The "water found" position on the provincial water well record marks the depth where the water well driller encountered significant groundwater flow, usually signalling that an adequate domestic water supply has been encountered (Ontario 2015).

4.3.2 Analytical Methods

Groundwater samples were analyzed for major and minor inorganic parameters, stable water isotopes ($\delta^{18}O$ and $\delta^{2}H$), tritium, strontium isotopes ($^{87}Sr/^{86}Sr$) and sulphur isotopes ($\delta^{34}S$ and $\delta^{18}O$ of sulphate). General chemistry parameters and metals were analyzed at the Ontario Geological Survey, Geoscience Laboratories in Sudbury, Ontario by inductively-coupled plasma-mass spectrometer (ICP-MS), inductively-coupled plasma-atomic emission spectrometer (ICP-AES) and ion chromatography (IC).

Stable water isotope analyses, $\delta^{18}O$ and $\delta^{2}H$, were conducted by Isotope Tracer Technologies Inc. in Waterloo, Ontario. These analyses were conducted by cavity ring down spectroscopy on a Picarro Model L1102-I with an analytical precision of +/- 0.1 per mil for oxygen and +/- 0.6 per mil for hydrogen. For quality assurance, a cross-laboratory comparison was conducted by sending a sub-set of samples to a second lab for $\delta^{18}O$ and $\delta^{2}H$ analyses. Tritium analyses were conducted at the University of Waterloo, Canada, Environmental Isotope Laboratory by liquid scintillation counting. The samples were enriched 15 times by electrolysis, following the method of Taylor (1977), and counted to achieve a detection limit of 0.8 TU.

Strontium isotope ($^{87}Sr/^{86}Sr$) analyses were conducted on a Thermo Finnigan Triton thermal ionization mass spectrometer, using the double rhenium filament technique. These analyses were done at the Environmental Isotope Laboratory, University of Waterloo, Ontario. Strontium was first extracted from the sample with an ion specific resin, following a similar approach to that of Horowitz and Gale (1994) for lead. The standard reference material NIST 987 was inserted 3/21 times for QC, and a standard error of precision of $\alpha = 0.00002$ was achieved. Rock samples, taken from bedrock core powders, were also analyzed for strontium isotopes for comparison with groundwater values. Like the water analyses, these

were conducted on a Thermo Finnigan Triton thermal ionization mass spectrometer, with the analyses performed on digested solids at the University of Saskatchewan Isotope Laboratory, Saskatoon, Canada.

Sulphur isotopes analyses, comprising $\delta^{34}S$ of sulphate and sulphide as well as $\delta^{18}O$ of sulphate, were performed at the G.G. Hatch stable isotope laboratory at the University Ottawa, Ontario. Where sulphide was detected in the groundwater sample in the field, the sample was preserved and the sulphide precipitated with a Zn acetate solution. Although samples were collected for $\delta^{34}S$ of sulphides, the sulphide concentrations were too low to be successfully analyzed. Sulphur isotope analyses were conducted using a Thermo Finnigan DeltaPlus XP ion spectrometer, with a Conflow IV for analysis, following the method of Grassineau et al. (2001), achieving an analytical precision of +/- 0.3 ‰ VCDT.

4.4 RESULTS AND DISCUSSION

The results of the chemical and isotopic analyses are presented to evaluate basic hydrochemical trends by geologic formations, identify the locations of regional-scale recharge areas and to investigate groundwater chemical evolution in the bedrock flow systems. Groundwater chemistry results presented in the section are shown without error bars, as is the common approach for such geochemical data because of the small detection limits. Detection limits for chemical and isotopic parameters are presented in Priebe and Lee (2016)

4.4.1 Groundwater Flow Direction by Hydrostratigraphic Unit

As described in section 4.3.1, regional hydrostratigraphic units were defined by identifying the stratigraphic position of the most transmissive bedrock formations at each well location, and extrapolating these findings across study area using the geological model of Brunton (2009). The Guelph and Goat Island formations were identified in this investigation as the most significant hydrostratigraphic units (HSU) of the study area. Inferred groundwater flow in the Guelph Fm HSU is radial, away from the Dundalk Dome, with the flow divide centred around DDH6 and DDH10 (Figure 4.3A). On the flanks of the Dundalk Dome, the Guelph Formation thins and eventually pinches out to the north, east and south, with its extent approximated in plan view on figure 4.3A. Calculated vertical gradients within the Guelph Formation, measured in the Dundalk Dome area, are weakly downward ranging from 0.003 (DDH6) to 0.07 (DDH10). Similarly weak gradients are calculated for horizontal groundwater flowing south-southwest and north-northwest of the Dundalk Dome are 0.003 and 0.004, respectively (Figure 4.3A). The possible range of groundwater velocities for the Guelph FM HSU is between 100 m/year and 4 km/year, as estimated from Guelph FM K values ($3x10^{-4}$ to $2x10^{-7}$ m/s, Priebe et al. 2017), the range of

local porosities (0.1-24 % , Zheng 1999) and the horizontal gradient for the Guelph FM hydrostratigraphic unit (0.004).

The Goat Island Formation has a uniform thickness of approximately 40 m across the study area, and it underlies the Guelph Formation in the centre of the study area and the Eramosa Formation at the northern and southern study area margins. Downward vertical gradients were calculated and mapped by taking the difference between the elevations of the piezometric surfaces for the Guelph Fm (Figure 4.3A) and Goat Island Fm (Figure 4.3B) HSUs. The geographic distribution of downward vertical hydraulic gradients between the Guelph and Goat Island Formations is shown in Figure 4.3C, represented with the blue hatched polygons. Much like the Guelph Fm HSU, the inferred groundwater flow direction for the Goat Island HSU is radial from the Dundalk Dome area, and the calculated horizontal gradients are weak, approximately 0.003 in all directions from the Dundalk Dome flow divide (Figure 4.3b). The possible range of groundwater velocities for the Goat Island FM HSU is between 80 m/year and 9.5 km/year, as estimated from Guelph FM K values ($1x10^{-4}$ to $2x10^{-7}$ m/s, Priebe et al. 2017), the range of local porosities (0.1-24 % , Zheng 1999) and the horizontal gradient for the Guelph FM hydrostratigraphic unit (0.003).

The study area contains portions of six watersheds. The boundaries of these watersheds are shaped by the geometry of the surficial landforms, and they do not appear to perfectly align with the bedrock groundwater flow divide observed near the Dundalk Dome (Figure 4.3D). Instead, the bedrock groundwater systems appear to reflect the bedrock topography, consisting of what appear to be longer, regional-scale bedrock groundwater flowpaths that cross several watershed boundaries.

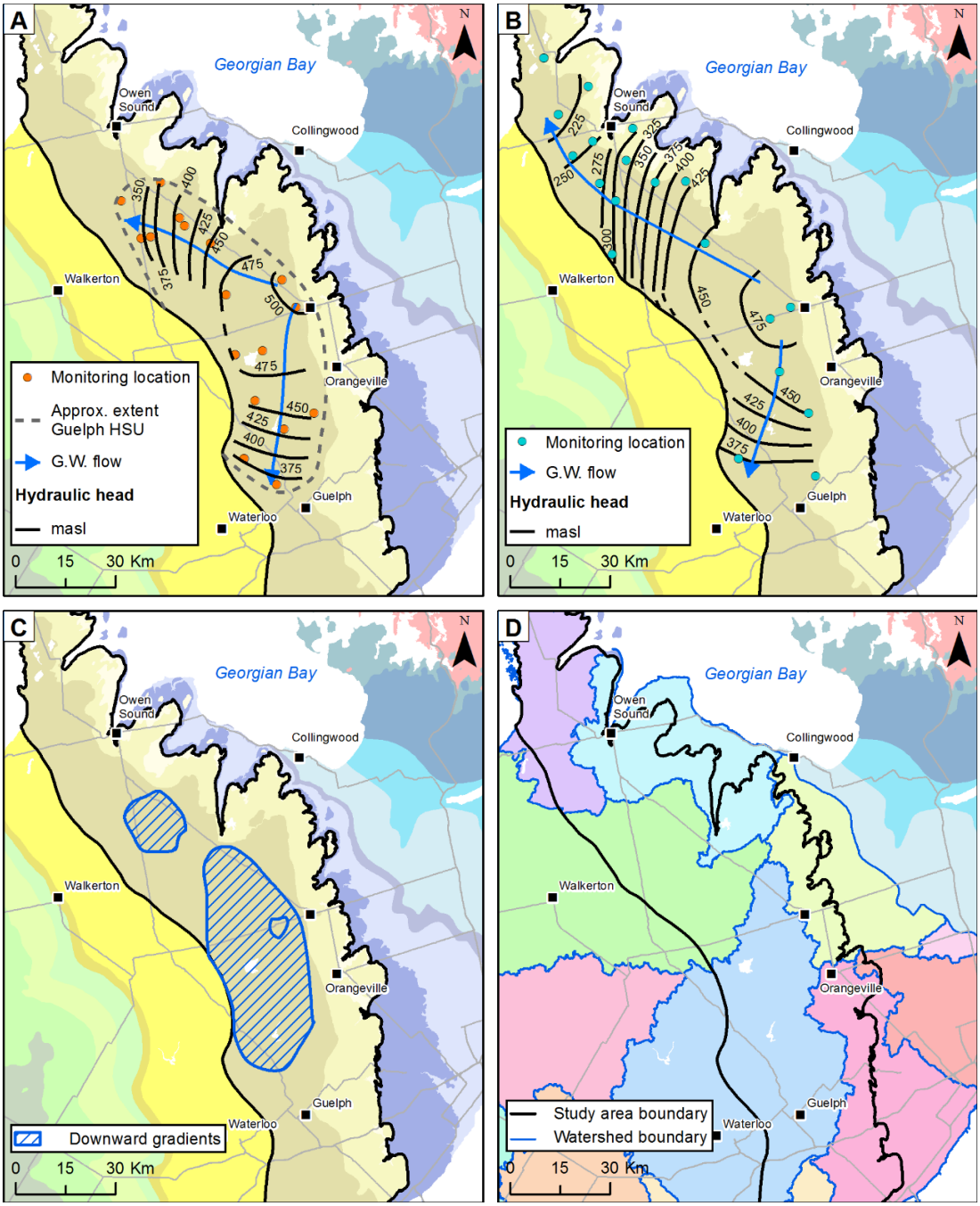

Figure 4.3. Piezometric surfaces are presented for the bedrock formations that are the most significant groundwater producers, the Guelph Fm Hydrostratigraphic Unit (HSU) (Panel A) and the Goat Island Fm HSU (Panel B). The locations of the wells from which water level measurements were taken are shown, with the Guelph Formation wells symbolized with *orange circles* (Panel A) and the Goat Island Formation wells symbolized with *turquoise circles* (Panel B). Groundwater flow directions for both HSUs are shown with *black arrows*. Areas where there are downward gradients between the Guelph and Goat Island formation HSUs are shown in Panel C, represented by hatched polygons. Panels A through C are shown overlying the Paleozoic bedrock. The watershed boundaries of the study area, and beyond, are presented in Panel D.

4.4.2 General Chemistry

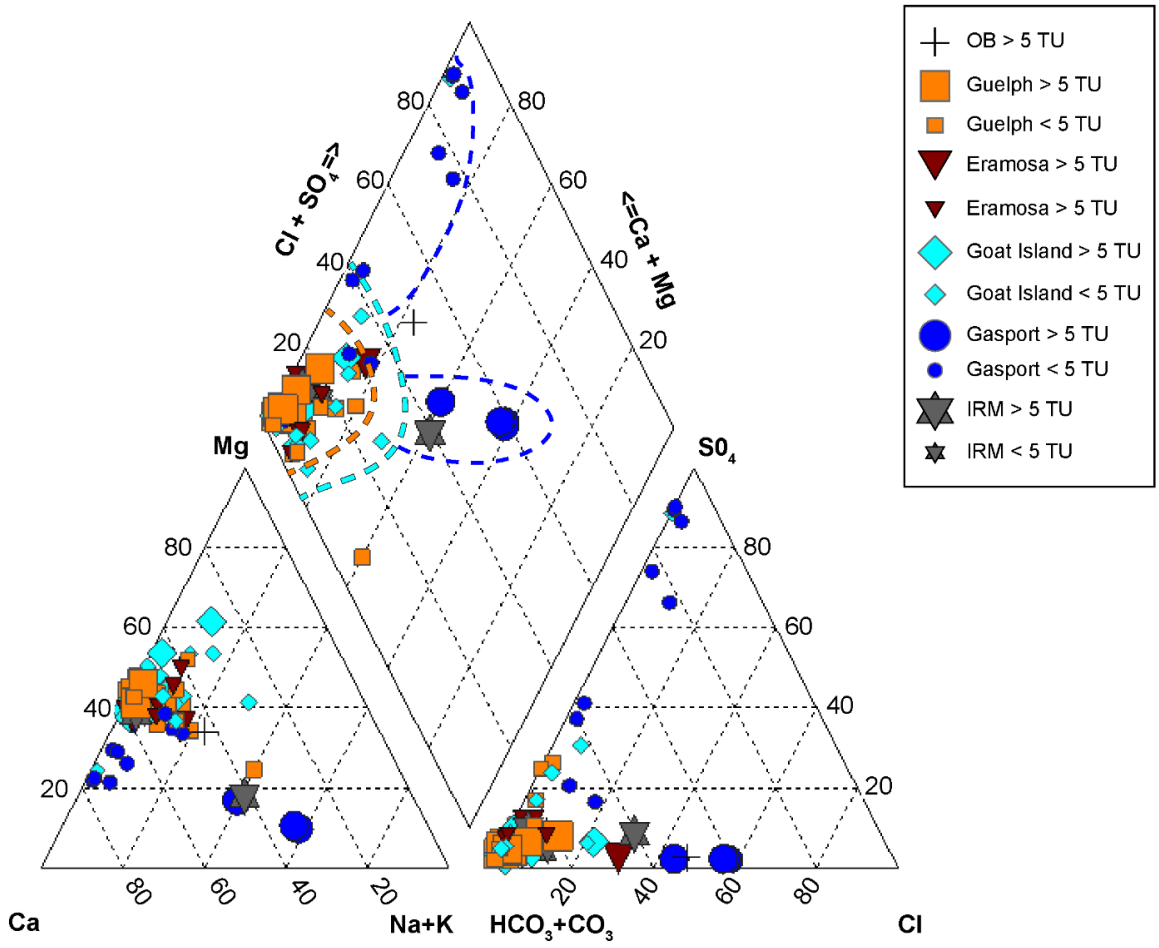

Figure 4.4. A Piper diagram plotting groundwater data for samples collected from each of the Lockport Group bedrock formations. Groundwater samples from each bedrock formation are represented by a symbol with a unique *shape* and *colour*. The *symbol size* reflects the tritium content, with samples containing greater than 5 tritium units represented with *large symbols* and samples containing < 5TU represented with *small symbols*. The legend presents the symbols for each geologic formation in descending stratigraphic order. The IRM refers to a grouping of three formations that underlie the Lockport Group: the Irondequoit, the Rockway and the Merritton.

A Piper diagram (Figure 4.4) displays major ion trends for each geologic formation and the symbol size reflects the tritium content of the sample, with small symbols representing very low to non-detect tritium and larger symbols representing tritium values > 5 TU. The very low to non-detect tritium levels roughly reflect "older" water, with recharge timing prior to the 1950's atmospheric nuclear testing (Brown 1961). Samples with > 5 TU roughly reflect more recent recharge. With the exception of one outlier, the Guelph Formation has the least mineralized signature with a consistent Ca-Mg-HCO_3 water type (within orange dashed line, Figure 4.4). Groundwater becomes more mineralized in the Goat Island Formation (turquoise dashed line, Figure 4.4), which underlies the Guelph Formation. Too few samples are available for the Eramosa Formation, which underlies the Goat Island, to asses a trend. Groundwater in the deepest

Lockport Group formation, the Gasport (dark blue dashed lines, Figure 4.4), shows a relative increase in proportions of sodium, chloride and sulphate as groundwater trends move away from the Ca-Mg-HCO_3 area on the Piper diagram with increasing stratigraphic depth. The two trends observed for the Gasport Formation, a high sulphate trend and a high chloride trend, occur in different geographic locations within the study area. The high sulphate trend, with low associated tritium content, is observed in the southern part of the study area. The high chloride trend, with higher associated tritium content, is observed in the northern part of the study area. This high chloride trend is limited to a single multi-depth well (DDH3, Figure 4.1) located in a Gasport Formation sub-crop area, near a roadway. Chloride to bromide ratios, which are commonly used to distinguish between different chloride sources, are as high as 8000 for the DDH3 samples, falling within a range indicative of road salt influence (Katz et al. 2011).

A general trend of more mineralized groundwater with increasing stratigraphic depth is observed, and this trend appears to be independent of tritium content (Figure 4.4). Each stratigraphic formation has samples that contain very low to non-detect tritium, as well as samples with higher tritium content. Longer groundwater residence times are often associated with increased mineralization. However, the absence of a correlation between tritium values and mineralization in this study area suggests that residence times are not necessarily longer in the deeper stratigraphic units, but rather that there is a range of recharge timing for each stratigraphic formation that is independent of stratigraphic position.

4.4.3 Preliminary Assessment of Relative Recharge Timing

Tritium content in bedrock groundwater was interpolated across the study area as a means of conducting a reconnaissance-level assessment of relative recharge timing (Figure 4.5A). The tritium values used in this assessment comprise the bedrock groundwater samples from this investigation, as well as a sub-set of bedrock groundwater tritium data from Hamilton (2015) that were used to enhance the spatial density of the dataset. The sampling locations for the combined dataset are shown on Figure 4.5A. The tritium data from Hamilton (2015) comprise samples collected from bedrock domestic wells. The interpolation of tritium data was developed using the nearest neighbour method of Sibson (1981) (Figure 4.5A). This interpolation includes tritium data from all bedrock formations. This reconnaissance-level assessment provides a foundation for recharge area mapping conducted for each hydrostratigraphic unit, described in detail in section 4.5, below. In this assessment, low tritium levels in bedrock groundwater are assumed to represent areas of relatively insignificant recharge flux in comparison with the areas of high tritium in bedrock groundwater. However, the possibility remains that areas of low tritium in bedrock may represent important recharge areas to some parts of the groundwater system, with long residence times in the overburden having resulted in tritium decay upon entry into the bedrock. Mixing and dispersion, the

quantification of which was being the scope of this assessment, have also likely influenced tritium content in bedrock groundwater. Given these uncertainties, recharge areas as described here using tritium levels, among other parameters, should be considered to be "significant", as they carry the strongest evidence of high flux of fresh meteoric waters into bedrock, but not exclusive.

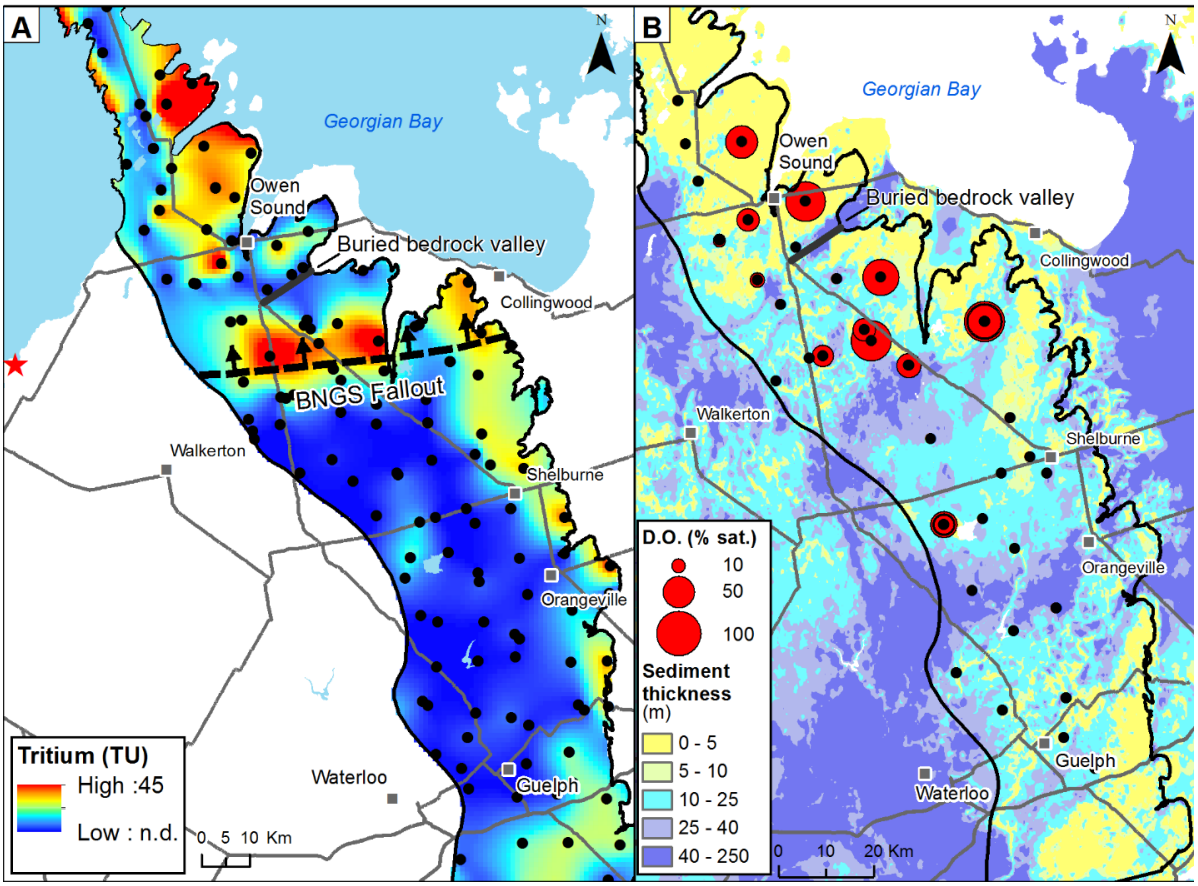

Figure 4.5. Tritium content (as tritium units) is presented in Panel A and dissolved oxygen (as % saturation) values are presented in Panel B for study area *bedrock* groundwater. Groundwater sampling points are represented on both panels with *black circles*. In Panel A, the location of the Bruce Nuclear Generating Station (BNGS) is shown with a *red star*, and the extent of influence of BGNS on tritium is represented with a *dashed black line*. The dissolved oxygen data in Panel B are symbolized with gradational red circles, where the larger the symbol the greater the percent saturation of dissolved oxygen. The sampling points where dissolved oxygen was not detected in bedrock groundwater are symbolized with *black circles*. In Panel B, the dissolved oxygen values are plotted on the glacial sediment thickness of Gao et al. (2007).

The tritium values observed in bedrock groundwater range from below method detection (0.8 TU) to 44 TU. The highest values are from samples collected in the northern third of the study area, which is the portion of the study area that is just east of, and downwind, of the Bruce Nuclear Generating Station (BNGS), which began operations in 1976 (Figure 4.5A). The location of BNGS is shown on Figure 4.5A with a *red star*. The annual average tritium value in precipitation at the BNGS was 1142 TU in 2016, and ranged from 635 TU to 2542 TU in the past decade (Bruce Power 2017). The tritum values near the

BNGS are significantly higher than the weighted annual average tritium content of precipitation in southern Ontario, which is 17 TU (IAEA 2015 https://nucleus.iaea.org/Pages/GNIPR.aspx). Weighted annual average tritium levels in precipitation have been stable in southern Ontario since the 1990's (Clark and Fritz 1997), with the exception of local influences from nuclear generating stations. The interpolation presented in Figure 4.5A does not account for tritium in precipitation originating from BNGS, and this must be considered in the interpretation of this figure. In the northern third of the study area, which is the area north of the *black dashed line* on Figure 4.5A, the most recent recharge has a signature of approximately 40 TU and is represented with red hues of the colour ramp. South of the influence of the BGNS, depicted with the *dashed black line* on Figure 4.5A, recent recharge carries the weighted annual average tritium level of 17 TU, and these areas are identified with orange to turquoise. Based on decay calculations, using the average tritium values for southern Ontario precipitation, groundwater recharged prior to the release of bomb tritium in the 1950's would have a present day tritium signature of < 0.8 TU in. Areas of this sub-modern (pre-1950's) recharge are represented on Figure 4.5A as dark blue.

Dissolved oxygen in bedrock groundwater is shown on Figure 4.5B, superimposed onto the glacial sediment thickness map of Gao et al. (2007), to evaluate the influence of sediment thickness on the distribution of regional-scale recharge areas. Dissolved oxygen in groundwater provides hydrochemical evidence of rapid recharge because of its atmospheric origin and rapid reactivity in the sub-surface. The dissolved oxygen values in Figure 4.5B are presented as gradational dots, reflecting percent saturations. At the typical temperature and elevation of the study area, 100% saturation would equal approximately 10 mg/L of dissolved oxygen. Measureable dissolved oxygen (DO) penetrates to great depths in bedrock (~100m) at many locations in the northern third of the of the study area, and also at one location in the Dundalk Dome area.

Where overburden sediments are thin or absent, DO is high and tritium values more closely resemble precipitation averages, suggesting more recent recharge. These areas generally occur in the north, near the Niagara Escarpment edge and in the Dundalk Dome area. In contrast, DO is absent and tritium values indicate sub-modern recharge timing in groundwater for areas where the carbonate bedrock is overlain by thick glacial sediments. One such area of thick glacial sediments (>250m) represents a buried bedrock valley, as described by Eyles et al. (1993) (Figure 4.5B). When considered together, the tritium content, DO and the thickness of glacial sediments provide corroborating evidence of regional trends of recharge to the bedrock groundwater systems. The locations where DO is measured in bedrock groundwater tend to fall within the areas where the tritium trends indicate more recent recharge, and likewise, there is no measureable DO in areas where the tritium content suggests sub-modern recharge.

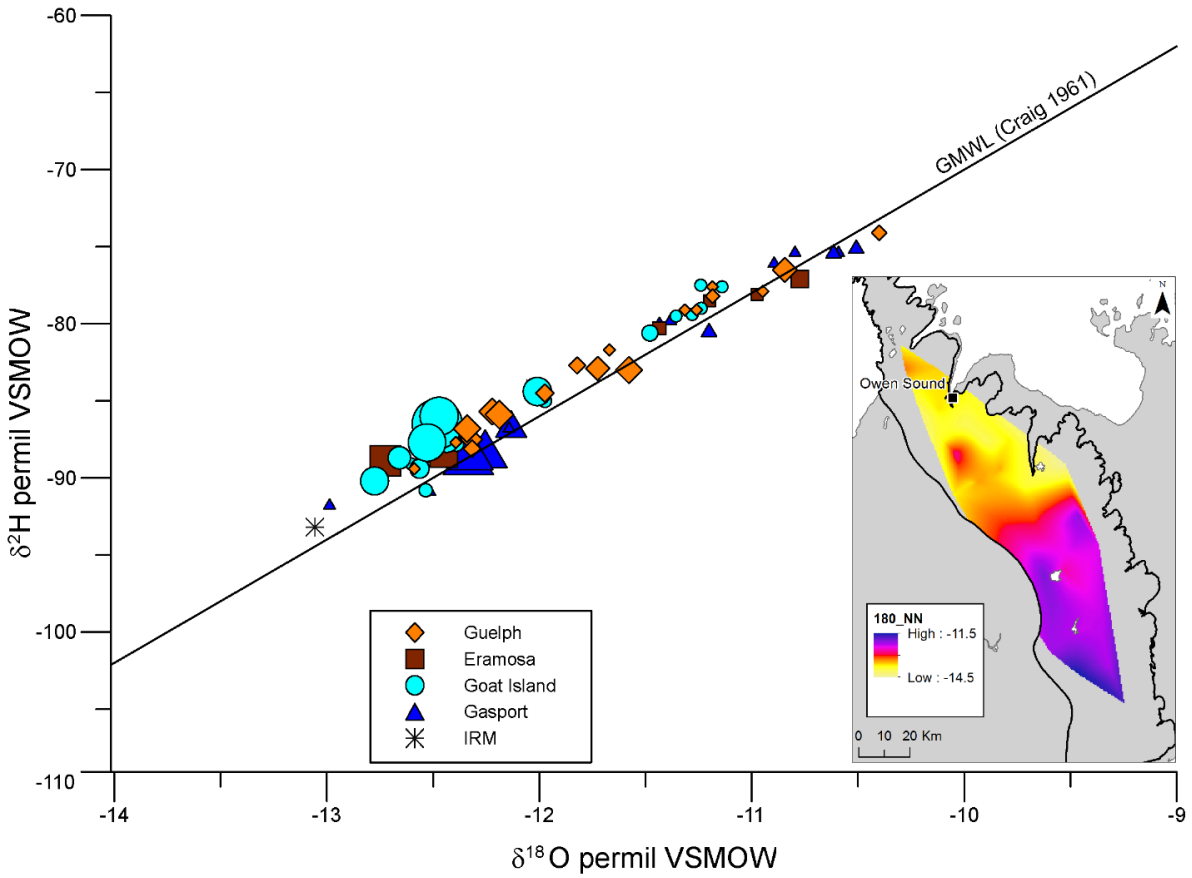

Figure 4.6. Deuterium (δ^2H) and $\delta^{18}O$ values for bedrock groundwater samples are displayed with the Global Meteoric Water Line (GMWL) of Craig (1961). Groundwater samples are represented with symbols that have a *shape and colour* that are unique to each bedrock formation. The *size* of the symbol reflects the tritium content of the sample, with the highest tritium contents represented with largest symbols. The inset map contains an interpolation of $\delta^{18}O$ in bedrock groundwater, generated value from the Guelph and Goat Island hydrostratigraphic units.

As shown in Figure 4.5A, tritium content in groundwater at many locations is below detection limit (0.8 TU), indicating sub-modern recharge timing, prior to the nuclear-bomb testing of the early 1950's (Clark and Fritz 1997). To further assess the recharge timing of these pre-1950's samples, groundwater samples were analyzed for stable water isotopes δ^2H and $\delta^{18}O$, looking particularly for evidence of isotopic depletion caused by glacial, cold climates at the time of recharge. Stable water isotopes are presented in Figure 4.6, with symbols coded and sized to represent geologic formation and tritium content, respectively, with the larger symbols representing greater tritium content. The δ^2H and $\delta^{18}O$ values generally fall on the global meteoric water line of Craig (1961), with a slight deuterium excess. This deuterium excess can be attributed to lake effect evaporation, as described by Gat et al. (1994), over Lake Huron which is located up-wind of the study area.

The $\delta^{2}H$ and $\delta^{18}O$ values for bedrock groundwater fall within the range reported for modern groundwater in southern Ontario (Fritz et al. 1987). The isotopic signature presented in Figure 4.6 is not depleted enough to suggest evidence of Pleistocene-age recharge, though such old waters have been identified in nearby deep glacial sediment aquifers (Aravena and Wassenaar 1993). The only trend observed in the water isotopes of this investigation is a latitude influence, with the northernmost sampling locations having the most depleted $\delta^{18}O$ values, and the southern values being more enriched. This trend can be observed with the interpolation of $\delta^{18}O$ values (inset map, Figure 4.6), which shows a marked depletion in $\delta^{18}O$ from south to north and a sharp change in the $\delta^{18}O$ signature near the centre of the study area, in the vicinity of the Dundalk Dome.

4.4.4 Water-Rock Interaction

A water-rock interaction investigation was undertaken to identify the main geochemical process occurring along the groundwater flow paths and to support the characterization of recharge and evolved chemical end-members. This investigation relied on strontium isotopes in bedrock and groundwater, and sulphur isotopes in the groundwater system.

4.4.4.1 Strontium Isotopes

The Sr isotopic signature ($^{87}Sr/^{86}Sr$) of each bedrock formation is presented in Figure 4.7A, with all bedrock samples symbolized with yellow diamonds. The data show a clear trend of bedrock formations having a more radiogenic $^{87}Sr/^{86}Sr$ signature with geologic age and stratigraphic depth. The $^{87}Sr/^{86}Sr$ values of the groundwater samples for each geologic formation are shown underlying the associated bedrock values for the same formation, where the groundwater symbols are sized to reflect the tritium content in the sample (Figure 4.7A). When comparing bedrock and groundwater strontium isotope values, in some cases there is an obvious difference between signatures. The greatest disparity between bedrock and groundwater signatures is observed for the Guelph Formation, with a bedrock range of values from 0.7082 to 0.7086 and a groundwater range of values 0.7084 to 0.7104 (Figure 4.7A).

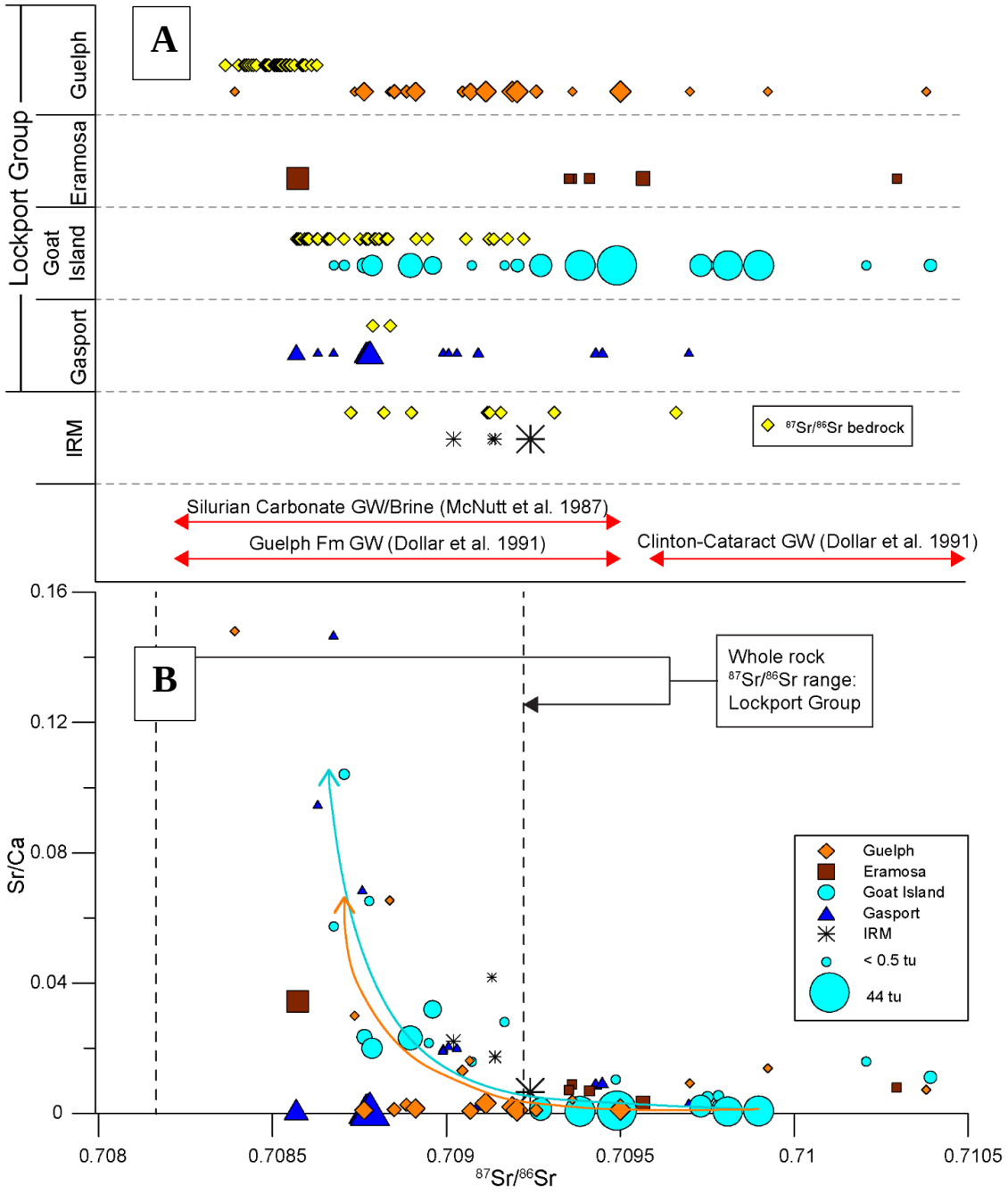

Figure 4.7. Strontium isotope ratios ($^{87}Sr/^{86}Sr$) for groundwater and bedrock are shown in *Panel A*, with the x-axis shown at the bottom of Panel B. In Panel A, the strontium isotope ratios measured in bedrock are symbolized with yellow diamonds, and these are shown by formation in descending stratigraphic order. The IRM combines the data for three formations, the Irondequoit, the Rockway and the Merritton. The strontium isotope ratios for groundwater samples are shown directly under the bedrock values, with shape and size of groundwater samples reflecting formation and tritium content. For comparison, $^{87}Sr/^{86}Sr$ ranges from the literature for groundwater and brines are shown with red arrows. In *Panel B*, the strontium isotope ratios are plotted against the Sr/Ca ratio. For Panel B, the $^{87}Sr/^{86}Sr$ range for the Lockport Group bedrock is shown with dashed vertical lines.

The Sr/Ca ratios in groundwater were plotted to provide insight into mineral precipitation following dolomite dissolution, and how these interactions might change with groundwater residence time. In

carbonate bedrock groundwater systems, the Sr/Ca ratio can provide valuable information about mineral precipitation/dissolution and the incongruent dissolution of related minerals (Edmunds and Walton 1983). In Figure 4.7B, the Sr/Ca ratios are plotted against the Sr isotope ratio for groundwater samples, with the Sr isotope ratio range for the bedrock formations shown with vertical dashed lines to facilitate a comparison between groundwater and the host-rock signature (Figure 4.7B). The groundwater samples that fall within the vertical dashed lines of the host bedrock Sr isotope signature also happen to have the highest Sr/Ca ratio. These high Sr/Ca ratio groundwater samples also have little or no detectable tritium content, indicating that these waters have resided in the groundwater system since the 1950s, or earlier.

The difference between the more recently recharged groundwater (large symbols) and the bedrock Sr isotope signatures is likely due, at least in part, to the potential Sr inputs from the mineralogy of the overlying glacial sediments, which constitute the surficial materials of the recharge pathway. The Clinton-Cataract Group underlies the Lockport Group bedrock formations, but also sub-crops or out-crops along the entire edge of the Niagara Escarpment in the study area. Ice flow during the most recent glaciation comprised a Georgian Bay/Huron lobe, descending from north to south, a Simcoe lobe, approaching from the northeast, and a lake Ontario lobe migrating from the south (Cowell et al. 1978). These glacial ice lobes eroded the bedrock surface, depositing glacial sediments that contained up-ice bedrock components such as the rocks of the Clinton-Cataract Group. A Sr isotopic range for Clinton-Cataract Group formational brines, collected from deeper within the Michigan Basin in Ontario by Dollar et al. (1991), is shown for comparison (Figure 4.7A). This range is more radiogenic than the Lockport Group bedrock range observed here. Therefore, the groundwater samples that carry a more radiogenic signature than their host bedrock formation are likely carrying the signature of the Clinton-Cataract, imprinted as water was recharging through the glacial sediments.

The increase in Sr/Ca ratio and the evolution toward a Lockport Group, host-rock Sr isotope signature in groundwater (Figure 4.7B), appears to occur with increasing groundwater residence time. This is likely due to incongruent dissolution of the dolomite host rock, which could lead to calcite precipitation and thus influence the Sr/Ca along the flowpath. Because dolomite dissolution is irreversible at the low temperatures found in most modern groundwater systems (Drever 1988), other carbonate minerals precipitate as groundwater evolves away from recharge areas. Calcite reaches equilibrium sooner than strontium minerals because of the proportional abundance of Ca compared with Sr. The removal of Ca from solution as calcite precipitates causes a Sr/Ca ratio increase. The Sr that dissolves along the flowpath carries the Sr isotopic signature of the host bedrock, resulting in the groundwater signature eventually matching the host-rock Sr isotope signature. The dissolution of dolomite and subsequent precipitation of carbonate minerals is also supported by the pH data shown in Table 4.1a, as pH values are

shown to be lowest at recharge, increasing with chemical evolution. An increase of the Sr/Ca with groundwater evolution was similarly observed for the Lincolnshire Limestone aquifer by Edmunds and Walton (1983), who also attributed the trend to incongruent dissolution of dolomite.

4.4.4.2 SULPHUR ISOTOPES

The sulphur isotopic composition of sulphate, $\delta^{34}S_{SO4}$ and $\delta^{18}O_{SO4}$, in bedrock groundwater covers a broad range that encompasses the depleted compositions typical of pyrite oxidation, (Claypool et al. 1980) to the enriched composition of Silurian-age evaporites (Toran and Harris 1989). Sulphur isotope values for groundwater are presented in Figure 4.8A, with the data encircled to show three groupings of distinct sulphur isotopic compositions. These three groupings consist of a pyrite oxidation composition (Group 1), a Silurian evaporite composition (Group 3) and a mixed composition that falls between these (Group 2) (Figure 4.8A).

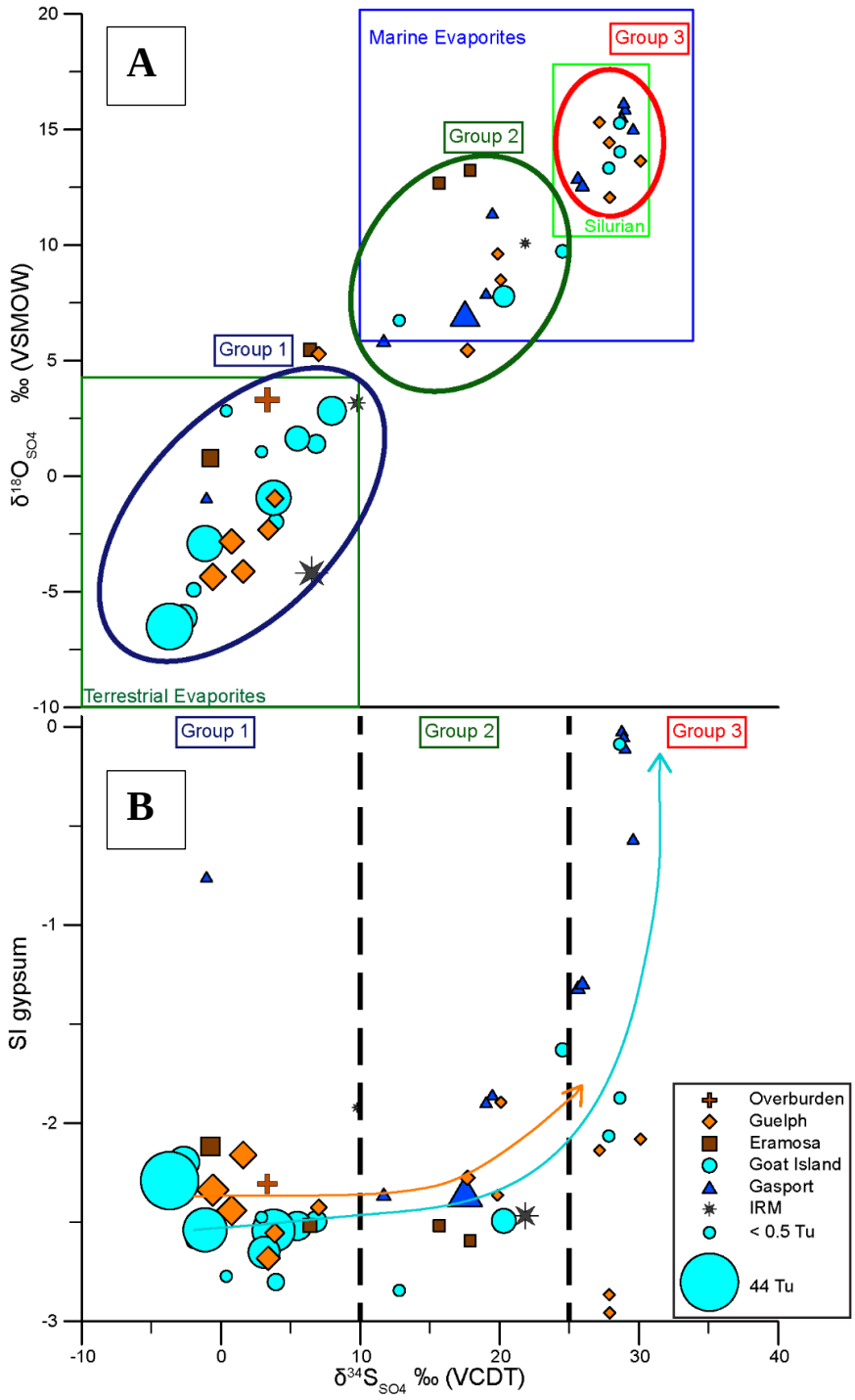

Figure 4.8. *Panel A* presents the $\delta^{34}S$-$\delta^{18}O$ composition of groundwater. The symbol for each groundwater sample represents the associated bedrock formation by *symbol colour* and *shape*. The tritium content of the sample is expressed in the *symbol size*, with the greatest tritium content represented by the largest symbol. The isotopic composition of terrestrial sulphate (Claypool et al. 1980), marine evaporites (Toran and Harris 1989), and the Silurian evaporites (Toran and Harris 1989) are shown for context. In P*anel B*, the $\delta^{34}S$ composition of sulphate in groundwater is presented versus the saturation index for gypsum.

Group 1: Pyrite Oxidation (Terrestrial Evaporite) Composition

Group 1 samples have a depleted sulphur isotopic signature and the highest tritium values of the entire dataset, with many containing measureable quantities of DO, indicating that they represent the most recently recharged waters. The Group 1 sulphur isotopic compositions fall within the range of oxidized sulphides described by Toran and Harris (1989). Sulphates derived from the oxidation of sulphides tend to have a $\delta^{34}S$ signature that is marginally more depleted than their source sulphides (by approximately 2 to 6 per mil, Toran and Harris 1989). Because Group 1 contains samples collected from all of the geologic formations, the sulphur isotopic composition cannot be attributed to the formation-scale differences in sulphate predominance that are observed in the Piper diagram (Figure 4.4). Although Group 1 contains samples from all geologic formations, the majority of the samples are from the Guelph and Goat Island formations which form the major regional hydrostratigraphic units of the study area.

The redox trend for the Group 1 groundwater is relatively aerobic, falling primarily within the Oxygen-Nitrate redox zones (Champ et al.1979). These waters have high Eh (up to 398 mV), consistent with the measurable DO (up to 85% sat.) at many locations, non-detect or very low dissolved iron-manganese concentrations, and no detectable H_2S (<0.01 mg/L) (see Guelph and Goat Island formation HSU recharge chemistry, (Table 4.1a,b). The relatively aerobic conditions in the Group 1 groundwater would support the oxidation of sulphides such as those in the overlying glacial sediments or the pyrites in bedrock, described by Brunton (2009). Therefore, the observed isotopic signature of the Group 1 samples is corroborated by the groundwater redox chemistry.

Group 3: Silurian Evaporite Composition

Group 3 groundwater is the most $\delta^{34}S_{SO4}$ isotopically enriched, with values falling in the range reported for Silurian evaporites described by Claypool et al. (1980) (Figure 4.8A). The tritium values for Group 3 are below detection, indicating sub-modern, pre-1950s recharge. Like the tritium values, the redox trend of the Group 3 samples also suggests longer residence times. The Group 3 redox trend is much more reducing than Group 1, falling within the Iron-Manganese to Sulphide dominance zones, indicating redox evolution in closed systems (Champ et al. 1979). The Group 3 groundwater has low Eh (~ 50 mV), consistent with an absence of DO, some Mn and Fe, and measurable H_2S for most areas of up to 140 ug/L (see evolved chemical end members, Table 4.1a,b).

Group 2: Mixed/Marine Evaporite Composition

The sulphur isotopic composition of the Group 2 samples represents a near linear mixing line between Group 1 and Group 3, falling within the range expected for marine evaporites, though with a more depleted sulphur isotopic composition than the Silurian range described by Claypool et al. (1980) (Figure 4.8A).

Gypsum Saturation: Water-Rock Interaction

To assess the relationship between gypsum equilibrium and the sulphur isotopic composition, the $\delta^{34}S_{SO4}$ is plotted against the saturation index (SI) for gypsum (Figure 4.8B). The SI for gypsum for the entire groundwater dataset is below saturation (0), ranging from -3 to nearly 0. With the exception of one outlier containing a tritium value below detection (< 0.8 TU), the Group 1 groundwater falls within a narrow SI range that is the lowest of the entire dataset, with tritium values that are the highest. In contrast, the Group 3 samples have a broad range of saturation indices, and this range contains the samples with the highest SI's and no detectible tritium (Figure 4.8B).

Although the broad range of SI values is influenced by the formation-scale differences in relative sulphate content, as shown on the Piper diagram (Figure 4.4), SI also appears be influenced by groundwater residence time. As groundwater residence time increases, demonstrated with progressive loss of tritium, groundwater approaches gypsum saturation as well as the sulphur isotopic composition of the Silurian-age, Group 3 gypsum (Figure 4.8B). An evolution of Group 1 to Group 3 groundwater would begin with pyrite oxidation at recharge, followed by the dissolution of gypsum along the groundwater flowpath. Gypsum dissolution along the flowpath would increase the SI and cause a shift in the sulphur isotopic composition towards that of the host bedrock, both of which are observed (Figure 4.8B). This concept is further supported by the observed increase in dissolved sulphate from the recharge to the evolved chemical end members (Table 4.1a,b).

4.5 DELINEATING REGIONAL-SCALE RECHARGE AREAS AND CHEMICAL EVOLUTION

The development of conceptual models of regional-scale recharge trends and groundwater evolution for the Guelph and Goat Island formation HSUs (Figures 4.9 and 4.10, respectively) are presented in the following sections. These conceptual models were developed using the hydrogeological, chemical and isotopic information previously described, within the context of the geology of the glacial sediments.

Recharge area boundaries were defined using multiple lines of evidence, beginning with separate tritium assessments for areas north and south of the BNGS influence. South of the area of BNGS influence, recharge area boundaries were first roughly sketched following the 10 TU contour from the interpolation presented in Figure 4.5A. The 10 TU contour reflects groundwater recharged roughly in the past decade, based on decay of the provincial average tritium value (17 TU) for southern Ontario (IAEA 2015 https://nucleus.iaea.org/Pages/GNIPR.aspx) and an assumption of advective transport. In the north, within the presumed area of influence of the BNGS (Figure 4.5A), a recharge boundary was roughly sketched following 20 TU contour. Because average levels of TU in precipitation are not known, the 20 TU contour was selected for the north to reflect the higher tritium observed there, which are approximately double those measured in the south. Because the tritium contours shown previously were drawn using a larger dataset from bedrock wells with no stratigraphic control, these initial recharge areas shown on Figure 4.5A, are tested and refined using the hydrochemistry information for the high-quality Guelph and Goat Island formation HSU wells from the present investigation. Final recharge boundaries are shaped using the glacial sediment thickness map of Gao et al. (2007) and the surficial geology map of Ontario (Ontario Geological Survey 2010) to roughly reflect the geometry of individual or groups of key landforms that appear to be controlling recharge to the bedrock groundwater. This final shaping of recharge boundaries using glacial sediment mapping and information is intended to account for the hydraulic characteristics of the glacial sediments. This step is essential because the groundwater sampling density does not capture the heterogeneity of the glacial sediments that controls where recharge is entering the bedrock groundwater systems. Therefore, the glacial geology maps provide insight into where recharge might be occurring in areas where bedrock groundwater sampling data are not available.

The Guelph Fm HSU: Recharge Areas and Groundwater Evolution

The Guelph Formation recharge areas are presented in Figure 4.9, shown within the context of the regional groundwater flow direction for the Guelph Fm HSU. Each of the four identifiable recharge areas is also superimposed on the tritium contours (9a,9d,9g,9j), on the glacial sediment thickness map of Gao et al. (2007), also showing DO content (9b,9e,9h, 9k) and on the surficial geology map of Ontario (Ontario Geological Survey 2010), (9c,9f,9i,9l). Each identified recharge also area exhibits a downward hydraulic gradient in the multilevel monitoring wells that define it.

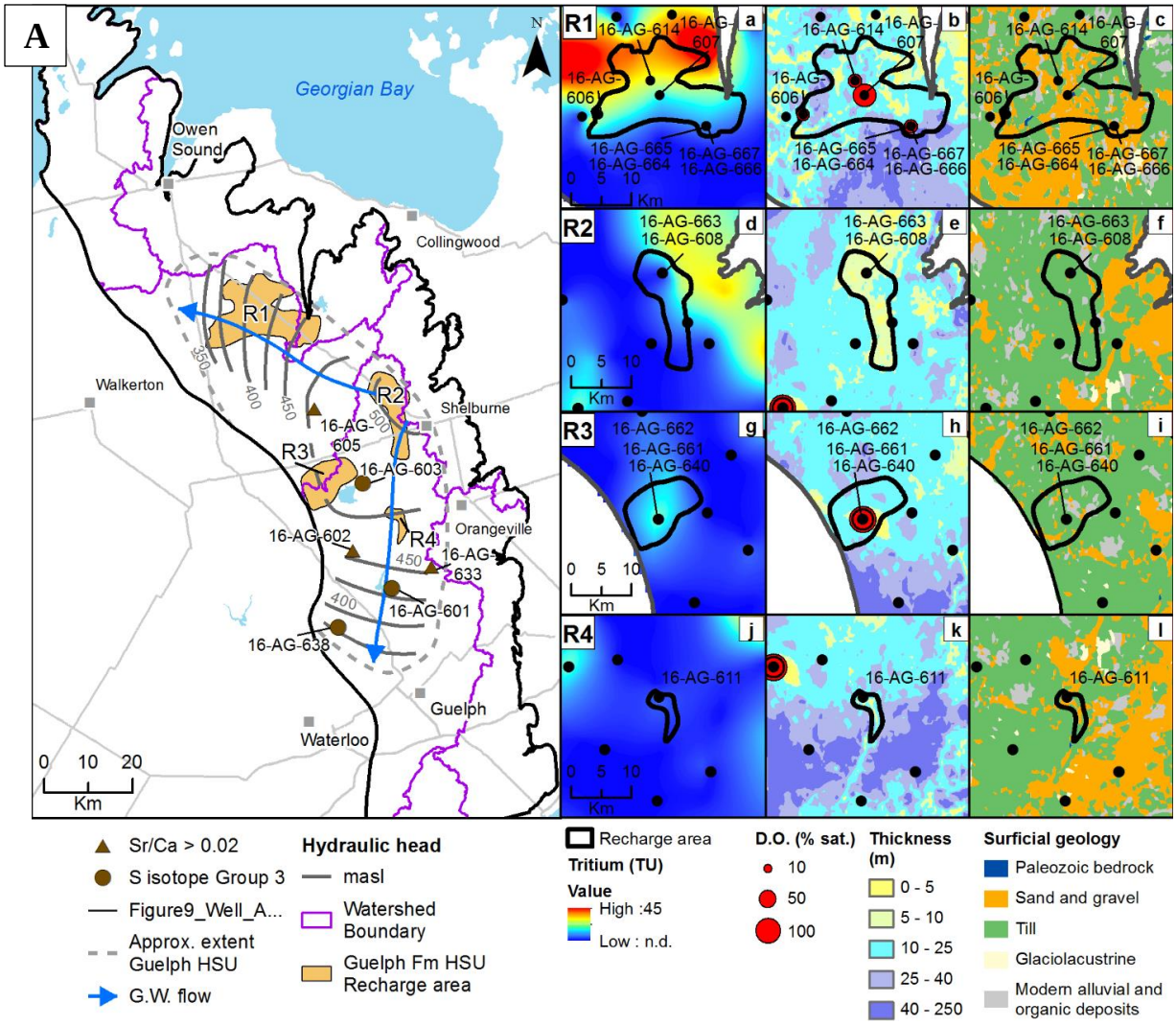

Figure 4.9. Recharge areas for the Guelph Fm HSU are symbolized with *orange polygons* on Panel A. The piezometric surface and groundwater flow direction for the Guelph Fm HSU are shown in grey and blue, respectively, taken from Figure 4.3A. Watershed boundaries are symbolized with *purple lines*. Indicators of evolved chemistry are shown with *brown circles* for Sr/Ca ratios greater than 0.02, and *brown triangles* for sulphur isotope Group 3 samples. The small panels to the right of the Panel A are close-ups of each of the four recharge areas, shown superimposed on tritium contours (9a,d,g,i), the glacial sediment thickness of Gao et al. (2007) (9b,e,h,k) with also shows DO in bedrock, and a simplification of the surficial geology of Ontario (Ontario Geological Survey 2010) (9c,f,i,l).

Recharge area 1 (R1): The glacial sediments of R1 comprise glacial fluvial outwash sands and gravels, deposited during the Late Wisconsin episode, shown as sands and gravels on Figure 4.9c. There are also several small areas of exposed bedrock within R1, shown in dark blue (Figure 4.9c) providing direct access for recharge waters to enter the Guelph Fm HSU. Glacial sediment thickness ranges from 0 to 50 m within R1 (Figure 4.9b), though at the four well locations sampled, the sediment thickness does not exceed 20 m. The hydrochemistry for Guelph Fm HSU wells within R1 is aerobic (Table 4.1a,b), containing measurable dissolved oxygen and an Eh range within the oxygen-nitrate zone, indicative of

recharge area groundwater (Champ et al. 1979). The strontium isotopes and Sr/Ca ratio for R1 also provide evidence of recent recharge, with Sr isotope values being more radiogenic than the Guelph Fm bedrock range of values, suggesting disequilibrium between water and rock (Figure 4.7A, Table 4.1a,b), and very small Sr/Ca ratios, well below the "evolved" threshold of 0.02 (Figure 4.7B, Table 4.1a,b). Sulphur isotopes and gypsum equilibrium values for R1 water also indicate recent recharge, with S isotope values falling within the Group 1 range (Figure 4.8A) and a low gypsum saturation index for these samples (Figure 4.8B, Table 4.1a,b).

Recharge area 2 (R2): R2 is located in an area of very thin glacial sediments (0-5 m thickness, Figure 4.9e). The sediments comprise the Elma and Tavistock Tills that have been likely been eroded with high permeability ice-contact stratified drift of mainly sands and gravels (Figure 4.9f) (Burt and Dodge 2017). The hydrochemistry for the recharge water for R2 (Table 4.1a,b) resembles the trend described for R1, except that there is no measurable DO in the R2 groundwater and the tritium values are smaller. Although DO is absent in groundwater at R2, the strontium isotopes, sulphur isotopes, gypsum equilibrium and tritium values all meet the criteria for recent recharge (Table 4.1a,b, sample 18-AG-663).

Recharge area 3 (R3): R3 is located near the Dundalk Dome, in the centre of the study area. Glacial sediments in R3 vary in thickness from 0 to 34 metres (Figure 4.9h). The surficial geology consists of Tavistock Till that has been eroded by high-permeability glacial fluvial sands and ice-contact sands and gravels, overlain in some areas by lacustrine sands and bog/organic deposits (Figure 4.9i). The hydrochemistry for the recharge water for R3 (Table 4.1a,b) resembles the hydrochemical trends described in detail for R1.

Recharge area 4 (R4): The glacial sediments of R4 consist primarily of glacial fluvial outwash sands and gravels that have eroded through Tavistock Till to form the modern day Grand River channel (Figure 4.9l). R4 is located in a section of the Grand River channel that contains areas of bedrock outcrop, though these are difficult to see at the scale presented in Figure 4.9l. The thickness of the glacial sediments surrounding R3 increases significantly just south of the recharge area (Figure 4.9k). The hydrochemical profile for R4 does not perfectly match those previously described for R1 through R3, with no DO, a low tritium value (3.8 TU) and higher Fe and Mn concentrations, which suggest that these waters are more evolved than those of the other recharge areas (Table 4.1a,b). Inclusion of R4 as a recharge area is supported by the non-detect tritium trend observed just up-gradient (Figure 4.5, Figure 4.9j), which suggests that the detectable tritium at R4 is due to local recharge. The apparently more evolved chemistry observed at R4 might be due to the mixing of recharge at this location with older, upgradient groundwater. The absence of a multi-level monitoring well in the Guelph Formation HSU at

R4 precludes confirmation of vertical gradients at this location. Therefore, R4 has been identified as a possible recharge area by hydrochemical evidence alone.

The Goat Island Fm HSU: Recharge Areas

Because the Goat Island Fm HSU underlies the Guelph Fm HSU, the entire footprint of the Guelph FM HSU is considered to be a possible recharge area where downward gradients between these two formations exist (for downward gradients, see Figure 4.3C). Recharge areas for the Goat Island Fm HSU are mapped beyond the footprint of the Guelph Fm HSU, using the approach just described for the Guelph Fm HSU. Three regional-scale recharge areas have been identified for the Goat Island Fm HSU and these are located only in the northern part of the study area (Figure 4.10).

Recharge areas (R1, R2, R3): R1 and R2 are located in an area that consists primarily of bedrock outcrop, near the edge of the Niagara Escarpment (Figure 4.10b, 4.10c, Figure 4.10e, 4.10f). The glacial sediments of R3 are thin (0-15 m), and they consist of Elma Till that has been eroded in areas by glaciofluvial sands and gravels (Ontario Geological Survey 2010, Figure 10h,10i). Separating R2 and R3 is an area of very thick glacial sediments, representing a sediment-filled bedrock re-entrant valley (Eyles et al. 1993). The recharge waters for R1, R2 and R3 (Table 4.1a,b) are aerobic, containing measurable dissolved oxygen and an Eh range just at the transition from the oxygen-nitrate zone to the iron-manganese zone (Champ et al. 1979). Tritium values in these recharge area groundwaters are the highest observed in the study area (median = 28 TU), showing evidence of the influence of the BNGS on tritium values in precipitation. The strontium isotopes and Sr/Ca ratio are also indicative of recent recharge, with Sr isotope values that are more radiogenic than the Goat Island Fm bedrock range of values (Figure 4.7A), and Sr/Ca ratios well below the "evolved" threshold of 0.02 (median 0.0009). Sulphur isotopes fall within the Group 1 range (Figure 4.8A) and gypsum saturation indices are low (median = -2.5), suggesting disequilibrium between water and rock.

Chemical Evolution, Downgradient of Recharge Areas

The chemical evolution of groundwater generally follows the same trend for the Guelph and Goat Island formation HSUs. As groundwater moves away from recharge areas, DO is consumed, redox conditions shift to a lower Eh range (~50 mV), with some dissolved Fe and Mn present, and increasing H_2S concentrations (median values for end members presented in Table 4.1a,b). Carbonate mineral equilibrium also shifts as the systems migrate from open (exposed to atmospheric gases O_2 and CO_2) to closed (disconnected from atmospheric gases). Total dissolved strontium increases with evolution, as does the Sr/ Ca ratios (>0.02) (Figure 4.7B, Table 4.1a,b). The sulphur isotope characteristics also shift

with evolution, changing from pyrite oxidation (Group 1) at recharge, to the Silurian-age evaporite signature of Group 3 (Figure 4.8, Table 4.1a,b). An increase in gypsum dissolution is also observed along the groundwater flowpath. This is demonstrated by an increase in dissolved sulphate and an increase in the gypsum SI with residence time coinciding with a decrease in tritium levels (Figure 4.8B, Table 4.1a,b). The evolved chemical end member is fairly consistent for the entire Guelph Fm HSU, and is similar to the evolved chemical end member for the *southern* Goat Island Fm HSU. The evolved chemical end member for Goat Island Fm HSU in the north is slightly different, having higher tritium from the influence of BNGS, higher Eh, smaller gypsum SI and a Group 2, "mixed" sulphur isotope signature. This apparently less-evolved chemical end member for the Goat Island Fm HSU in the north occurs beyond the extent of the Guelph Formation, where the Goat Island Formation outcrops and glacial sediments are mostly absent.

Geographically, sampling locations where evolved chemical end members have been observed are shown on Figures 4.9A and 4.10A, with high Sr/Ca ratios symbolized with *brown triangles* and locations with Group 3 sulphur isotopic composition shown with *brown circles*. In both the Guelph and Goat Island formation HSUs, locations where evolved chemical indicators were observed are located outside of, and downgradient of identified recharge areas (Figure 4.9A, Figure 4.10A).

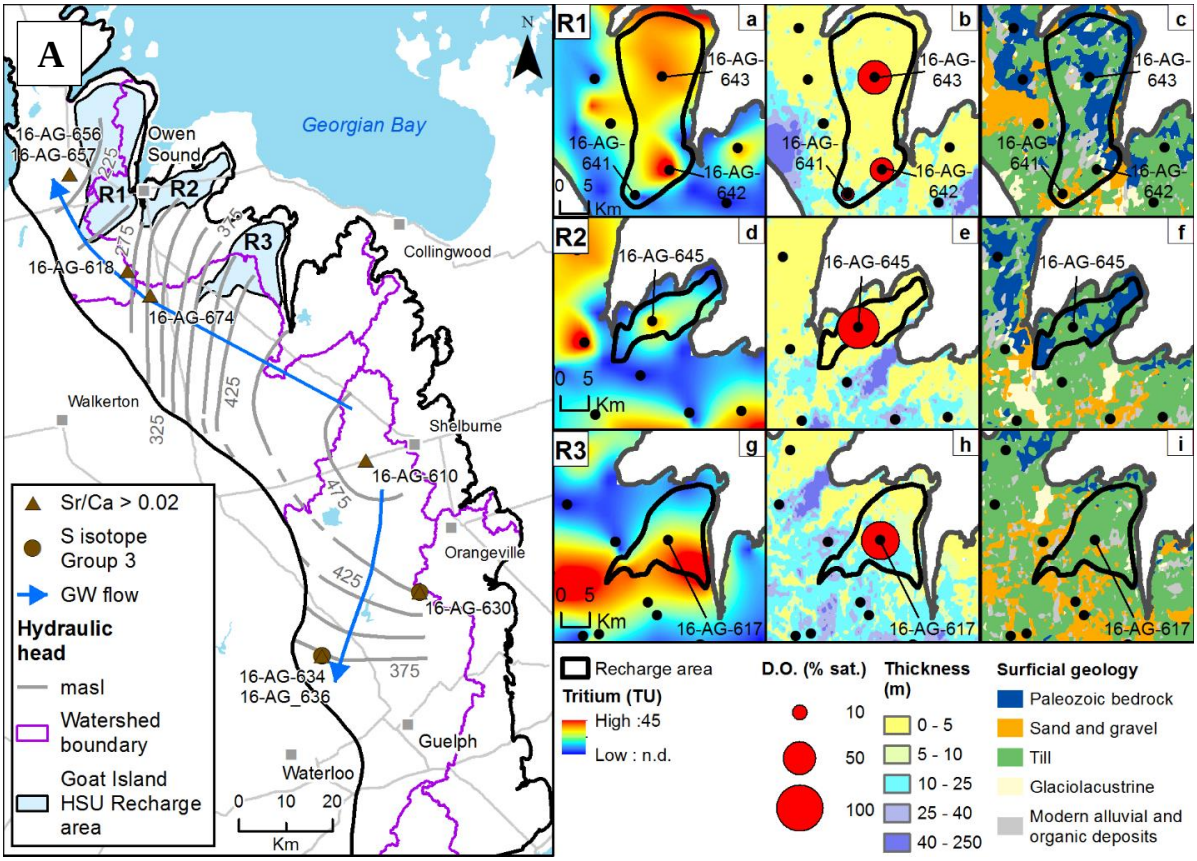

Figure 4.10. Recharge areas for the Goat Island Fm HSU are symbolized with *blue polygons*. The piezometric surface and groundwater flow direction for the Goat Island Fm HSU are shown in grey and blue, respectively, taken from Figure 4.3B. Watershed boundaries are symbolized with *purple lines*. Indicators of evolved chemistry are shown with *brown circles* for Sr/Ca ratios greater than 0.02, and *brown triangles* for sulphur isotope Group 3 samples. The small panels to the right of the main map are close-ups of each of the four recharge areas, shown superimposed on tritium contours (10a,d,g), the glacial sediment thickness of Gao et al. (2007) (10b,e,h) also showing DO in bedrock, and a simplification of the surficial geology of Ontario (Ontario 2010) (10c,f,i).

4.6 SUMMARY AND CONCLUSIONS

A large suite of hydrochemical and isotopic tools has been integrated with geological and hydrogeological information to identify recharge areas and hydrochemical evolution in the carbonate bedrock groundwater systems of the Niagara Escarpment of southern Ontario, Canada. Hydrochemical and isotopic changes within flow systems provided essential evidence for developing a conceptual model of recharge and evolution in this large and complex study area, despite the rather small spatial density of sampling points. In some cases, this geochemical information was the only evidence of recharge. Sulphur isotopes in conjunction with the sulphate mineral equilibrium provided essential information because of the distinct differences in isotopic signatures and gypsum saturation indices between recent recharge and chemically evolved groundwater. Strontium isotopes were not as informative as they have been in non-glaciated carbonate settings (e.g., Banner and Hanson 1990; Uliana et al. 2007). Although strontium isotopes

showed consistent formation-scale trends in bedrock, the geographic variability of the strontium isotopic composition in the glacial sediments precluded their utility for consistently identifying recharge. Despite this, strontium isotopes were still a useful line of evidence in many cases for identifying chemically evolved groundwater, with groundwater taking on the strontium isotopic composition of the bedrock with longer residence times in many cases.

Although tritium alone cannot provide exact estimates of recharge timing, it is still useful as a reconnaissance-level tool for distinguishing between relative ages, particularly for identifying pre- and post-1950's recharge timing. Comparing tritium data with redox parameters and trends, such as the DO comparison offered here (Figure 4.5), can strengthen assessments of relative recharge timing and groundwater residence times. The contouring of the combined bedrock tritium data from this investigation and that of Hamilton (2015) provided valuable insight into the geological controls on recharge when these results were compared with drift thickness and surficial geology. Redox sensitive parameters also provided another test of the conceptual model, as these parameters were assessed against the stability ranges and trends observed by other workers (Champ et al. 1979; Edmunds and Walton 1983).

Provincially defined regions known as Groundwater Source Water Protection areas in Ontario are shaped to match watershed or sub-watershed boundaries (Ontario 2017a). When considered within the context of the groundwater flow system, the regional-scale recharge areas identified here do not align perfectly with those watershed boundaries. There are areas where the bedrock groundwater system underlying one watershed is being recharged in another watershed, such as Guelph Fm HSU R2 which is the recharge source for the Guelph Fm HSU in two separate watersheds (Figure 4.9A), and Goat Island Fm HSU R1 and R2, which span more than one watershed each. Groundwater management and resource allocation in bedrock groundwater systems that are overlain by glacial sediments must consider that watershed, or hydrologic, boundaries are not always appropriate for the management of deeper bedrock systems. In addition to groundwater management area boundaries, the recharge area delineation that was previously conducted with shallow geological mapping and surface flow model calibration (AquaResources Inc. 2009) could be strengthened using the hydrochemical and isotopic indicators of recharge identified here. The findings of this investigation are timely, as they can support the management of these important bedrock groundwater resources, particularly as Ontario's provincial government makes decisions about resource allocation and the water bottling industry (Ontario 2017b).

This investigation presents a strong conceptual model of regional-scale recharge areas and hydrochemical evolution for the two HSUs of the study area. The isotopic and geochemical tools used to develop this

conceptual model provided critical new insight into the regional groundwater flow systems. Because the behaviour of these tools is predictable within the context of the of chemical controls on the groundwater system (e.g. connection with atmosphere, isotopic fractionation and mineralogy), these tools provide predictive insight at the regional scale, despite the relatively sparse network of sampling points. Unlike isotopic and geochemical tools, physical data are less predictive over large areas and between monitoring points, and thus regional characterization would not be possible from physical data alone. However, as is demonstrated here, the most insight is provided from the integration of isotopic and geochemical tools within the context of the physical groundwater flow system.

Several single mineral-specific, hydrochemical or isotopic processes have been assessed individually to support the conceptual model development. What has not yet been assessed is the interaction of these hydrochemical processes with one another. Reactive transport modeling would provide a rigorous test of this conceptual model by considering all of the hydrochemical and isotopic processes at once, within the context of the groundwater flow system. Such an exercise, would provide a quantitative step towards assessing the geochemical processes within each hydrostratigraphic unit.

Table 4.1a: Field parameters, cations and strontium isotope data from the summer 2016 sampling event.

		pH	ORP mV	Eh	DO %sat	Ca (mg/L)	Na (mg/L)	Mg (mg/L)	Fe (mg/L)	Mn (mg/L)	Sr (mg/L)	Sr/Ca	$^{87/86}$ Sr
Guelph HSU: R1	16-AG-606	7.09	201	398	24	71.68	5.11	35.60	n.d. (0.00047)	n.d. (0.0001)	0.15	0.002	0.7092
	16-AG-607	7.12	190	387	85	64.07	1.04	28.64	n.d. (0.00047)	n.d. (0.0001)	0.05	0.001	0.7091
	16-AG-614	7.26	157	354	28	70.54	2.26	37.40	n.d. (0.00047)	n.d. (0.0001)	0.08	0.001	0.7092
	16-AG-665	7.37	-79	118	29	57.70	1.24	29.07	0.0013	0.0008	0.07	0.001	0.7093
Guelph HSU: R2	16-AG-663	7.08	72	269	0	119.12	63.63	54.60	0.0194	0.0161	0.39	0.003	0.7096
Guelph HSU: R3	16-AG-640	7.64	47	244	36	57.95	1.95	30.18	0.0047	0.0002	0.07	0.001	0.7089
	16-AG-661	7.5	-22	175	24	66.91	2.95	28.24	0.0027	0.0004	0.07	0.001	0.7088
	16-AG-662	7.47	-3	194	20	77.91	9.08	37.70	0.0841	0.0063	0.13	0.002	0.7089
Guelph HSU: R4	16-AG-611	7.88	-157	40	0	27.96	30.23	23.03	0.4150	0.0744	0.32	0.012	0.7104
Recharge Median		7.37	47	244	24	66.91	2.95	30.18	0.0121	0.0036	0.08	14.30	0.001
Guelph HSU: Evolved chemical end member	16-AG-603	7.37	-73	124	0	48.09	16.04	26.38	0.021	0.021	1.420	0.03	0.7087
	16-AG-631	7.47	-193	4	0	51.68	7.48	21.41	0.049	0.005	0.428	0.01	0.7094
	16-AG-632	7.42	-222	-25	0	47.63	6.63	21.34	0.115	0.002	0.336	0.01	0.7094
	16-AG-602	7.74	-190	7	0	24.56	31.86	10.48	0.252	0.013	0.336	0.01	0.7099
	16-AG-601	7.53	-117	80	0	31.69	15.28	15.25	0.042	0.110	1.973	0.06	0.7088
	16-AG-628	7.09	-137	60	0	540.95	15.16	87.30	0.437	0.029	8.382	0.02	0.7090
	16-AG-630	7.11	-180	17	0	489.82	9.66	87.40	0.301	0.019	8.267	0.02	0.7089
	16-AG-634	7.74	-141	56	0	56.25	15.59	32.40	0.329	0.019	1.558	0.03	0.7092
	16-AG-636	7.6	-100	97	0	56.31	15.00	22.71	0.246	0.054	0.873	0.02	0.7091
	16-AG-637	7.6	-151	46	0	53.16	14.77	22.26	0.559	0.037	0.845	0.02	0.7091
Evolved Median		7.5	-146	51	0	52.42	15.08	22.49	0.249	0.020	1.15	44.73	0.02
Goat Island HSU: R1	16-AG-641	7.36	74	271	8	67.30	3.75	32.10	0.003	0.157	0.17	0.0025	0.7097
	16-AG-642	7.11	158	355	27	88.41	3.58	30.69	n.d. (0.0005)	0.194	0.08	0.0009	0.7095
	16-AG-643	7.10	122	319	56	73.03	7.54	30.11	0.025	n.d. (0.0001)	0.06	0.0009	0.7099
Goat Island HSU: R2	16-AG-645	7.17	157	354	80	73.64	9.34	32.70	n.d. (0.0005)	n.d. (0.0001)	0.05	0.0006	0.7098

		pH	ORP mV	Eh	DO %sat	Ca (mg/L)	Na (mg/L)	Mg (mg/L)	Fe (mg/L)	Mn (mg/L)	Sr (mg/L)	Sr/Ca	$^{87/86}$ Sr
Goat Island HSU: R3	16-AG-617	7.09	194	391	66	92.15	1.47	36.25	n.d. (0.0005)	n.d. (0.0001)	0.07	0.0008	0.7094
Recharge Median		7.11	157.40	354	55.50	73.64	3.75	32.10	n.d. (0.0005)	n.d. (0.0001)	0.07	11.00	0.0009
Goat Island HSU: Evolved chemical end member North	16-AG-656	7.40	-84	113	0	63.88	2.18	43.50	0.082	0.002	1.65	0.03	0.7089
	16-AG-657	7.58	-94	103	0	47.27	15.72	60.10	0.100	0.003	1.67	0.04	0.7090
	16-AG-674	7.42	-112	85	0	66.52	10.83	29.09	0.051	0.001	7.19	0.11	0.7087
Evolved Median		7.42	-94	103	0	63.88	10.83	43.50	0.082	0.002	1.67	21.56	0.04
Goat Island HSU: Evolved chemical end member South	16-AG-630	7.11	-180	17	0	489.82	9.66	87.40	0.301	0.019	8.27	0.02	0.7089
	16-AG-634	7.74	-141	56	0	56.25	15.59	32.40	0.329	0.019	1.56	0.03	0.7092
	16-AG-636	7.60	-100	97	0	56.31	15.00	22.71	0.246	0.054	0.87	0.02	0.7091
Evolved Median		7.60	-141	56	0	56.31	15.00	32.40	0.301	0.019	1.56	66.72	0.02

Table 4.1b: Anions and isotopic data from the summer 2016 sampling event

		Cl (mg/L)	NO_3 (mg/L)	SO4 (mg/L)	HCO_3 (mg/L)	H2S	$\delta^{34}S\_SO_4$	$\delta^{18}O(SO_4)$	Sulphur Group	SI Gypsum	Tritium (TU)
Guelph HSU: R1	16-AG-606	6.14	n.d. (0.0015)	14.90	390	n.d. (0.005)	0.80	-2.8	1	-2.4	15.4
	16-AG-607	1.40	n.d. (0.0015)	8.58	315	n.d. (0.005)	3.40	-2.3	1	-2.7	10.2
	16-AG-614	1.87	n.d. (0.0015)	18.15	357	n.d. (0.005)	-0.60	-4.4	1	-2.3	17.5
	16-AG-665	0.75	n.d. (0.0015)	11.41	279	n.d. (0.005)	0.00	-2.1	1	-2.6	5.5
Guelph HSU: R2	16-AG-663	201.97	n.d. (0.0015)	15.50	373	n.d. (0.005)	3.30	3.3	1	-2.3	14.4
Guelph HSU: R3	16-AG-640	5.31	n.d. (0.0015)	12.84	355	n.d. (0.005)	3.90	-1.0	1	-2.6	6.5
	16-AG-661	10.73	0.008	14.30	256	n.d. (0.005)	no data	no data	n/a	-2.4	12.4
	16-AG-662	31.59	n.d. (0.0015)	25.64	333	n.d. (0.005)	1.60	-4.1	1	-2.2	13.3
Guelph HSU: R4	16-AG-611	33.49	n.d. (0.0015)	13.40	204	n.d. (0.005)	4.00	-2.0	1	-2.8	3.8
Recharge Median		6.14	n.d. (0.0015)	14.30	333	333	2.45	-2.2	1	-2.4	12.4
Guelph HSU: Evolved chemical end member	16-AG-603	4.94	n.d. (0.0015)	65.85	229	n.d. (0.005)	20.1	8.49	2	-1.9	n.d. (0.8)
	16-AG-631	0.45	n.d. (0.0015)	13.98	200	0.14	15.7	12.68	2	-2.5	n.d. (0.8)
	16-AG-632	0.41	n.d. (0.0015)	12.68	213	0.07	17.9	13.23	2	-2.6	n.d. (0.8)
	16-AG-602	1.54	n.d. (0.0015)	10.51	195	n.d. (0.005)	27.9	14.43	3	-2.9	n.d. (0.8)
	16-AG-601	0.67	n.d. (0.0015)	46.33	180	n.d. (0.005)	27.2	15.31	3	-2.1	n.d. (0.8)
	16-AG-628	7.57	n.d. (0.0015)	1370.89	252	0.19	28.8	15.54	3	0.0	n.d. (0.8)
	16-AG-630	3.57	n.d. (0.0015)	1303.16	255	0.32	28.6	15.27	3	-0.1	n.d. (0.8)
	16-AG-634	6.96	n.d. (0.0015)	66.72	261	0.1	28.6	14.03	3	-1.9	n.d. (0.8)
	16-AG-636	5.61	n.d. (0.0015)	43.12	260	0.12	27.8	13.33	3	-2.1	n.d. (0.8)
	16-AG-637	5.75	n.d. (0.0015)	42.17	258	0.23	30.1	13.64	3	-2.1	n.d. (0.8)
Evolved Median		4.25	n.d.	44.73	240.50	240.50	27.85	13.84	3	-2.1	n.d. (0.8)
Goat Island HSU: R1	16-AG-641	2.42	n.d. (0.0015)	25.05	307	n.d. (0.005)	-2.7	-6.12	1	-2.2	17
	16-AG-642	5.27	n.d. (0.0015)	17.74	338	n.d. (0.005)	-3.7	-6.5	1	-2.3	41.1
	16-AG-643	12.85	0.01	10.97	334	n.d. (0.005)	-1.1	-2.91	1	-2.5	28.4
Goat Island HSU: R2	16-AG-645	16.86	n.d. (0.0015)	11.00	312	n.d. (0.005)	3.8	-0.93	1	-2.5	27.3

		Cl (mg/L)	NO_3 (mg/L)	SO4 (mg/L)	HCO_3 (mg/L)	H2S	$\delta^{34}S\_SO_4$	$\delta^{18}O(SO_4)$	Sulphur Group	SI Gypsum	Tritium (TU)
Goat Island HSU: R3	16-AG-617	5.71	n.d. (0.0015)	5.27	335	n.d. (0.005)	no data	no data	n/a	-2.8	28.3
Recharge Median		5.71	n.d. (0.005)	11.00	334.00	334.00	-1.90	-4.52	1.00	-2.54	28.30
Goat Island HSU: Evolved chemical end member North	16-AG-656	3.00	0.00	18.95	327	0.15	8	2.83	1	-2.4	19.8
	16-AG-657	55.19	0.00	21.56	305	0.10	20.3	7.78	2	-2.5	10.9
	16-AG-674	17.93	0.00	93.93	277	0.05	24.5	9.73	2	-1.6	1.1
Evolved Median		17.93	0.00	21.56	305	305	20.3	7.78	2	-2.4	10.9
Goat Island HSU: Evolved chemical end member South	16-AG-630	3.57	0.00	1303.16	255	0.32	28.6	15.27	3	-0.1	n.d. (0.8)
	16-AG-634	6.96	0.00	66.72	261	0.10	28.6	14.03	3	-1.9	n.d. (0.8)
	16-AG-636	5.61	0.00	43.12	260	0.12	27.8	13.33	3	-2.1	n.d. (0.8)
Evolved Median		5.61	0.00	66.72	260	260	28.6	14.03	3	-1.9	n.d. (0.8)

Chapter 5 Reactive Transport Modelling in a Regional-Scale Carbonate Groundwater System

5.1 INTRODUCTION

Multiple lines of geochemical, hydrochemical and isotopic evidence support a conceptual model of recharge and groundwater evolution in the regional-scale carbonate groundwater systems of the Niagara Escarpment area, southern Ontario (Chapter 4). These lines of evidence were established by isolating and investigating individual chemical processes, leaving the interactions among these processes untested. In this chapter, a reactive transport model is developed to simulate the geochemical, hydrochemical and isotopic processes that form the conceptual model. The objective of this exercise is to assess the hydrochemistry of the system as a whole, identifying any missed or misunderstood processes or interactions in the conceptual model. The modeling comprises the simulation of a hypothetical groundwater flowpath with the multi-component reactive transport model MIN3P (Mayer et al. 2002). The simulated flowpath is within the Guelph Formation, one of the main hydrostratigraphic units of the study area.

Reactive transport modeling is under-utilized for regional-scale investigations. For these large study areas, workers have tended to rely on simplistic chemical modeling approaches, such as mass balance and inverse mixing models (e.g., Toth and Katz 2006; Uliana et al. 2007; El-Kadi et al. 2010; Xie et al. 2013) that vary in their ability to simulate kinetic processes and have limited or no capability to simulate flow. In contrast, reactive transport modeling has the advantage of incorporating equilibrium and kinetic chemical processes with transport and groundwater flow. In addition to meeting the objective of assessing the conceptual model, modeling results will also be used to evaluate the suitability of reactive transport modeling for investigating regional-scale groundwater systems.

5.2 STUDY AREA DESCRIPTION

The 8,000 km^2 study area is located in southern Ontario, and is bounded by Lake Huron to the north, the Niagara Escarpment to the east, the Algonquin Arch basement structural feature in the south and the outcrop of the Late Silurian Salina Group evaporites to the west (Figure 5.1). The Early Silurian carbonate bedrock formations of the study area, more specifically the Lockport Group (Brunton 2009), contain significant and high-quality groundwater resources where they out-crop or sub-crop along the Niagara Escarpment (Sharpe et al. 2013).

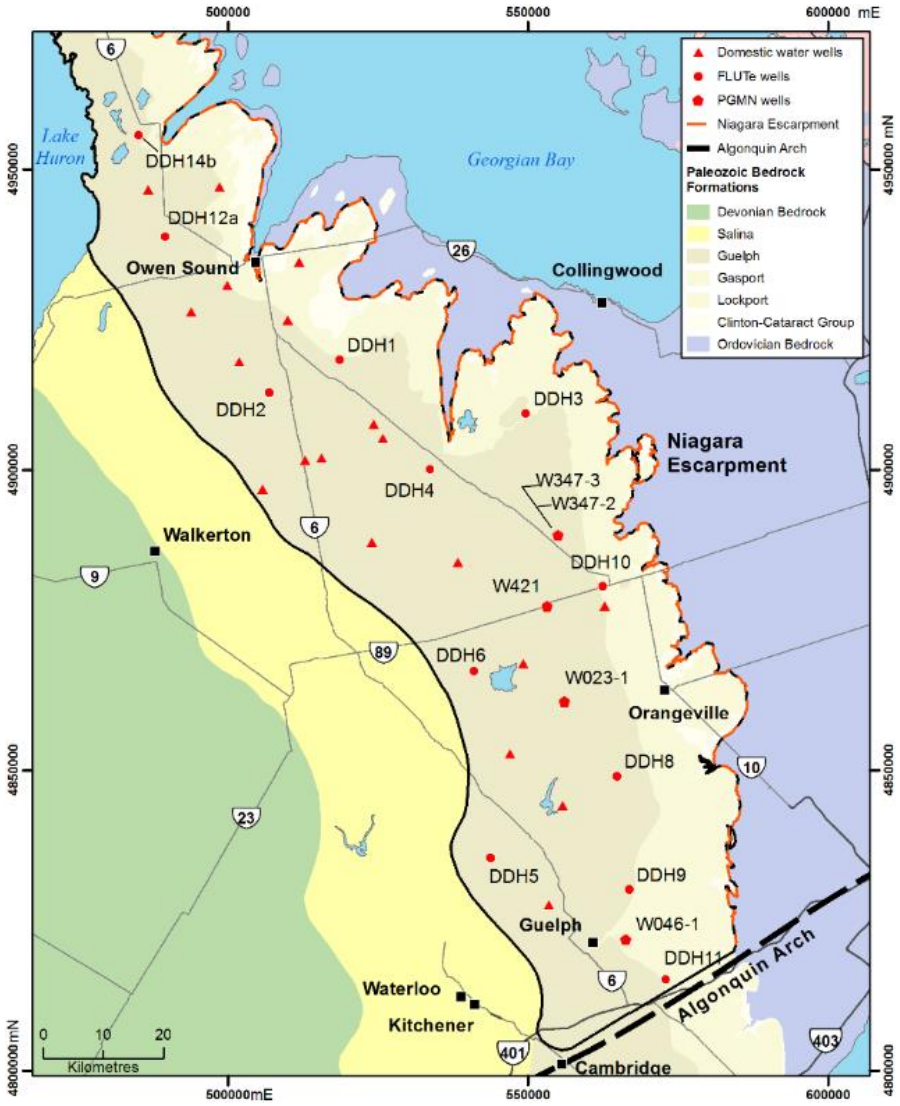

Figure 5.1. Study area showing groundwater sampling locations from the summer 2016 field campaign. Sampling locations are symbolized in *red*, with a different symbol shape for each of the three well types. The DDH wells are multi-level, containing 3-5 sampling ports at each location. Figure 5.1 is a reproduced from Chapter 4 (Figure 4.1).

5.2.1 Geology, Mineralogy and Hydrostratigraphy

The Early Silurian, Lockport Group bedrock formations comprise an approximately 100 m thick succession of stacked marine carbonates (Brunton 2009). In ascending order, the Lockport Group consists of the following stratigraphic formations; the Gasport, the Goat Island, the Eramosa and the Guelph (Brunton 2009; Brunton and Brintnell 2011). The Guelph Formation, which is the subject of this modeling investigation, is a high-purity dolomite containing very low silica levels, with localized sphalerite and galena mineralization (Brunton et al. 2007; Rowell 2015). Whole rock geochemistry values for the Guelph Formation demonstrate that the mineralogy primarily comprises carbonates, with an average carbonate percent of 98.53 (Table 5.1). Because strontium minerals were not identified in the

petrographic analyses (Brunton et al. 2007), the total strontium measured in the whole rock analysis by Rowell (2015) is assumed be a small component of the dolomite mineral structure itself. In addition to the petrographic and whole rock analyses, strontium isotopic analyses were conducted on 34 samples taken from a single core of Guelph Formation bedrock. The average $^{87}Sr/^{86}Sr$ isotope ratio from those analyses is 0.7085, within a range of 0.7082 to 0.7086 (Chapter 4, Figure 4.7A).

Dissolved organic carbon is consistently present in low concentrations across the study area in Guelph Formation groundwater. The source of these dissolved organics is assumed to be the Eramosa Fm, which is the geologic unit underlying the Guelph Fm. The Eramosa Fm is described as petroliferous (Armstrong and Carter 2010), making it a likely organic carbon source.

The occurrence of pyrite across the study area is spatially inconsistent, as it forms in fractures within the carbonate bedrock, precipitated from basin brines (Brunton et al. 2007). The source of gypsum is also spatially inconsistent, owing to its origin from the previously overlying (presently eroded) Salina Group evaporites. The Salina Group contains significant gypsum beds (Armstrong and Carter 2010), which are assumed to have been dissolved and redistributed to the underlying Guelph formation through vertical conduits.

Table 5.1. Whole rock geochemistry data for the Guelph Fm (Rowell 2015)

Mineral/parameter	**Average values (n = 124)**	**Minimum value**	**Max value**
Carb Tot (%)	98.53	87.81	101.01
Ca/Mg	1.42	1.32	2.04
Total S (%)	0.01	<0.01	0.01
Sr (%) (*n = 51*)	0.0057	0.0043	0.0095
Iron oxide %	0.12	0.0	0.41
Manganese oxide (%)	0.02	0.01	0.06

The Guelph and Goat Island formations were identified in Chapter 4 as the two main regional hydrostratigraphic units of the study area. Hydrostratigraphic units were delineated by identifying the stratigraphic position(s) of the most hydraulically conductive portions of the bedrock in high-quality wells using borehole flow metre and geophysical logging profiles (Lee et al. 2011), and in domestic wells, using information from the provincial well drilling records (Ontario 2015). Further detail regarding hydrostratigraphic unit identification and delineation is presented in Chapter 4 (section 4.3.1).

5.2.2 Groundwater Sampling and End Member Chemistry

Groundwater sampling was conducted in the summer of 2016, comprising the collection of 67 samples across the 8000 km^2 study area (Figure 5.1). Samples were collected from a variety of different well types, including multi-level monitoring wells containing several sampling ports (DDH wells), provincial groundwater monitoring wells and domestic water supply wells. Descriptions of field methods, QA/QC procedures and analytical methods are provided in Chapter 4, section 3.1. Groundwater data for the Guelph Formation hydrostratigraphic unit (Guelph HSU) are provided in Table 5.2, with data summarized by recharge and evolved hydrochemical end members, with the evolved end member representing groundwaters with the longest residence times.

Table 5.2. Recharge and evolved groundwater end member chemistry for the Guelph HSU.

	Guelph HSU				
	Sample	**Recharge end member (n = 9)**		**Evolved end member (n = 10)**	
	DDH6-2	**Average**	**Median**	**Average**	**Median**
pH	7.5	7.38	7.37	7.47	7.50
Eh	178	242	244	46	51
DO %sat	24.2	27.4	24.2	0.0	0.0
Ca (mg/L)	66.9	68.20	66.91	140.02	52.42
Na (mg/L)	2.9	13.05	2.95	14.75	15.08
Mg (mg/L)	28.24	33.83	30.18	34.69	22.49
Fe (mg/L)	0.002	0.09	0.01	0.24	0.25
Mn (mg/L)	n.d.	0.02	n.d.	0.03	0.02
Sr (mg/L)	0.068	0.15	0.08	2.44	1.15
SO4 (mg/L)	14.29	14.97	14.30	297.54	44.73
HCO3 (mg/L)	256	318.00	333.00	230.30	240.50
Cl (mg/L)	10.7	32.58	6.14	3.75	4.25
NO3 (mg/L)	0.008	n.d. (0.0015)	n.d. (0.0015)	n.d.	n.d.
H2S	n.d. (0.005)	n.d. (0.005)	n.d. (0.005)	0.17	0.14
Sr/Ca	0.001	0.003	0.001	0.021	0.016
87/86 Sr	0.7088	0.7093	0.7092	0.7091	0.7091
δ34S_SO4	0	2.05	2.45	25.27	27.85
δ18O(SO4)	-	-1.91	-2.21	13.60	13.84
SI Gypsum	-2.45	-2.48	-2.44	-1.81	-2.07
Tritium (TU)	12	11.0	12.4	n.d. (0.8)	n.d. (0.8)
CH_2O (mg/L)	2.5	3.7	2.6	4.0	2.5

5.2.3 Conceptual Model of Geochemical Processes from Recharge with Hydrochemical Evolution

5.2.3.1 RECHARGE

Gypsum under-saturation is greatest in recharge areas (Table 5.2), indicating that gypsum dissolution is likely (Chapter 4, Figure 4.8B). However, groundwater residence times are not long enough in recharge areas for sufficient quantities of gypsum to dissolve and impart its Silurian $\delta^{34}S_{SO4}$ signature (Toran and Harris 1989) on the groundwater. Instead, the $\delta^{34}S_{SO4}$ signature in recharge areas falls within the range expected of pyrite oxidation (Claypool et al. 1980), indicating this as the dominant process for sulphate production (Table 5.2; Chapter 4, Figure 4.8A). The oxidation of sulphide during pyrite oxidation also produces ferrous iron, which is unstable in aerobic environments and quickly oxidizes to ferric iron and precipitates. It is assumed that the precipitate takes the form of ferrihydrite because of the prevalence of this mineral in natural groundwater systems (Jambor and Dutrizac 1998).

Dolomite is assumed to dissolve irreversibly, as it cannot precipitate in low temperature groundwater systems (Hardie 1987), such as those of the study area. Dolomite dissolution releases calcium, magnesium and small quantities of strontium. The increase in concentration of these cations is assumed, based on saturation indices, to result in the precipitation of calcite and magnesite. With calcium precipitating, the ratio of dissolved strontium to calcium (Sr/Ca) increases as dolomite continues to dissolve with hydrochemical evolution (Chapter 4, Figure 4.7B). The strontium isotopic composition ($^{87}Sr/^{86}Sr$) in recharge area groundwater is more radiogenic than the Guelph Fm bedrock value, though it matches the $^{87}Sr/^{86}Sr$ signature of the Clinton-Cataract Group (Dollar et al. 1991), from which some of the overburden sediments were derived through glacial erosion.

The redox trend for recharge areas falls within the Eh range described by Champ et al. (1979) as the dissolved oxygen/nitrate zone, indicative of recharge areas in closed systems. Dissolved oxygen is present in recharge areas, while concentrations of dissolved iron, manganese and hydrogen sulphide are not detected in this aerobic environment (Table 5.2). Tritium values in recharge areas are the highest reported for the study area, most closely reflecting the local weighted average precipitation levels.

5.2.3.2 HYDROCHEMICAL EVOLUTION

At its most hydrochemically evolved, the $\delta^{34}S_{SO4}$ signature matches that of Silurian age gypsum as determined by Toran and Harris (1989) (Table 5.2; Chapter 4, Figure 4.8). This shift from a $\delta^{34}S_{SO4}$ signature indicative of pyrite oxidation towards the Silurian signature is representative of gypsum

dissolution and sulphate reduction that occurs with increasing groundwater residence time. An increase in dissolved sulphate and gypsum SI are also observed with hydrochemical evolution, providing further evidence that gypsum dissolution is a source of the $\delta^{34}S_{SO4}$ isotopic shift (Table 5.2; Chapter 4, Figure 4.8B).

Dolomite is assumed to dissolve along the entire groundwater flowpath. The observed increase in the Sr/Ca ratio with hydrochemical evolution supports this assumption as dolomite dissolution releases strontium and calcite continues to precipitate (Table 5.2; Chapter 4, Figure 4.7B). At its most evolved, groundwater chemistry falls within the iron-manganese to sulphide redox zones, as described by Champ et al. (1979), with concentrations of dissolve iron, manganese and hydrogen sulphide increasing with hydrochemical evolution (Table 5.2). The reduction of ferrihydrite, manganese oxide and sulphate by dissolved organic carbon are assumed to be the processes releasing these redox sensitive parameters in the more evolved, reducing regions of the closed system. Small quantities of dissolved organic carbon are ubiquitous across the Guelph HSU, regardless of position within the flow system (Table 5.2). Tritium values in the hydrochemically evolved groundwaters are below detection limits, confirming longer groundwater residence times (Table 5.2).

5.3 REACTIVE TRANSPORT MODELING APPROACH

5.3.1 Model Domain, Physical Properties and Boundaries

The geochemical and isotopic processes described in the conceptual model were simulated using the multi-component reactive transport code MIN3P (Mayer et al., 2002). Reactive transport in the Guelph HSU was simulated with a fully saturated, 1D model. Constant head, Dirichlet boundary conditions were assigned to the start and end boundaries of the flow problem, with hydraulic heads taken from the piezometric surface developed from water level elevations collected in the summer of 2016 (Figure 5.2). The reactive transport boundaries comprise a specified concentration input, Dirichlet condition, for the recharge boundary and a free advective, aqueous mass outflux (Neumann condition), at the end of the flowpath. The specified concentrations at the recharge boundary comprise the chemical analyses for sample DDH6-2, which closely resembles the median recharge end-member values for the Guelph HSU (Table 5.2). Sample DDH6-2 also represents one of the three field values at the recharge boundary against which the simulation is compared (Figure 5.2). The initial conditions within the model domain comprise the median evolved end-member concentrations (Table 5.2). One of the assumptions in the model set-up is that the recharge is only occurring at the input boundary, with closed to atmosphere conditions occurring beyond this point. This assumption does not consider that recharge waters beyond the “significant” recharge occurring that the boundary may influence the hydrochemistry by mixing with

bedrock groundwater along the simulated flowpath. Simulation results may provide an indication of where recharge is occurring along the flowpath with evidence found in poor matching of field observations.

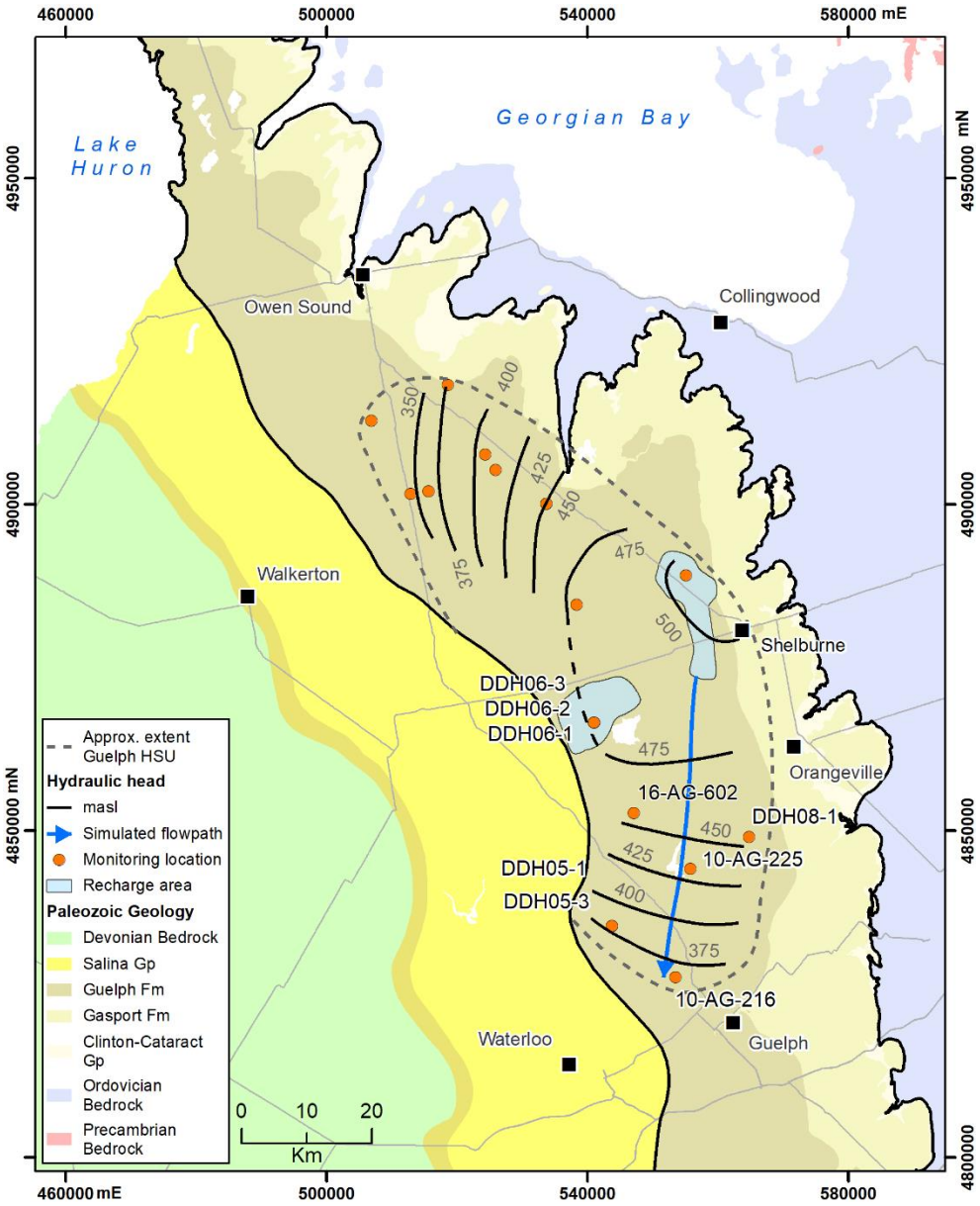

Figure 5.2. The piezometric surface for the Guelph HSU flow system is shown for the study area. The simulated flowpath is represented with a *blue arrow*. Guelph HSU sampling locations are symbolized with *orange dots*. Where multiple sampling ports occur at one location, the station ID's are provided for each port. The recharge areas identified for the Guelph HSU (Chapter 4) are depicted as *light blue polygons*.

The model domain is 50 km long, approximating the greatest distance required for the groundwater system to shift from the recharge to the evolved end-member chemistry. Hydraulic conductivity is represented by a single value throughout the model domain, despite the wide range of values for the

Guelph Formation reported by Priebe et al. (2017a). Porosity was not measured in the study area, though it is assumed to vary significantly due to the heterogeneity and range in carbonate textures described by Priebe et al (2018). A porosity value was taken from the range of values (0.001-23.6 %) measured for the Guelph Fm at a location approximately 50 km south of the study area (Zheng 1999). The model was designed to approximate a hypothetical flowpath that falls within the range of what is realistic, although the groundwater systems of the study area likely contain many flowpaths that differ in length, effective porosity and groundwater velocities.

Table 5.3. 1-D model domain and physical properties

1-D Model Domain	
Discretization	cell l =25 m, n = 2001
Model dimensions	1m x 1m x 50,000 m
Duration of simulation	150 years
Minimum time step / Maximum time step	$1x10^{-8}$ years/ 0.5 years
Physical Properties	
Hydraulic conductivity	$9x10^{-5}$ [a]
Hydraulic head at start/end	475 masl / 375 masl
Porosity	0.005 [b]
Average linear groundwater velocity	1 km/year
Dispersivity	1 m

a: calibrated value, within range reported by Priebe et al. (2017)
b: calibrated value, within range reported by Zheng (1999)

5.3.2 Chemical and Isotopic Processes

5.3.2.1 Mineral Precipitation/Dissolution Reactions

Five minerals are represented in the model to describe precipitation and/or dissolution reactions. These minerals are dolomite, gypsum, calcite, magnesite, ferrihydrite and pyrolusite. Dolomite dissolution is represented as irreversible, with its rate described using the empirically-derived expression of Busenberg and Plummer (1982):

$$R_{dolomite} = k_1 \{H^+\}^{0.5} + k_2 \{H_2 CO_3\}^{0.5} + k_3 \quad (1)$$

$$1.34Ca0.685Mg0.00008SrCO_3 + H^+ \overset{k_1}{\rightarrow} 1.34\, Ca^{2+} + 0.658\, Mg^{2+} + 0.00008\, Sr^{2+} + HCO_3^- \quad (2)$$

$$1.34Ca0.685Mg0.00008SrCO_3 + H_2CO_3 \overset{k_2}{\rightarrow} 1.34\, Ca^{2+} + 0.658\, Mg^{2+} + 0.00008\, Sr^{2+}\, 2\, HCO_3^- \quad (3)$$

$$1.34Ca0.685Mg0.00008SrCO_3 \xrightarrow{k_3} 1.34\,Ca^{2+} + 0.658\,Mg^{2+} + 0.00008\,Sr^{2+} + CO_3^{2-} \quad (4)$$

$$0.00008\,Sr^{2+} = 0.0000468\ {}^{87}Sr^{2+} + 0.0000332\ {}^{86}Sr^{2+} \quad (5)$$

Where $R_{dolomite}$ is the overall reaction rate of dolomite dissolution and k_1, k_2 and k_3 are the rate constants for the three reaction pathways (equations 2 to 4). The Sr isotope ratio is imposed on the dolomite mineral, with the Sr quantity based on the whole rock chemistry of Rowell (Table 5.2, 2015), and the $^{87}Sr/^{86}Sr$ isotopic composition based on the average value for the Guelph Fm bedrock (0.7058, n=34).

Gypsum dissolution and precipitation is represented in the model as two minerals, one each for sulphur isotopes ^{34}S and ^{32}S, following the approach described by Gibson et al. (2010).

$$Ca\,{}^{34}SO_4 \cdot 2H_2O \leftrightarrow Ca^{2+} + {}^{34}SO_4^{-2} + 2H_2O \quad (6)$$

$$Ca\,{}^{32}SO_4 \cdot 2H_2O \leftrightarrow Ca^{2+} + {}^{32}SO_4^{-2} + 2H_2O \quad (7)$$

The Silurian sulphur isotope signature for gypsum described by Toran and Harris (1989) is represented in the initial mineral volume fractions, with a $\delta^{34}S_{SO4}$ value of 28 ‰ (VCDT). This Silurian sulphur isotope signature is observed in the evolved groundwater end member (Table 5.2; Chapter 4, Figure 4.8A). Gypsum precipitation/dissolution is represented in the model as a reversible, surface-controlled reaction with the rate expression:

$${}^{34}R_{gypsum} = -{}^{32}k\left[1 - \left(\frac{IAP}{K}\right)\right] \quad (8)$$

$${}^{32}R_{gypsum} = -{}^{34}k\left[1 - \left(\frac{IAP}{K}\right)\right] \quad (9)$$

Where R_{gypsum} is the reaction rate, ^{34}k and ^{32}k are the rate constants (mol/m^{3}s) for reactions 6 and 7 respectively and K is the equilibrium constant. The mass dependant rate constants, ^{32}k and ^{34}k are a function of the fractionation factor, which is 1 for gypsum dissolution, and the isotope ratio of the gypsum mineral ($^{34}R_S$). The overall rate constant for gypsum dissolution (k_{eff}) equals the sum of the individual rate constants for both isotopes. The individual rate constants are estimated following the approach of Gibson et al. (2010), with the equations:

$${}^{34}k = \frac{k_{eff}}{1+\frac{1}{\alpha\,{}^{34}R_S}} \quad (10)$$

$${}^{32}k = \frac{k_{eff}}{1+\alpha\,{}^{34}R_S} \quad (11)$$

Similar to gypsum, but without the inclusion of isotopes, the precipitation and dissolution of minerals ferrihydrite, magnesite and calcite are represented as reversible, surface-controlled reactions with the same rate expression as that presented in equation 8.

5.3.2.2 REDOX REACTIONS

Redox reactions were included to represent pyrite oxidation in recharge areas, and the reduction of pyrolusite and ferrihydrite by dissolved organic carbon (CH_2O) with chemical evolution. Pyrite oxidation is represented as an irreversible, surface-controlled reaction with the stoichiometry written as:

$$FeS_2\ (s) + H_2O\ + 3.5O_2 = Fe^{2+}\ + 1.915\ {}^{32}SO_4^{-2} + \ +0.0846\ {}^{34}SO_4^{-2} + \ 2H^+ \quad (12)$$

The recharge area $\delta^{34}S_{SO4}$ isotopic composition was applied in the pyrite oxidation stoichiometry in the MIN3P mineral database by imposing a $\delta^{34}S_{SO4}$ of 2.5 ‰ VCDT, representing the median value for recharge area groundwater (Table 5.2).

The rate of pyrite oxidation was simulated using the rate expression developed by Williamson and Rimstidt (1994), which has been demonstrated to be reliable over a broad range of dissolved oxygen concentrations (4 orders of magnitude), and pH values (2-10), and has been used successfully in many reactive transport simulations (e.g. Appelo et al. 1998; Prommer and Stuyfzand 2005; Antoniou et al. 2013; Seibert et al. 2016). The rate expression for pyrite oxidation is:

$$R_{pyriteOX} = -k_{eff}\ \{\ H^+\}^{-0.11}\ \{O_{2\ (aq)}\}^{0.5} \quad (13)$$

where $R_{pyriteOX}$ is the overall rate of pyrite oxidation, and k_{eff} is the rate constant (mol/m^{3}s).

The reduction of ferrihydrite and pyrolusite by dissolved organic carbon (CH_2O) is assumed to occur with hydrochemical evolution in the closed system. The stoichiometry for these two reactions are:

$$Fe(OH)_3(s) + 0.25\ CH_2O + 2\ H^+ \rightarrow Fe^{2+}\ +\ 0.125\ CO_2\ +\ 2.75\ H_2O \quad (14)$$

$$MnO_2(s) + 0.5\ CH_2O\ +\ H^+ \rightarrow Mn^{+2} + 0.5\ CO_3^{-2}\ +\ H_2O \quad (15)$$

The rate expressions for the reduction of pyrolusite and ferrihydrite are represented as irreversible reactions, with an inhibition and Monod term to represent the dependence of the reaction rate on oxygen and organic carbon, respectively:

$$R_{min} = k_{eff}\ \left[\frac{m_{CH2O}}{K^M_{CH2O}+m_{CH2O}}\right]\left[\frac{K^I_{O2}}{K^I_{O2}+m_{O2}}\right] \quad (16)$$

Where R_{min} is the overall mineral oxidation rate for MnO_2 or $Fe(OH)_3$ k_{eff} is the rate constant (mol/m^{3}s), m_{CH2O} is the activity of the CH_2O (mol/L), K^M_{CH2O} is the Monod constant (mol/L) and K^I_{O2} is the inhibition term (mol/L).

The inhibition expression is included to represent the reduced reaction rate in the presence of oxygen. The Monod expression is included to slow the reaction rate when the concentrations of reacting species, in this case CH_2O, reaches a low threshold. Monod and inhibition expressions are commonly used in reactive transport simulations to represent kinetic processes and species interactions (e.g. van Cappellen and Gaillard 1996; Parkhurst and Appelo 1999; Mayer et al. 2002; Antoniou et al. 2013).

5.3.2.3 INTRA-AQUEOUS KINETIC REACTIONS

Three chemical processes are represented as intra-aqueous kinetic reactions. Ferrous iron from pyrite oxidation and dissolved organic carbon are oxidized by dissolved oxygen. With hydrochemical evolution, the reduction of sulphate by dissolved organic carbon produces hydrogen sulphide.

Dissolved organic carbon (CH_2O) is oxidized by dissolved oxygen:

$$CH_2O + O_2 \rightarrow CO_3^{-2} + 2H^+ \qquad (17)$$

with the rate defined by:

$$R_{CH_2O\ oxidation} = k_{eff}\left[\frac{m_{O2}}{K^M_{O2}+m_{O2}}\right] \quad (18)$$

where $R_{CH_2O\ oxidation}$ is the overall reaction rate for CH_2O oxidation, k_{eff} is the rate constant (mol/m^{3}s), m_{O2} is the concentration of dissolved oxygen (mol/L) and K^M_{O2} is the half-saturation constant (mol/L). For the oxidation of dissolved organic carbon, the Monod term for dissolved oxygen is equal to the half-saturation constant (van Cappellen and Gaillard 1996; Antoniou et al. 2013).

The oxidation of ferrous iron by dissolved oxygen is written as:

$$Fe^{2+} + H^+ + 0.25\ O_{2\ (aq)} \rightarrow H_2O + Fe^{3+} \quad (19).$$

$$R_{Fe^{2+}\ oxidation} = k_{eff}\left[\frac{m_{O2}}{K^M_{O2}+m_{O2}}\right] \quad (20)$$

where $R_{Fe^{2+}\ oxidation}$ is the overall reaction rate for ferrous iron oxidation by dissolved oxygen , k_{eff} is the rate constant (mol/m^{3}s), m_{O2} is the dissolved oxygen concentration (mol/L) and K_{O2}^{M} is the half-saturation constant.

With hydrochemical evolution, sulphate reduction by dissolved organic carbon is represented by individual rate expressions for sulphur isotopes ^{32}S and ^{34}S in sulphate following the approach described by Gibson et al. (2010). The reduction of DOC by sulphate is represented as:

$$CH_2O + \ 0.5\ {}^{34}SO_4^{-2} + \rightarrow\ CO_3^{2-}\ +\ 0.5\ {}^{34}HS^-\ +\ 1.5H^+ \quad (21)$$

$$CH_2O + \ 0.5\ {}^{32}SO_4^{-2} + \rightarrow\ CO_3^{2-}\ +\ 0.5\ {}^{32}HS^-\ +\ 1.5H^+ \quad (22)$$

The rate expressions for the reduction of sulphate by DOC are written as:

$$R_{34_{SO4}\ reduction} = {}^{34}k \left[\frac{m_{Ch2O}}{K_{CH2O}^{M}+m_{CH2O}}\right]\left[\frac{m_{34_{SO4}}}{K_{34_{SO4}}^{M}+m_{34_{SO4}}}\right]\left[\frac{K_{O2}^{I}}{K_{O2}^{I}+m_{O2}}\right] \quad (23)$$

$$R_{32_{SO4}\ reduction} = {}^{32}k \left[\frac{m_{Ch2O}}{K_{CH2O}^{M}+m_{CH2O}}\right]\left[\frac{m_{32_{SO4}}}{K_{32_{SO4}}^{M}+m_{32_{SO4}}}\right]\left[\frac{K_{O2}^{I}}{K_{O2}^{I}+m_{O2}}\right] \quad (24)$$

Where $R_{34_{SO4}\ reduction}$ and $R_{32_{SO4}\ reduction}$ are the overall reaction rates for the two sulphur isotopes of sulphate, ^{32}k and ^{34}k are the rate constants for the reactions (mol/m^{3}s), m_{Ch2O} and K_{CH2O}^{M} are the activity and Monod constant for CH_2O, respectively (both mol/L), $m_{34_{SO4}}$ and $K_{34_{SO4}}^{M}$ are the activity and Monod constant for sulphate-34, respectively (both mol/L) and K_{O2}^{I} and m_{O2} are the half-saturation constant and dissolved oxygen concentration (both mol/L) in the inhibition term, respectively. The inhibition expression has been included in the rate expressions (equations 23, 24) to represent the reduced reaction rate in the presence of oxygen. Monod expressions have also been included to slow the reaction rates when the concentrations of reacting species, CH_2O and sulphate, reach low thresholds.

The mass dependant rate constants for the two sulphur isotopes (^{32}k and ^{34}k) were estimated following the method of Gibson (2010), using equations 10 and 11, above. A sulphur isotope fractionation factor (α) of 0.959 was applied. This fractionation factor was estimated by taking the fractionation factor of Sakai (1968) and performing a temperature correction (Majoube 1971) to account for the influence of the study area groundwater temperatures (ave = 9 °C). The value for $^{34}R_S$, represents the isotope ratio of sulphur in the gypsum mineral (0.0443965).

5.4 MODEL PARAMETERIZATION

Calibrated values of porosity and hydraulic conductivity are 0.005 and $9x10^{-5}$ m s^{-1}, respectively, which are within the porosity range reported for the Guelph Fm (Zheng, 1999; range = 0.001 to 23.6 %) and within the range of hydraulic conductivity values reported for the Guelph Fm ($3x10^{-4}$ to $9x10^{-6}$ m/s; Priebe et al. 2017a). The calibration of porosity and hydraulic conductivity was conducted to simulate a target groundwater velocity of 1 km/year, which was estimated from tritium values. The observed concentration of tritium at recharge is approximately 12 TU, with non-detect tritium observed at 50 km from the recharge area (detection limit is 0.8 TU). With a half-life of 12.32 years, groundwater with an input tritium concentration of 12 TU would decay to 0.8 TU in 48 years in a closed system, approximating an average linear groundwater velocity of 1km/year. This velocity value falls within the possible range of groundwater velocities of 100 m/year to 4 km/year, as estimated from Guelph FM K values (Priebe et al. 2017), the range of local porosities (Zheng 1999) and the horizontal gradient for the Guelph FM hydrostratigraphic unit (0.004, see section 4.3)

Mineral volume fractions were constrained by the geochemistry data of Rowell (2015; Table 5.4) with the exception of sulphur minerals, pyrite and gypsum. Calibrated sulphur mineral percentages are higher than the whole rock sulphur quantities of Rowell (2015) in part to reflect the percentage of the entire mineral in the model rather than just elemental sulphur. However, proportions of pyrite and gypsum in the calibrated model are higher (pyrite 3x and gypsum 6x) than the whole rock sulphur values would suggest. Higher values are intended to account for the spatial inconsistency in these minerals not captured by the work of Rowell (2015). The isotopic composition of strontium in the dolomite mineral was constrained by the average value of the bedrock isotopic analyses (equation 5, Chapter 4 Figure 4.7A). Hydrochemistry and isotopic compositions of groundwater at the recharge boundary was constrained by sample analyses for DDH6-2 and initial conditions within the model domain were constrained by the median values for the evolved end member (Table 5.2).

Table 5.4. Whole rock geochemistry data for the Guelph Fm HSU (Rowell 2015)

Whole rock geochemistry data				**Calibrated mineral proportions**	
Mineral/parameter	**Average (*n = 124*)**	**Min**	**Max**	**%**	**Assumed mineral assemblage**
Carb Tot (%)	98.53	87.81	101.01	96.4	dolomite
Ca:Mg	1.42	1.32	2.04	2.04	
S (%)	0.01	<0.01	0.01	0.5	pyrite
				2.5	gypsum
Sr (%) (*n = 51*)	0.0057	0.0043	0.0095	0.0043	Sr, in dolomite structure
Iron oxide %	0.12	0.0	0.41	0.1	ferrihydrite
Manganese oxide (%)	0.02	0.01	0.06	0.05	Manganese dioxide

Calibrated and fixed parameters for the kinetic rate expressions are presented in Table 5. Effective rate constants were calibrated manually, with the exception of the values representing the dolomite reaction pathways which were taken from Busenberg and Plummer (1982). Equilibrium constants for the precipitation and dilution of gypsum, magnesite, calcite, ferrihydrite and pyrolusite were taken from the PHREEQC databases minteq.v4.dat, minteq.dat or phreeqc.dat (Parkhurst and Appelo 1999; Table 5.5). Inhibition and Monod terms governing the role of dissolved oxygen in chemical processes were taken from the literature (Shafer 2001; Parkhurst and Appelo 1999; van Cappellen and Gaillard 1996), with the exception of the inhibition constant for sulphate reduction in the presence of oxygen, which was calibrated. Inhibition and Monod terms for all other processes were calibrated (Table 5.5).

Table 5.5. Calibrated and fixed parameters. Parameters without references were calibrated.

Reaction	Eqn	Parameter	Value	Units	Source
Mineral precipitation/dissolution reactions					
Dolomite	2-4	log k1, log k2, log k3	-7.55, -9.18, -11.5	mol/m^2	Busenberg and Plummer 1982
		Surface area	0.065	m^{2}mineral/ L bulk	Chilingarian et al. 1990
		φ	0.964	m^{3}mineral/m^3 bulk	Rowell (2015)
Gypsum	8,9	log K	- 4.58	mol/L	Parkhurst and Appelo 1999 (phreecq.dat)
		log ^{34}k	-16.01	mol/m^{3}s	
		log ^{32}k	-14.67	mol/m^{3}s	
		φ	0.025	m^{3}mineral/m^3 bulk	Rowell (2015)
Ferrihydrite	14	log K	4.891	mol/L	Parkhurst and Appelo 1999 (minteq.dat)
		log k_{eff}	-10.5	mol/m^{3}s	
		φ	0.001	m^{3}mineral/m^3 bulk	Rowell (2015)
Magnesite	15	log K,	- 8.8	mol/L	Parkhurst and Appelo 1999 (minteq.v4.dat)
		log k_{eff}	-9.0	mol/m^{3}s	
		φ	mineral not identified		Brunton et al. 2007
Calcite		log K,	- 8.48	mol/L	Parkhurst and Appelo 1999 (phreecq.dat)
		log k_{eff}	-12.05	mol/m^{3}s	
		φ	mineral not identified		Brunton et al. 2007
Redox reactions					
Pyrolusite reduction by DOC	13	log k_{eff}	-14.5	mol/m^{3}s	
		φ	0.005	m^{3}mineral/m^3 bulk	Rowell (2015)
Ferrihydrite reduction by DOC	16	log k_{eff}	-15.1	mol/m^{3}s	
		φ	0.001	m^{3}mineral/m^3 bulk	Rowell (2015)
		log K^M_{CH2O}	-5, -10	mol/L	
		log K^I_{O2}	-5.5	mol/L	Shafer (2001)
MnO reduction by DOC	16	log k_{eff}	-17.7	mol/m^{3}s	
		φ	0.0005	m^{3}mineral/m^3 bulk	Rowell (2015)
		log K^M_{CH2O}	-5, -10	mol/L	

Reaction	Eqn	Parameter	Value	Units	Source
		$\log K^{I}_{O2}$	-5.5	mol/L	Shafer (2001)
Intra-aqueous kinetic reactions					
Sulphate reduction by DOC and S isotope fractionation	23, 24	$\log {}^{34}k$	-15.727	mol/m^3s	
		$\log {}^{32}k$	-13.369	mol/m^3s	
		$\log K^{M}_{CH2O}$, $\log K^{M}_{34_{SO4}}$ $\log K^{M}_{32_{SO4}}$	-5, -10, -10		
		$\log K^{I}_{O2}$	-8.0	mol/L	
Ferrous iron oxidation	20	$\log k_{eff}$	-11	mol/m^3s	
		$\log K^{M}_{O2}$	-3.5	mol/L	Parkhurst and Appelo 1999; van Cappellen and Gaillard 1996
DOC oxidation by oxygen	18	$\log k_{eff}$	-14	mol/m^3s	
		$\log K^{M}_{O2}$	-3.5	mol/L	Parkhurst and Appelo 1999; van Cappellen and Gaillard 1996

5.5 RESULTS AND DISCUSSION

5.5.1 Model Simulations of Field Observations Presented Spatially

Simulation results are compared to field observations along a hypothetical 50 km flow path in the Guelph HSU, located in the southern half of the study area (Figure 5.2). To facilitate these comparisons, field observations were transposed along this hypothetical groundwater flow path. Based on the conceptual model presented in Chapter 4, Figure 4.9, recharge for the southern part of the study area is assumed to occur at the groundwater divide in the centre of the study area, representing the starting point of the hypothetical flowpath, with conditions becoming closed to the atmosphere downgradient. The simulated flowpath is described as hypothetical because the sampling points are not directly downgradient of each other, nor are they directly downgradient of a single recharge area. In fact, the monitoring wells and their sampling points were installed long before the complexity of the flowpaths was appreciated, consequently the simulated flowpath is an approximation of the ensemble of actual flowpaths. Though outliers exist, trends in the field observations along the hypothetical flowpath are evident enough that the exercise of simulating them is instructive. Simulation results are not intended to perfectly match every field observation, but rather they are intended to reflect general trends in hydrochemistry and isotopes with increasing groundwater residence time. The symbols representing field data are sized to reflect tritium content, with the largest symbols reflecting the most recently recharged water and smallest representing the longest residence times (Figures 5.3-5.5). The tritium content, and associated field data symbol sizes,

decrease within the first 20 km and then slightly increase along the hypothetical flowpath. This observation in the field data indicates discontinuity and/or mixing.

5.5.1.1 MINERAL PRECIPITATION/DILUTION

5.5.1.1.1 Dolomite Dissolution

The simulated dissolved Ca concentration is 66 mg/L at the recharge boundary, falling rapidly in the first few kilometres of the flowpath to 45 mg/L and then rising along the rest of the flowpath to 61 mg/L (Figure 5.3A). The field data show a similar trend of decreasing Ca followed by an increase, though the initial drop in the field values is slower and more pronounced than the simulation indicates. In general, the simulated Ca values fall within the range of observations, and the trend direction, of initial drop and subsequent rise with an overall net decrease, appear to be similar. The areas of disagreement between simulated and observed are the timing and magnitude of the Ca concentration drop. The sources of dissolved Ca in the model are the dissolution of dolomite (equations 1-4) and the dissolution of gypsum (equations 8 and 9). With no calcite in the bedrock itself, the conceptual model assumes that calcite precipitation occurs as dolomite and gypsum dissolve. The net reduction of Ca in the simulation and the field observations, despite the addition of Ca from gypsum dolomite dissolution, indicates that the conceptual model is likely correct. Calcite precipitation and dissolution was initially governed thermodynamically in the model, but was subsequently kinetically controlled to improve the simulation of dissolved Ca. The rate constant for calcite precipitation/dissolution is calibrated here, an approach that is justified by the broad range of rate constants developed empirically by others (Nancollas and Reddy 1971; Plummer et al. 1978; Plummer and Wigley 1976; Inskeep and Bloom 1985; Chou et al. 1989).

For dissolved Mg, the simulation shows the concentration rising rapidly at the recharge boundary, with values increasing from 28 to 45 mg/L in the first few kilometers of the flowpath (Figure 5.3B). The rate of change of dissolved Mg slows after this rapid initial rise, with concentrations increasing steadily to 60 mg/L at the end of the flowpath. The simulation does not reproduce the field observation well in either trend direction or magnitude. The field observations suggest that the Mg trend is similar to that observed for Ca, with an initial decrease near the recharge boundary, followed by a slow increase along the flowpath. The poor representation of dissolved Mg by the model, particularly at the recharge boundary where the simulation differs in trend direction, likely reflects a misrepresentation of Mg mineralogy in the simulation. The potential mineral sink for dissolved Mg in the model comprises magnesite, which was governed by thermodynamic constraints in the model. Although magnesite was reactive in the model, it was not reactive enough to represent the Mg sink that would be required to better match the field

observations. Earlier versions of the model included the precipitation and dissolution of additional minerals brucite ($Mg(OH)_2$) and nesquenhonite ($MgCO_3*3H_2O$), but these minerals did not dissolve or precipitate. The lack of brucite reactivity was likely due to pH, as brucite precipitates readily at a pH of 10 or above (Sillen and Martell 1964) and the average field area pH is 7.4. Hostetler (1964) described nesquehonite as requiring a high level of super-saturation before precipitation can occur, which was not achieved in the model. Further exploration of the controls on magnesium in the conceptual model is required.

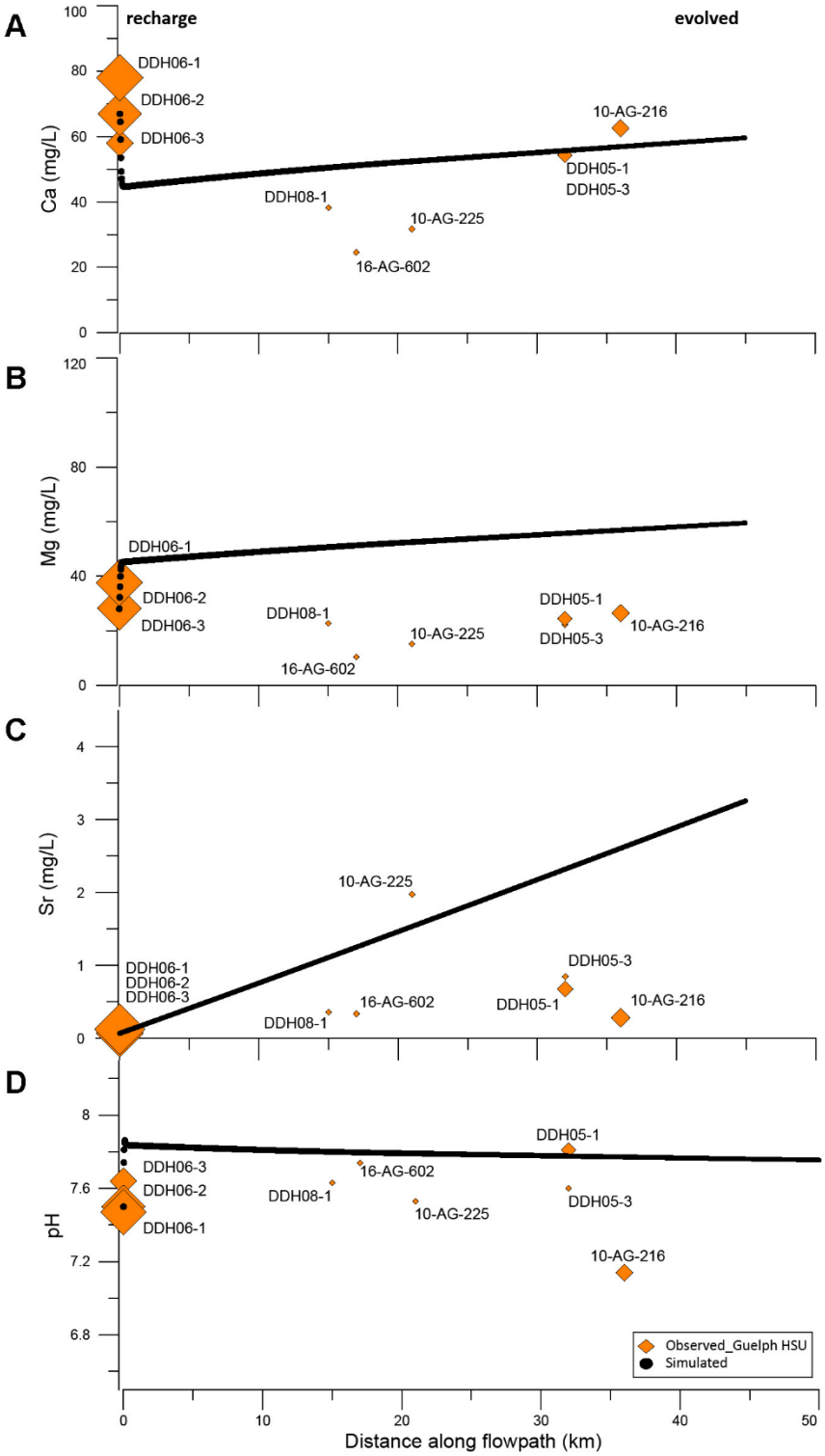

Figure 5.3. Simulated and observed values of cations Ca (panel A), Mg (panel B), Sr (panel C), as well as pH (panel D) are shown along the groundwater flowpath from recharge (0 km) on the far left, to hydrochemically evolved (50 km) on the far right. Observed values are symbolized with orange diamonds and are sized to reflect tritium content. Simulated concentrations are symbolized with black dots that where tightly spaced, resemble a black line.

Simulated Sr concentrations increase from 0.07 at the recharge boundary to 3.5 mg/L at the end of the flowpath (Figure 5.3C). The simulated Sr values approximate the field observations well in trend direction, though the concentrations are slightly over-predicted. The conceptual model describes Sr as increasing with groundwater residence time, a trend observed with the simulation and the field observations (Figure 5.3C). This slight over-prediction of concentrations is likely due to a misrepresentation of the proportion of Sr in the dolomite mineral (equations 2-4). During calibration, the Sr proportion was varied within the range of values reported by Rowell (0.0057-0.0043%, 2015) with the final calibrated value representing the minimum of this range (Table 5.4). It is possible that the whole rock analyses (Rowell 2015) do not capture the full range of Sr content in the dolomite mineral across the study area.

Because dolomite is the only source of Sr in the model, the relatively good agreement between simulated and observed values suggests that the process of irreversible dolomite dissolution has been well represented by the imposed reaction pathways (equations 2-4), with rate constants for these taken from Busenberg and Plummer (1982). Because H^+ is a component of the first dolomite dissolution reaction pathway (equation 2), the good approximation of the narrow range of field pH values (7.5 to 7.8) with the model (Figure 5.3D) provides further indication that dolomite dissolution has been well represented.

Simulated pH and dissolved Mg and Ca values show rapid changes within the first few kilometres of the recharge boundary (Figure 5.2 A, B and D). These rapid changes are likely caused by equilibration of recharge boundary water with the mineral assemblage in the model. A smoother recharge input simulation for Ca, Mg and pH could likely be achieved by setting the mineral assemblage to reflect the DDH6-2 location specific bedrock mineralogy and whole rock geochemistry, should these data become available. A further addition to the model that may improve the simulation at the beginning of the flowpath would be the addition of pCO_2. Although pCO_2 data were collected, quality control issues prevented their inclusion here.

5.5.1.1.2 Gypsum Precipitation and Dissolution

The simulated dissolved sulphate concentration is 14 mg/L at the recharge boundary, rising to 70 mg/L at the end of the flowpath (Figure 5.4A). The field observations and simulated values show the same trend of increasing sulphate concentrations along the flowpath, though the simulation provides a slight overprediction of sulphate concentrations. This increase in sulphate concentration corresponds with the trend of increasing gypsum SI that is observed in the field data and the simulation (Figure 5.4B). The

simulated and observed increase in sulphate and gypsum SI with groundwater residence time reflects the conceptual model presented in Chapter 4, Figure 4.8B.

The effective rate constant for gypsum precipitation and dissolution (equations 8, 9) was calibrated to approximate dissolved sulphate concentrations along the flowpath. This approach represents kinetically limited gypsum dissolution which is justified as a means of accounting for the spatially inconsistent distribution of gypsum along the flowpath, the source of which is the (presently eroded) Salina Group evaporitic bedrock formations (Armstrong and Carter 2010).

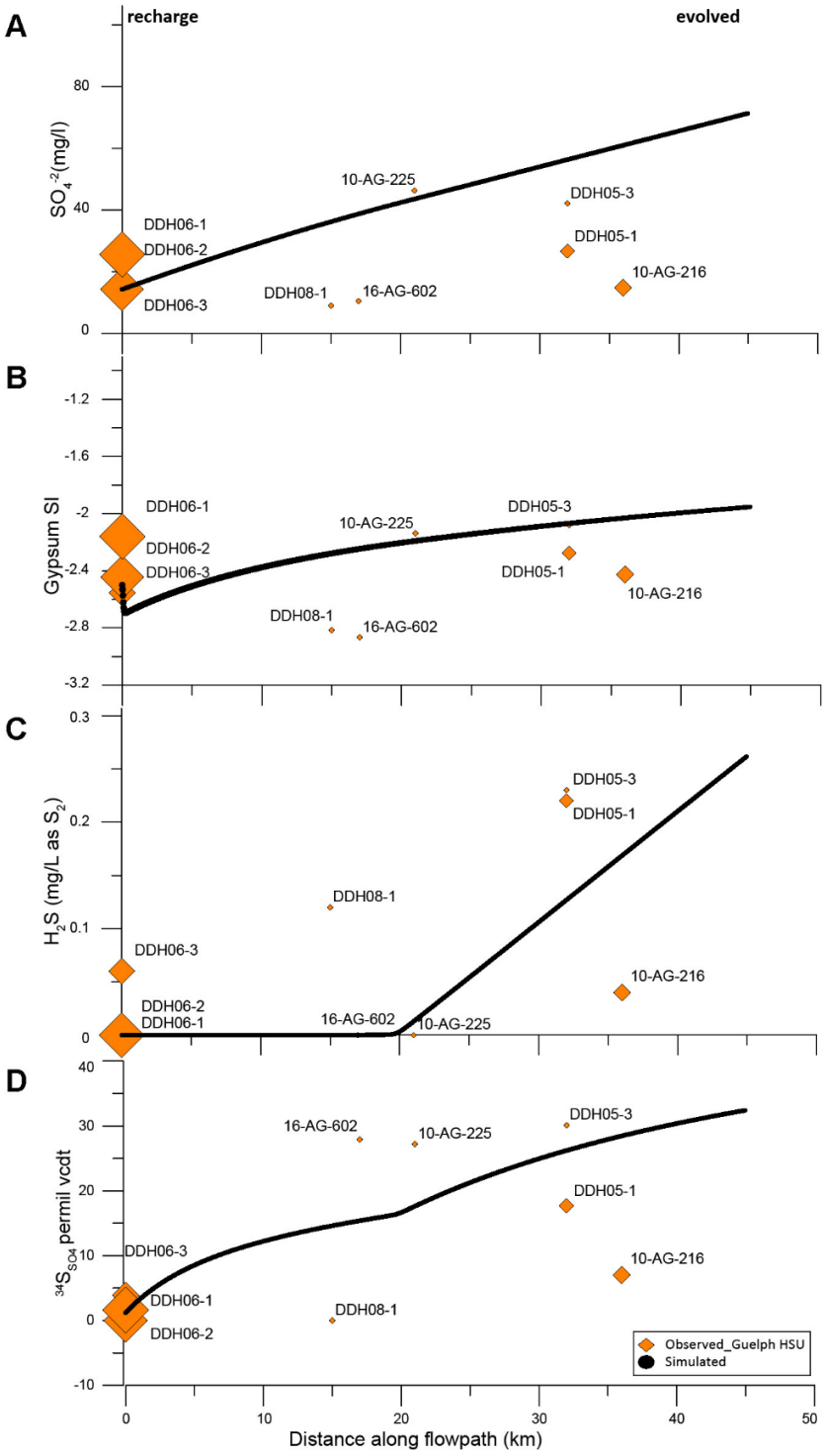

Figure 5.4. Simulated and observed values of dissolved sulphate (panel A), gypsum saturation index (panel B), H2S (mg/L) and the ^{34}S of sulphate are shown along the groundwater flowpath from recharge (0 km) to hydrochemically evolved (50 km) on the far right. Observed values are symbolized with orange diamonds and are sized to reflect tritium content. Simulated concentrations are symbolized with black dots that, where tightly spaced, resemble a black line.

Simulated dissolved H_2S concentrations rise at approximately 22 km into the flowpath, corresponding to the point just beyond where field observations show non-detectable values (Figure 5.4C). The simulated rise in dissolved H_2S reflects the rise observed in field data, though the field data show varied concentrations (Figure 5.4C). The varied concentrations are likely related to spatial inconstancy of the gypsum mineral and associated dissolved sulphate. Fractionation of sulphur isotopes during H_2S production from sulphate reduction (equations 21, 22), causes the hinge-point in the curve and the simulated increasing enrichment rate of $\delta^{34}S_{SO4}$ (Figure 5.4D). Although the simulation reflects the conceptual model well, the field observations do not show this trend clearly. However, the field data do show a progressive enrichment of $\delta^{34}S_{SO4}$ along the flowpath, which is well simulated with the model.

5.5.1.2 REDOX PARAMETERS

The simulated dissolved oxygen concentration is 2.5 mg/L at the recharge boundary, decreasing to 0 mg/L within the first 20 km of the flowpath (Figure 5.5A). Simulated dissolved manganese, iron and hydrogen sulphide concentrations are below detection at the recharge boundary, increasing along the flowpath to 0.04 mg/L, 0.8 mg/L and 0.3 mg/L, respectively (Figure 5.5, panels B, C and D). The simulation shows that manganese concentrations are below detection until they begin rising at approximately 15 km into the flowpath, with dissolved iron and hydrogen sulphide concentrations beginning to increase at approximately 18 and 22 km, respectively. In general, the simulation approximates the trends in observed redox parameter concentrations well in direction and magnitude along the flowpath.

Many redox processes involving dissolved CH_2O, either as an oxidant or reductant, are included in the conceptual and reactive transport models. These CH_2O consuming processes comprise CH_2O oxidation (equation 17), ferrihydrite and pyrolusite reduction (equations 14,15) and sulphate reduction (equations 21,22). Observed CH_2O values appear to be increasing along the flowpath (Figure 5.5E), though the controls on this apparent trend are not well understood due to a lack of characterization of the source, which is assumed to be the underlying, petroliferous Eramosa Formation. Because of this uncertainty, CH_2O was simulated as being consistently present at the average value (4.0 mg/L) throughout the model. Rate constants for processes that include the consumption of CH_2O were calibrated, in part, by ensuring that CH_2O values were maintained within the range of observed values (Figure 5.5E).

The spatial trends in simulated and observed concentrations of redox parameters DO, Mn, Fe and H_2S are consistent with oxidation-reduction sequences commonly described for closed oxidant systems (e.g. Champ et al. 1979; Edmunds and Walton 1983). This consistency among commonly described, observed

and modelled trends provides strong evidence supporting the conceptual model of redox processes in the study area, and the accuracy of how these processes are represented in the model. In addition, these results provide further evidence that the assumption of closed oxidant system conditions is realistic.

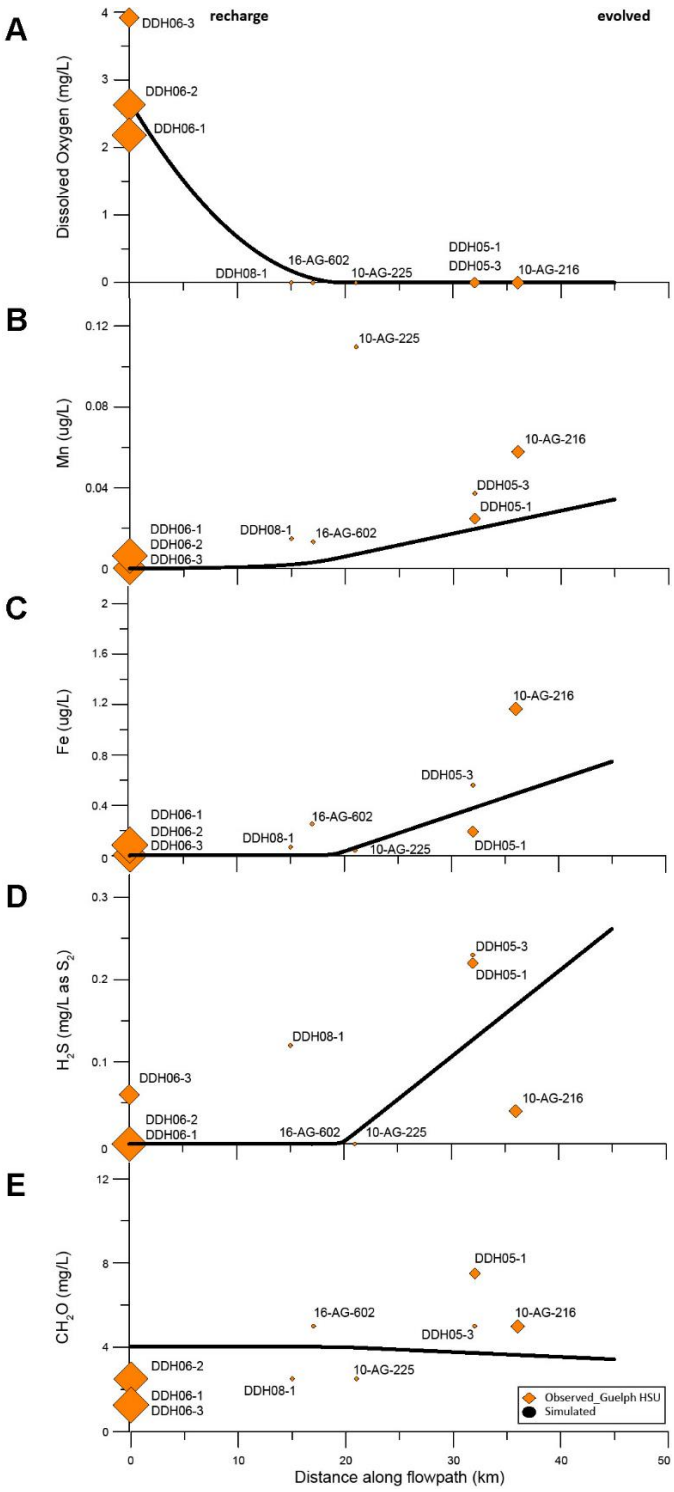

Figure 5.5. Simulated and observed values of dissolved oxygen (panel A), manganese (panel B), iron (panel C) and hydrogen sulphide (panel D) are shown along the groundwater flowpath from recharge (0 km) to hydrochemically evolved (50 km) on the far right. Observed concentrations are symbolized with *orange diamonds* and are sized to reflect tritium content. Simulated concentrations are symbolized with *black* dots that resemble a black line where tightly spaced.

5.5.2 Results by Chemical Process

In the following comparisons, simulation results are plotted against field observations to assess the individual chemical and isotopic processes that were used as evidence towards developing the conceptual model described in Chapter 4. The model was built to simulate Guelph HSU processes, however, the Goat Island field data are included here because of similarities in hydrochemical trends between the two units. The inclusion of hydrochemical data from the Goat Island HSU enables an assessment of the suitability of applying a similar modeling approach in this unit. Observed tritium data were used in the following plots to guide the point of comparison, with the simulated recharge boundary values plotted against the observed highest tritium values.

5.5.2.1 Carbonate System with Strontium Isotopes

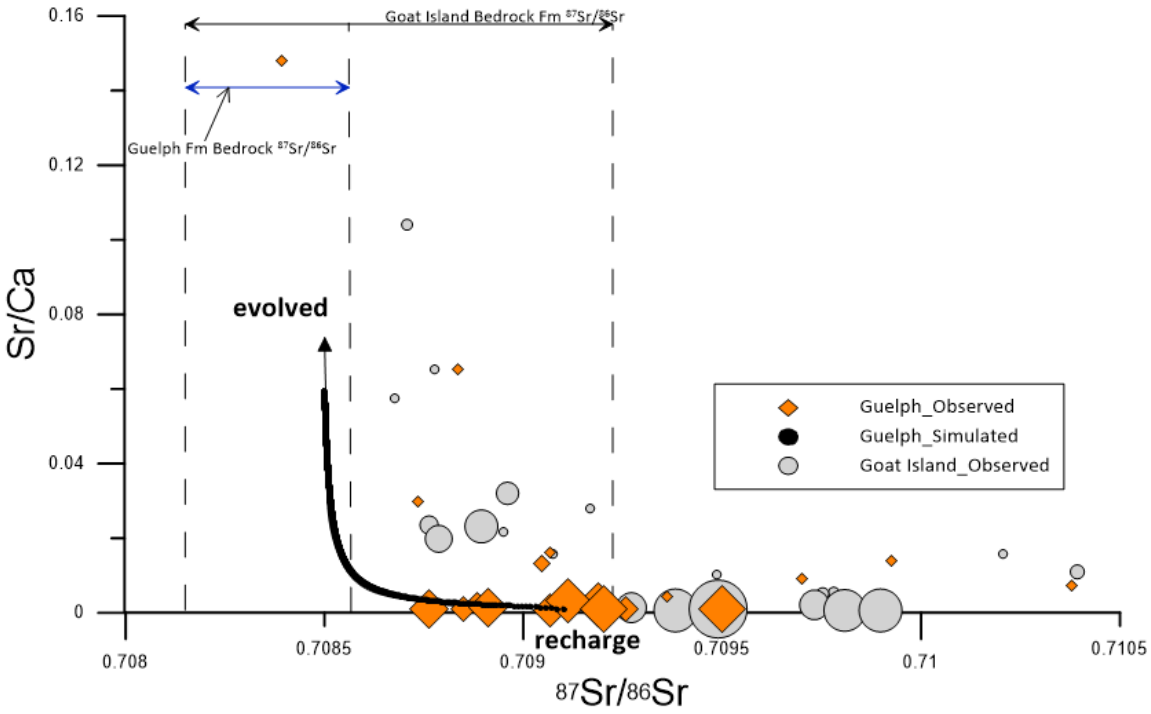

Figure 5.6. The groundwater strontium isotope ratio ($^{87}Sr/^{87}Sr$) is shown versus the Sr/Ca ratio for the Guelph and Goat Island HSUs. Guelph HSU groundwater samples are symbolized with *orange diamonds*, scaled to reflect tritium content. Goat Island HSU groundwater samples are symbolized with *grey circles*, also sized to reflect tritium content. Modelled concentrations are symbolized with *black dots* that resemble a black line where tightly spaced. The *vertical dashed lines* represent whole rock $^{87}Sr/^{87}Sr$ ranges for the Guelph Formation and the Goat Island Formation bedrock.

The simulation shows an increase in the Sr/Ca ratio and a corresponding decrease in the $^{87}Sr/^{86}Sr$ isotope ratio as groundwater residence time increases (Figure 5.6). For the evolved Sr/Ca values, there is

generally good agreement between the simulated and observed values, with the exception of a high Guelph HSU Sr/Ca outlier (0.15) that was not reached with the simulation. For the strontium isotopic composition, the simulated $^{87}Sr/^{86}Sr$ values match the field observations reasonably well in trend direction but the model gives more radiogenic values with hydrochemical evolution than are observed. The model was designed to simulate a progression from 0.7090 at recharge, decreasing to the average $^{87}Sr/^{86}Sr$ isotope ratio of the Guelph Fm bedrock with increasing residence time (average = 0.7085, values plotted Chapter 4, Figure 4.7A). The poor agreement between observed and simulated $^{87}Sr/^{86}Sr$ may be because the targeted Guelph Fm bedrock average $^{87}Sr/^{86}Sr$, developed from a single bedrock core, does not reflect the true range or spatial variability in the strontium isotopic composition of the Guelph Fm bedrock.

Despite the generally good agreement in trend direction for both parameters, there are some anomalies in the field observations that suggest that the conceptual and reactive transport models may not entirely represent strontium dynamics in the system. There are several evolved Guelph HSU field observations with long residence times (small symbols) that do not follow the general trend of increasing Sr/Ca and decreasing $^{87}Sr/^{86}Sr$ with evolution. Despite their long residence times, these samples show low Sr/Ca ratios and $^{87}Sr/^{86}Sr$ values that are much more radiogenic than the Guelph or Goat Island bedrock $^{87}Sr/^{86}Sr$ range of values. These anomalies indicate that although the conceptual and reactive transport models represent the general trends well, they do not account for strontium dynamics with groundwater hydrochemical evolution for every flowpath in the Guelph HSU. Similar trends and anomalies are observed for the Goat Island HSU, indicating that the same modeling approach may be applied for this unit with consideration that the conceptual and reactive transport model are not reflective of chemical changes within every flowpath.

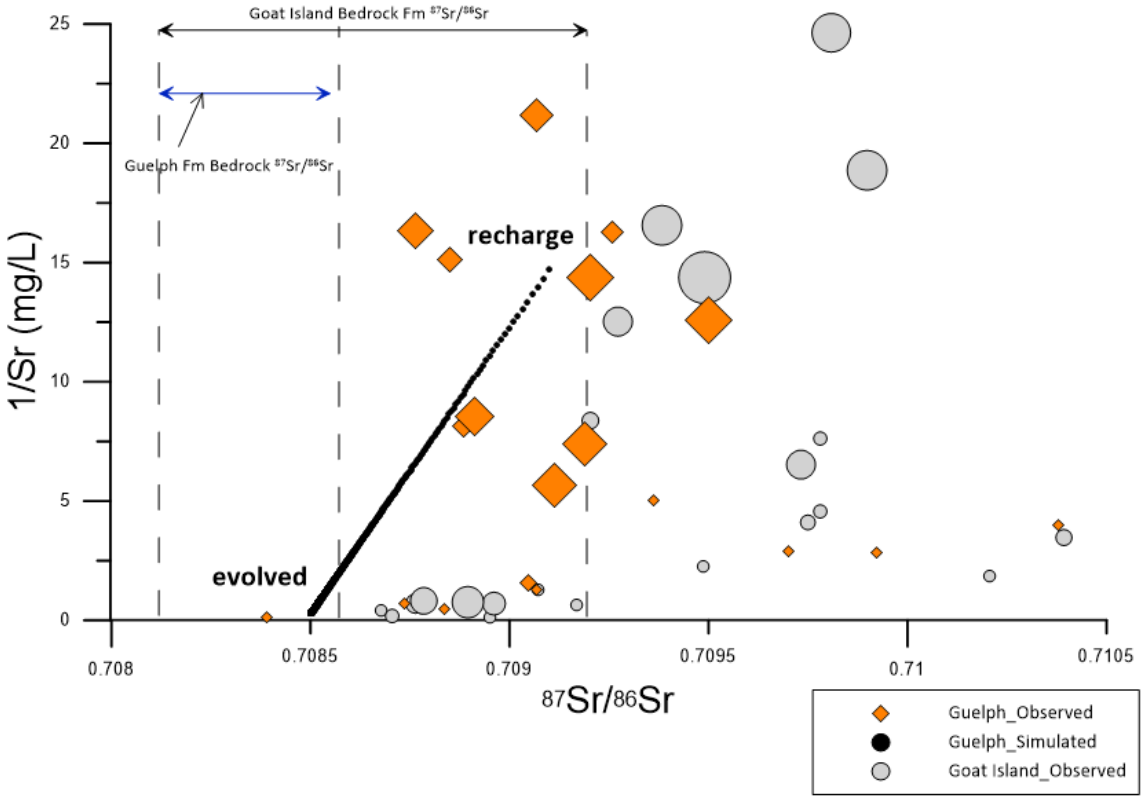

Figure 5.7. The strontium isotope ratio ($^{87}Sr/^{87}Sr$) is shown versus the inverse of dissolved Sr for groundwater samples from the Guelph and Goat Island HSUs. Guelph HSU groundwater samples are symbolized with *orange diamonds*, scaled to reflect tritium content. Goat Island HSU groundwater samples are symbolized with *grey circles*, also sized to reflect tritium content. The simulation results are symbolized with the *black dots* that resemble a black line where tightly spaced.

The simulation of total Sr against $^{87}Sr/^{86}Sr$ shows a trend of increasing Sr with a corresponding decrease in the $^{87}Sr/^{86}Sr$ isotopic composition with groundwater residence time (Figure 5.7). There is good agreement between the simulated and observed total Sr values in magnitude and trend direction. The simulated $^{87}Sr/^{87}Sr$ values, also shown in Figure 5.6, show the same progression towards the average value for the Guelph Fm bedrock. As a result, the model does not simulate the field observations well due to the wide range of observed $^{87}Sr/^{87}Sr$ values. Considering total Sr and $^{87}Sr/^{87}Sr$ together, the observed values show that total Sr consistently increases with groundwater residence time regardless of the $^{87}Sr/^{87}Sr$ value.

While the trend of increasing total Sr with residence time is consistent (Figure 5.7), the increase in Sr/Ca with groundwater residence time is not consistent (Figure 5.6). The increase in total Sr with residence time suggests continued dolomite dissolution with hydrochemical evolution, which reflects the conceptual model. However, variability in the Sr/Ca ratio for the most evolved samples indicates that the continuous dissolution of dolomite and resulting calcite precipitation, described in the conceptual model, is not

occurring everywhere within the Guelph HSU as predicted or simulated. Samples with long residence times and low Sr/Ca ratios may occur where the dolomite contains little to no strontium in the mineral structure. Trends and anomalies observed for the Guelph HSU are similar to those observed for the Goat Island HSU, indicating that the same modeling approach, with consideration of inconsistencies, may be employed for this unit.

5.5.2.2 SULPHUR

The simulation shows an increase in the saturation index for gypsum along the flowpath, from as low as -2.7 at recharge to -2.0, corresponding with an enrichment of $\delta^{34}S_{SO4}$ from 2.5 permil at recharge to 32 permil VCDT. Simulated and observed values show the same trend of increasing gypsum SI and progressive enrichment of $\partial^{34}S_{SO4.}$ The only area of disagreement between simulated and observed values appears to be with gypsum SI at the recharge boundary. Although the simulation provides a perfect match with initial gypsum SI values, simulated values quickly drop and subsequently climb to provide a good match with field observation with evolution. The early drop in gypsum SI is likely caused by the drop in Ca concentration that is also observed at the recharge boundary (Figure 5.3A). As mentioned in regard to Figure 5.3A, rapid changes in chemistry at the recharge boundary are likely caused by initial disequilibrium of recharge boundary water with the mineral assemblage in the model, resulting from the use of average mineral values rather than site-specific ones.

Along the flowpath, the $\delta^{34}S_{SO4}$ signature becomes more enriched as Silurian gypsum dissolves and sulphate reduces to H_2S by dissolved organic carbon (equations 21, 22). The reduction of sulphate to H_2S by dissolved organic carbon results in an enrichment in the remaining dissolved sulphate, and the initiation of this process is marked by the hinge-point in the curve, observed at $\delta^{34}S_{SO4}$ = 17 permil VCDT (Figure 5.8, Figure 5.4C and 5.4D). The enrichment of $\delta^{34}S_{SO4}$ with sulphate reduction is governed by the sulphur isotope mass dependant rate constants (equations 23, 24; Table 5.5). The effective rate constants for gypsum dissolution and sulphate reduction were calibrated to best simulate dissolved sulphate and hydrogen sulphide concentrations.

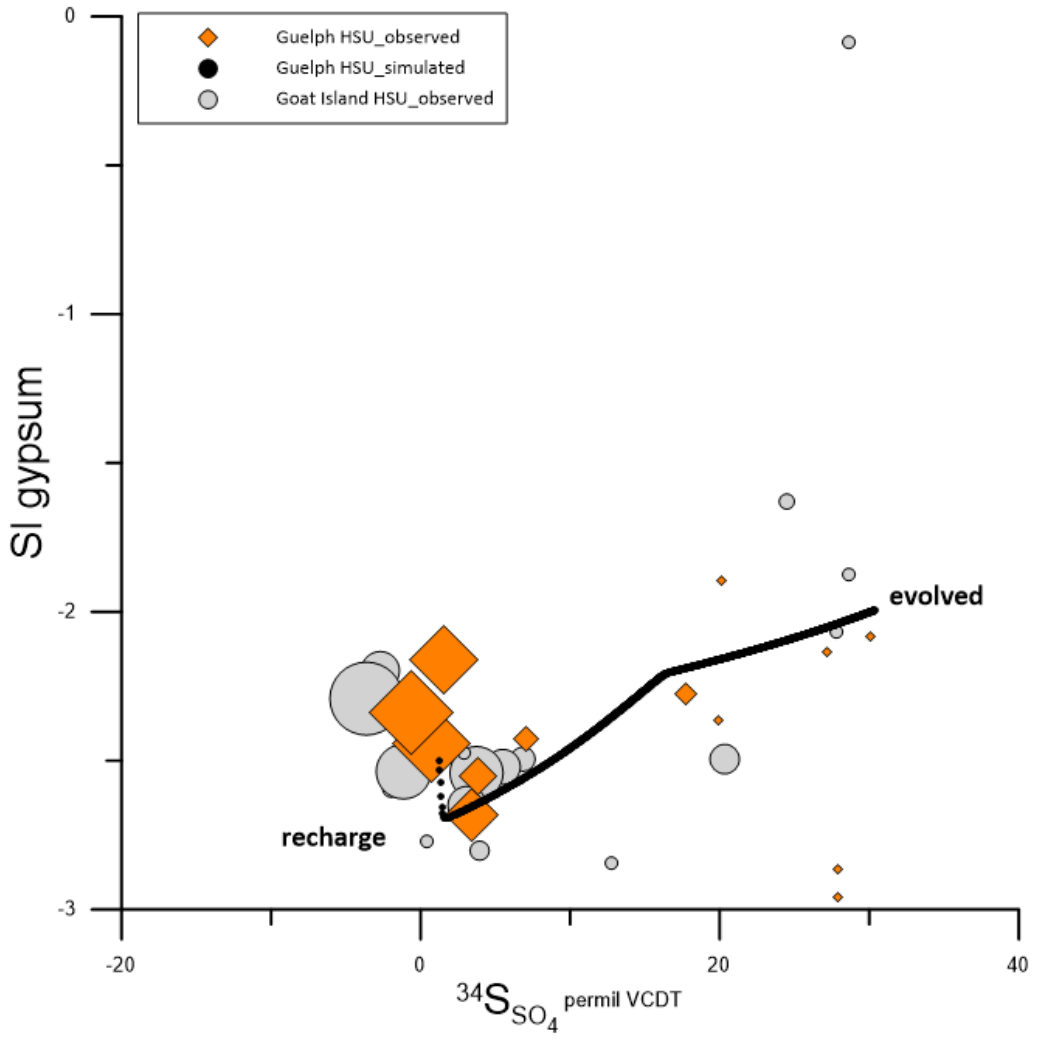

Figure 5.8. The $\delta^{34}S_{SO4}$ is presented against the saturation index for gypsum for the Guelph and Goat Island HSU groundwater datasets. Guelph HSU groundwater samples are symbolized with *orange diamonds*, scaled to reflect tritium content. Goat Island HSU groundwater samples are symbolized with *grey circles*, also sized to reflect tritium content. The simulation results are symbolized with the *black dots* that resemble a black line where tightly spaced.

With the exception of two evolved samples with low SI values, there is good agreement between observed and simulated gypsum SI and $\delta^{34}S_{SO4}$ for the Guelph HSU dataset. This good agreement indicates that pyrite oxidation, gypsum dissolution and precipitation and sulphur isotope fractionation during sulphate reduction have been accurately represented in the conceptual and reactive transport models. At recharge, the simulated $\delta^{34}S_{SO4}$ values fall within the range of expected of pyrite oxidation (Claypool et al. 1980), indicating that pyrite oxidation is the dominant sulphate producing process in the recharge areas. The evolved end member $\delta^{34}S_{SO4}$ values reflect the Silurian isotope signature (Toran and Harris 1989), indicating that gypsum dissolution and sulphate reduction are the dominant processes with increasing groundwater residence time.

The successful simulation of sulphur processes in the Guelph HSU indicates that this modeling approach could reasonably be applied to simulate the same processes elsewhere. For example, field data for the Goat Island HSU follow similar trends in gypsum SI and the $\delta^{34}S_{SO4}$ isotopic composition to the Guelph HSU (Figure 5.8). These similarities indicate that the modeling approach developed here may also be suitable for simulating these processes in the Goat Island HSU (Figure 5.8).

5.6 CONCLUSIONS

Reactive transport modeling was conducted to simulate isotopic and hydrochemical changes along a hypothetical 50 km flowpath, from recharge to closed-system evolution, in a carbonate bedrock aquifer system. The objective of this modeling exercise was to provide a quantitative assessment of the hydrochemical and isotopic processes that form the conceptual model presented in Chapter 4. Disagreement between simulated and observed values was intended to provide insight into possible flaws in the conceptual model.

Magnesium was the only parameter for which the model results gave a very poor approximation of the field data in both concentration levels and general trend direction. Because calcium, strontium and pH were simulated reasonably well, the poor approximation of magnesium is not likely attributed to how the reaction kinetics of the dolomite mineral were included in the model. Rather, the poor agreement is likely due to misrepresentation of magnesium-bearing mineralogy. Future modeling will require further investigation into magnesium dynamics and mineralogy within the system. With the exception of magnesium, the model approximates field observations reasonably well in magnitude and very well in trend direction. The results indicate that the conceptual model presented in Chapter 4 is comprehensive and realistic, however inconsistencies and outliers in the field data confirm that the conceptual model cannot be ubiquitously applied.

Model calibration was done manually, without the commonly applied statistical improvements of fit and sensitivity analyses. This approach provided the appropriate level of scrutiny, given that there is inconsistency in the field trends themselves, and further calibration methods or sensitivity analyses would have provided a misleading level of rigour. This calibration approach is consistent with the model objective, which was to quantify and assess the major processes. The reliability of the model lies in its field data constraints comprising whole rock geochemistry and mineralogical data (Rowell 2015; Brunton et al. 2007), hydrochemistry and isotopic analyses (Chapter 4), hydraulic conductivity (Priebe et al. 2017), hydraulic head values (Chapter 4) and porosity values (Zheng 1999). Despite these constraints, significant sources of uncertainty remain such as the uncertainty in groundwater velocity estimates, which may very widely and affect residence times, as well as the spatial variability in the geochemistry of the

mineral assemblage, which was not accounted for. It is because of uncertainties such as these that the modeling objectives are broad and process oriented, with no recommendation for conducting predictive simulations.

Testing of the conceptual model with reactive transport modeling demonstrated that most geochemical, hydrochemical and isotopic processes throughout the flow system are well understood, though some field outliers remain unexplained. Armed with the awareness of these inconsistencies, the many lines of evidence offered here provide a comprehensive set of tools for interpreting groundwater flow systems. Established end members may be used as fingerprints, providing insight into recharge area delineation, flow zone continuity assessments and the identification of areas of older, more hydrochemically evolved water. An understanding of relative position within a groundwater flow system is essential information to land use planning and water resources management, in particular for recharge area protection. Because some outliers in the field observations deviate from the general trends expressed in the conceptual model for many of the parameters and processes, end members should be used with caution for these interpretations.

This investigation has demonstrated that reactive transport modeling is a suitable tool for assessing trends in regional-scale systems. The inclusion of a flow simulation, a component not available in commonly used chemical models, provides an additional constraint, requiring the hydrochemical processes to be assessed within the spatial and temporal scales of the groundwater flow system. Although the simulation results are difficult and perhaps inappropriate to verify for regional-scale systems, they are still useful for assessing the systems as whole. Poor simulation results serve to shed light on complexities needing further investigation. As suggested by Steefel and van Cappellen (1998) for field-scale investigations, reactive transport modeling is a good interpretive tool for understanding interactions among coupled processes in natural systems. The results of the present study indicate that reactive transport models are similarly useful at regional-scales. However, in karstic carbonate groundwater systems such as the present study area, where flowpaths vary in length and hydraulic connection and are characterized by samples that are widely spaced, reactive transport modeling objectives may need to be restricted to those that are broad and process-oriented.

Chapter 6
Conclusions and Recommendations

6.1 SUMMARY OF CONCLUSIONS

The first research theme of this thesis focussed on understanding spatial relationships between geology and hydraulic conductivity (*K*). The need for enhanced coverage of *K* values across the study area was highlighted while conducting an investigation into the geological controls on *K*. To address this need, a spatially extensive set of *K* values was developed from domestic well specific capacity tests using a simple transmissivity estimator, developed with the method described by Theis (1963) and Driscoll (1986). Several comparisons were made to assess if the *K* values from specific capacity tests (SC *K*) could be combined with a high-quality *K* dataset, derived from the analysis of carefully conducted slug and pumping tests, to form one large set of values.

Results show that the SC *K* values compare very well with the high-quality *K* values at the high end of the *K* range ($\geq 1x10^{-5}$ m/s), but not at the low end of the *K* range. This divergence in *K* trends between the two sets of values stems from the different purposes of the wells, with monitoring wells installed to assess conditions in all geologic formations, regardless of production capacity, and domestic supply wells only targeting formations with good water producing zones, i.e., higher *K* values. Results of a smaller scale comparison, conducted in a single geological formation, suggest that the two sets of *K* values are similar enough to be combined to study more detailed well-field scale trends. The approach presented in Chapter 2 provides groundwater practitioners with a simple and low-cost method for improving coverage of *K* datasets. Domestic well datasets, such as the Ontario example used in Chapter 2, are available in many jurisdictions across the world (e.g. State of California 2001; British Geological Survey 2017). These wells represent an untapped resource of hydraulic information that can be used as a low-cost data source for groundwater research investigations.

The enhanced spatial coverage of *K* values developed in Chapter 2 was applied directly to investigating several geological controls on *K* in the karstic carbonate bedrock formations of the study area. Results of this investigation demonstrate that there is not one single geological feature, or "controlling variable", that is associated with high-*K* zones in carbonates. Instead, high-*K* zones correlate with areas where conductive geological features (e.g. fractures near valleys, coarse textures, sequence stratigraphic breaks) have been subjected to dissolution enhancement through relatively long periods of geological history. For the main hydrostratigraphic unit of the City of Guelph area (Gasport Fm), the greatest probability of encountering areas of high *K* occurs where this bedrock unit is out-cropping or sub-cropping, where it

contains paleokarstic sequence stratigraphic breaks, and where it is deeply penetrated by bedrock valleys. The integration of a large set of *K* values with a detailed geological model that considers dissolution enhancement through time (Brunton 2009) has revealed why and where *K* varies spatially across the study area. These results support the selection of local water supply exploration targets as well as describing an approach to understanding the relationship between *K* and geology that can be applied in similar settings elsewhere.

The second research theme of this thesis has focussed on investigating various hydrochemical tracer and modeling tools for delineating regional-scale groundwater flow systems in karstic carbonate bedrock. Research within this theme was initiated with a large groundwater sampling campaign within the 8,000 km^2 study area, followed by an assessment of the utility various hydrochemical, geochemical and isotopic tracer tools. Sulphur isotopes in conjunction with the sulphate mineral equilibrium provided essential information because of the distinct differences in isotopic signatures and mineral equilibria between recent recharge and chemically evolved groundwater. Strontium isotopes were not as informative as they have been in non-glaciated carbonate settings (e.g., Banner and Hanson 1990; Uliana et al. 2007) because of the hydrochemical imprinting of the glacial overburden signature being carried into the carbonate bedrock groundwater. Redox sensitive parameters provided essential information about hydrochemical evolution under closed-system conditions. Tritium values assisted with spatial assessments of relative recharge timing to the carbonate aquifers and were particularly useful for providing insight within the context of the permeability and thickness of glacial sediment cover. Upon identifying the most useful tracer tools, these were used as lines of evidence supporting a conceptual model of recharge and hydrochemical evolution. Tracer tools that provided the most insight into groundwater conditions in this investigation are recommended for use for groundwater mapping initiatives in similar geologic settings. Maps showing recharge locations for the major hydrostratigraphic units can be used to better inform the management of groundwater resources and groundwater source protection (Chapter 4).

To test the conceptual model presented in Chapter 4, hydrochemical, isotopic and geochemical processes were simulated along a single, hypothetical 50 km groundwater flowpath within the 8000 km^2 study area using the reactive transport model MIN3P (Chapter 5). In general, the simulation provided a good approximation of the field observations in trend directions and concentration levels. Of the 16 components within the model, there was only trend direction disagreement between the simulated and observed values for dissolved magnesium. The poor approximation of dissolved magnesium identified an issue with how magnesium mineralogy was represented, and confirmed that further investigation into magnesium dynamics is required. With the exception of magnesium, the modelling results confirmed that the conceptual model of chemical processes, developed in Chapter 4, is accurate and comprehensive.

Although the modeling confirms that the general trends are well understood, many field outliers suggest that chemical processes in some areas remain unexplained. With the knowledge that outliers exist, the newly confirmed conceptual model may be applied with caution. Established chemical end members may therefore be used as fingerprints, providing insight into recharge area delineation, flow zone continuity assessments and the identification of areas of older, more hydrochemically evolved water. The successful simulation of such a long hypothetical groundwater flowpath also indicates that reactive transport modeling may be a suitable tool for regional-scale applications, as was demonstrated by others for well-field scale ones (Steefal and van Cappelan 1998). However, inconsistencies and uncertainty derived from poor spatial coverage of monitoring wells at the regional-scale must be acknowledged in the application of reactive transport modeling to these large areas.

6.2 RECOMMENDATIONS FOR FUTURE RESEARCH AND APPLICATIONS

Incorporating Improved Spatial Coverage and Understanding of K Distribution into Groundwater Flow Modeling

In Chapters 2 and 3, the spatial coverage of *K* was enhanced and the influence of several geological features on *K* were identified. These outcomes contribute to an improved understanding of *K* distribution in the geological context that guides the selection of future groundwater supply exploration targets. An untested application of the improved *K* coverage and spatial understanding is how it might serve to inform groundwater modeling efforts. The City of Guelph, comprising the majority of the 600 km^2 study area of Chapter 2, relies on a finite-element groundwater-flow model to simulate flow for municipal wellhead capture zone delineation, aquifer vulnerability assessments and water budget estimates (Grand River Source Protection 2015). Despite the model being described as very sensitive to changes in *K*, the most recent account acknowledges that the observed spatial variation in *K* is not well reflected in the model (Grand River Source Protection 2015). Future research should include the incorporation of new findings on K distribution and geological controls into the conceptual and numerical flow models, where appropriate. For any groundwater model, the complexity of the model should only reflect the elements necessary for describing the field conditions (Anderson et al. 1992), and this recommendation for future work should follow this advice. If the ideal balance between simplicity and complexity is struck, the inclusion of the improved understanding of *K* distribution and its geological controls should serve to improve simulations of groundwater flow.

Adding Chemical Tracer Tools to Refine Ontario's Recharge Area Mapping Approach for Source Water Protection

Recharge area mapping and recharge quantification are required components of the assessment phase of Source Water Protection planning, as legislated under the Clean Water Act (Ontario 2006, part 2: s.15). In the present study area, recharge quantity was estimated for Source Water Protection planning from baseflow in a calibrated storm-event surface water model (AquaResource Inc. 2009). Recharge area locations were distributed within the watershed based on the assumed hydraulic properties of the top 3 m of Quaternary sediments and the land cover (AquaResource Inc. 2009). The approach to recharge area delineation taken in Chapter 4 differs from that of Source Water Protection in the use of hydrochemical end members and the consideration of sediment thickness as well as its permeability. Although the Source Water Protection approach to recharge characterization provides a rigorous quantitative estimate, the actual locations where recharge is occurring could be improved by confirming them with empirical observations. Future research should include an assessment of how the hydrochemical and isotopic end members developed in Chapter 4 might be used to better map recharge areas for Source Water Protection, and if appropriate, how such empirical observations might be incorporated into the Source Water Protection assessment approach itself.

Applying and Testing New Groundwater Mapping Tools Across Ontario in Similar and Dissimilar Geological Settings

As mentioned in section 1.3 of the introduction to this thesis, the research presented here was funded by the Ontario Geological Survey with the aim of supporting the development of new groundwater mapping and characterization techniques that can be applied in carbonate bedrock settings across the province. The application of the approaches developed here; which comprise enhancing spatial distribution of K, defining geological controls on K, defining chemical tools for mapping recharge areas and regional-scale reactive transport modeling, to similar settings elsewhere in Ontario or beyond will require consideration of how the findings of this thesis are unique to the Niagara Escarpment study area itself. Future researchers might consider the testing of non-uniqueness and the further refining of mapping and characterization approaches that are suitable in key groundwater-dependant areas across Ontario.

References

Anderson MP, Woessner WW (1992) Applied Groundwater Modeling: Simulation of Flow and Advective Transport. Academic Press, London, UK. 381p.

Antoniou EA, Stuyfzand PJ, van Breukelen BM (2013) Reactive transport modeling of an aquifer storage and recover (ASR) pilot to assess long-term water quality improvements and potential solutions. Applied Geochemistry 35:173-186

Appelo CAJ, Drijver B, Hekkenberg R, de Jonge M (1998) Modeling in situ iron removal from groundwater. Ground Water 13(2): 811-817

AquaResource Incorporated (2009) Integrated Water Budget Report, Grand River Watershed, https://www.sourcewater.ca/en/source-protection-areas/resources/Documents/Grand/Grand_Reports_WaterBudget_2009.pdf,accessed March 2018.

Aravena R, Wassenaar LI (1993) Dissolved organic carbon and methane in a regional confined aquifer, southern Ontario, Canada: Carbon isotope evidence for associated subsurface sources. Applied Geochemistry, 8: 483-493.

Ardis AF, Barker RA (1993) Historical saturated thickness of the Edwards-Trinity aquifer system and selected contiguous hydraulically connected units, west-central Texas. United States Geological Survey, Water-resources Inventory Report 92-4125.

Armstrong DK, Carter TR (2010) The subsurface Paleozoic stratigraphy of southern Ontario; Ontario Geological Survey, Special Volume 7, 301p.

Baird AF, McKinnon SD (2007) Linking stress-field deflection to basement structures in southern Ontario: Results from numerical modelling, Tectonophysics, 432:89-100.

Bajc AF, Shirota J (2007) Three-dimensional mapping of surficial deposits in the Regional Municipality of Waterloo, southwestern Ontario. Ontario Geological Survey, Groundwater Resources Study 3, 42p.

Bajc AF, Dodge JEP (2011) Three-dimensional mapping of surficial deposits of the Brantford-Woodstock area, southwestern Ontario. Ontario Geological Survey, Groundwater Resources Study 10, 77p.

Bajc AF, Marich AS, Priebe EH, Rainsford DRB (2017) Evaluating the groundwater resource potential of the Dundas buried bedrock valley, southwestern Ontario: an integrated geological and hydrogeological case study. Canadian Journal of Earth Science, doi.org/10.1139/cjes-2016-0224.

Banks WD, Brunton FR (2017) Collaboration between Ontario Geological Survey, consultants and municipal staff results in discovery and development of a safe and sustainable bedrock groundwater supply for the Town of Shelburne, Southern Ontario, Canada, IAH Canada, GeoOttawa 2017 – 70 years of Canadian Geotechnics and Geosciences, p.1-6.

Banner JL, Hanson GN (1990) Calculation of simultaneous isotopic and trace element variations during water-rock interaction with applications to carbonate diagenesis. Geochimica et Cosmochimica Acta, 54(11):3123-3137.

Banner JL, Wassenburg GJ, Dobson PF, Carpenter AB, Moore CH (1989) Isotopic and trace element constraints on the origin and evolution of saline groundwater from central Missouri. Geochmica et Cosmochimica Acta 53:383-398.

Barnett PJ (1992) Quaternary Geology of Ontario. In: Thurston PC, Williams HR, Sutcliffe RH, Stott GM (ed) Geology of Ontario, Ontario Geological Survey, Special Volume 4, Part 2, p 1011-1090.

Bierschenk WH (1964) Determining well efficiency by multiple step-drawdown tests, International Association of Scientific Hydrology, publication no. 54, General Assembly of Berkeley, Commission of Subterranean Waters. P.493-507.

Bourdet D (2002) Well Test Analysis: The Use of Advanced Interpretation Models, Elsevier.

Bouwer H, Rice RC (1976) A slug test for determining hydraulic conductivity of unconfined aquifers with completely or partially penetrating wells, Water Resources Research, 12(3): 423-428.

Bradbury KR, Rothschild ER (1985) A computerized technique for estimating the hydraulic conductivity of aquifers from specific capacity data, Ground Water, 23(2): 240-246.

Brett CE (1995) Sequence stratigraphy, biostratigraphy and taphonomy in shallow marine environments, Palaois, 10:597-616.

Brett CE (1998) Sequence stratigraphy, paleoecology and evolution: biotic clues to responses in sea-level fluctuations, Palaios, 13: 241-262.

British Geological Survey (2017) National Well Record Archive https://www.bgs.ac.uk/research/groundwater/datainfo/NWRA.html, accessed September 2018.

Brons, F, Marting, VE (1961) The effect of restricted fluid entry on well productivity, J. Petrol. Technol., 13(2): 172-174.

Brown RH (1963) Estimating the transmissivity of an artesian aquifer from the specific capacity of a well, U.S. Geological Survey Water Supply Paper 1536-I, p.336-338.

Brown RM (1961) Hydrology of tritium in the Ottawa Valley. Geochemica et Cosmochimica Acta, 21:199-216.

Bruce Power (2017) 2016 Environmental monitoring program report B-REP-07000-00008. 310p.

Brunton FR, Belanger D, DiBiase S, Yungwirth G, Boonstra G (2007) Caprock carbonate stratigraphy and bedrock aquifer characterization of the Niagara Escarpment- City of Guelph Region, Southern Ontario. In: Proceedings of the 60th Canadian Geotechnical Conference and the 8th joint Canadian Geotechnical Society- International Association of Hydrogeologists conference, Canadian Geotechnical Society, Ottawa. p 371-377.

Brunton FR, Dodge JEP (2008) Karst of southern Ontario and Manitoulin Island, Ontario Geological Survey, Groundwater Resources Study 5.

Brunton FR (2009) Update of revisions to the Early Silurian stratigraphy of the Niagara Escarpment: integration of sequence stratigraphy, sedimentology and hydrogeology to delineate hydrogeologic units; *In* Summary of Field Work and Other Activities 2009, Ontario Geological Survey, Open File Report 6240, pp. 25-1 to 25-20.

Brunton FR, Brintnell C (2011) Final update of the Early Silurian stratigraphy of the Niagara Escarpment and correlation with subsurface units across southwestern Ontario and the Great Lakes Basin. In: Summary of field work and other activities 2011, Ontario Geological Survey. Open File Report 6270. p 30-1 to 30-11.

Brunton FR, Brintnell C, Jin J, Bancroft AM (2012) Stratigraphic architecture of the Lockport Group in Ontario and Michigan – a new interpretation of Early Silurian 'Basin Geometries' & 'Guelph Pinnacle Reefs'. In: The 51st Annual Conference – Ontario-New York Oil & Gas Conference, Oct. 23-25th, 2012, Niagara Falls, Ontario. p 1-37.

Burt, AK, Dodge JEP (2016) Three-dimensional modelling of surficial deposits in the Orangeville–Fergus area of southern Ontario, Ontario Geological Survey, Groundwater Resources Study 15.

Burt AK, Dodge JEP (2017) Three-dimensional hydrostratigraphy of the Orangeville Moraine area, southwestern Ontario, Canada. Canadian Journal of Earth Sciences, dx.doi.org/10.1139/cjes-2017-0077.

Busenberg E, Plummer NL (1982) The kinetics of dissolution of dolomite in CO_2*H_2O systems at 1.5 to 65 degrees Celsius and 0 to 1 atm Pco2. American Journal of Science, 282:45-78.

Butler JJ Jr. (1998) The Design, Performance and Analysis of Slug Tests. Lewis Publishers, A CRC Press Company.

Champ DR, Gulens J, Jackson RE (1979) Oxidation-reduction sequences in ground-water flow systems. Canadian Journal of Earth Science 16(1): 12-23.

Chapman LJ, Putnam DF, (1984) The physiography of southern Ontario. Third Edition Ontario Geological Survey Special Volume 2, 270p.

Chilingarian GV, Chang J, Bagrintseva KI (1990) Empirical expression of permeability in terms of porosity, specific surface area, and residual water saturation of carbonate rocks. Journal of Petroleum Science and Engineering, 4:317-322.

Chen Z, Auler AS, Bakalowicz, Drew D, Griger F, Hartmann J, Jiange G, Moosdorf M, Richts A, Stevanovic Z, Veni G, Goldscheider N (2017) The World Karst Aquifer Mapping project: concept, mapping procedure and map of Europe. Hydrogeology Journal, 25: 771-785.

Chou L, Garrels RM, Wollast R (1989) Comparative study of the kinetics and mechanisms of dissolution of carbonate minerals. Chemical Geology 78:269-282

Clark ID, Fritz P (1997) Environmental isotopes in hydrogeology. CRC Press, New York.

Claypool GE, Holser WT, Kaplan IR, Sakai H, Zak I (1980) The age curves of sulphur and oxygen isotopes in marine sulphate and their mutual interpretation. Chemical Geology 28:199-260.

Cole J, Coniglio M, Gautrey S (2009) The role of buried bedrock valleys in the development of karstic aquifers in flat-lying carbonate bedrock: insights from Guelph, Ontario, Canada, Hydrogeology J. doi: 10.1007/s10040-009-0441-3.

Conservation Ontario 2017 http://conservationontario.ca/standalone/flood-find/southwestern.html, accessed September 26, 2017.

Cooke ML, Simo JA, Underwood CA, Rijken, P (2006). Mechanical stratigraphic controls on fracture patterns within carbonates and implications for groundwater flow, Sedimentary Geology 184: 225 – 239.

Cooper HH, Jacob CE (1946) A generalized method for evaluating formation constants and summarizing well field history, American Geophysical Union Transactions, 27: 526-534.

Cooper HH, Bredehoeft JD, Papadopulos IS (1967) Response of a finite-diameter well to an instantaneous charge of water, Water Resources Research, 3(1): 263- 269.

Cowan WR, Sharpe DR, Feenstra BH, Gwyn QHJ (1978) Glacial geology of the Toronto-Owen Sound area; in Toronto ’78 Field Trips Guidebook for a Joint Meeting of the Geological Society of America, Geological Association of Canada and Mineralogical Association of Canada,16p.

Craig H (1961) Isotopic variations in meteoric waters. Science, 133:1702-1703.

Cramer BD, Brett CE, Melchin MJ, Mannik P, Kleffner MA, Mclaughlin PI, Loydell DK, Munnecke A, Jeppsson L, Corrandini C, Brunton FR, Saltzman MR (2011) Revised correlation of Silurian provincial series of North Americal with global and regional chronostratigraphic units and 13C chemostratigraphy. Lethaia, DOI 10.1111/j.1502-3931.2010.00234.x.

Cunnane C (1978) Unbiased plotting positions- a review, Journal of Hydrology 35: 205-222.

Davies JL, Williams MAJ (1978) Interpretation of Australasian Karsts *in*: Landform evolution in Australasia, ANU Press, pp. 259-286.

Di Biase S, Petrie J (2009) Guelph Waterworks Groundwater Monitoring System, an unpublished private consulting report by Golder Associates Ltd., prepared for the Waterworks Division of the City of Guelph. p 324.

Di Biase S, Donald S, Cichocki A, Petrie J (2006) Additional Groundwater Supplies: The Guelph Lime Project; unpublished private consulting report by Golder Associates Ltd., prepared for the Waterworks Division of the City of Guelph. p 74.

Dollar PS, Frape SK, McNutt RH, (1991) Geochemistry of formation waters Southwestern Ontario, Canada and Southern Michigan USA: Implications for Origin and Evolution. Ontario Geological Survey, Ontario Geoscience Research Grant Program, Grant No. 249, Open File Report 5734, 72p.

Drever JI (1988) The geochemistry of natural waters, second edition, Prentice Hall, New Jersey.

Dreybrodt, W (1996) Principles of early development of karst conduits under natural and man-made conditions revealed by mathematical analysis of numerical models, Water Resources Research 32(9): 2923-2935.

Driscoll FG (1986) Groundwater and Wells, 2nd edition. Johnston Screens, Minnesota.

Eagon HB Jr., Johe DE (1972) Practical solutions for pumping tests in carbonate-rock aquifers, Ground Water 10(4): 6-13.

Edmunds WM, Walton NGR (1983) The Linconshire limestone- hydrogeochemical evolution over a ten year period, Journal of Hydrology 61: 201-211.

El-Kadi AI, Plummer LN, Aggarwal P (2010) NETPATH-WIM: An interactive user version of the mass-balance model, NETPATH. Ground Water, doi:10.111/j.1745-6584.2010.00779.x

El-Naqa A (1994) Estimation of transmissivity from specific capacity data in fractured carbonate rock aquifer, central Jordan, Environmental Geology 23: 73-80.

Ettensohn FR (1994) Tectonic control on formation and cyclicity of major Appalachian unconformities and associated stratigraphic sequences. Concepts in Sedimentology and Paleontology, 4(2): 17-242.

Ettensohn FR, Brett CE (1998) Tectonic components in Silurian cyclicity: examples from the Appalachian Basin and global implications; *in* Silurian Cycles: Linkages of dynamic stratigraphy with atmospheric, oceanic and tectonic changes, New York State Museum Bulletin 491, p.245-156.

Eyles N, Boyce J, Mohajer AA (1993) The bedrock surface of the western Lake Ontario region: evidence of reactivated basement structures, Géographie Physique et Quaternaire. 47(3): 269-283.

Eyles N, Scheidegger AE (1995) Environmental significance of bedrock jointing in southern Ontario, Canada, Environmental Geology 26:269-277.

Eyles N, Arnaud E, Scheidegger AE, Eyles CH (1997) Bedrock jointing and geomorphology in southwestern Ontario, Canada: an example of tectonic predesign, Geomophology 19: 17-34.

Ferguson HF, Hamel JV (1981) Valley stress relief in flat-lying sedimentary rocks: in Proceedings of the International Symposium on Weak Rock, Tokyo, p.1235-1240.

Ford DC (1983) Karstic interpretation of the Winnipeg Aquifer (Manitoba, Canada). Journal of Hydrology 61: 177-180.

Ford D (1987) Effects of glaciations and permafrost upon the development of karst in Canada, Earth Surface Processes and Landforms, 12: 507-521.

Freeze AR, Cherry JA (1979) Groundwater. Prentice Hall, New Jersey, pp.604.

Fritz P, Drimmie RJ, Frape SK and O'Shea O (1987) The isotopic composition of precipitation and groundwater in Canada. In Isotope techniques in water resources development, International Atomic Energy Agency, Symposium 299, March 1987, Vienna, Austria, pp.539-550.

Fritz P, Basharmal GM, Drimmie RJ, Ibsen J, Qureshi RM (1989) Oxygen isotope exchange between sulphate and water during bacterial reduction of sulphate, Chemical Geology: Isotope Geoscience Section 79: 99-105.

Funk G (1979) Geology and water resources of the East and Middle Oakville Creeks IHD representative drainage basin, Water Resources Report 12, Ontario Ministry of the Environment, 89p.

Funk G (2009) Arkell Spring Grounds Hydrogeological Study, unpublished, private consulting report prepared by AECOM Canada Ltd. for the City of Guelph. p 102.

Gao C, Shirota J, Kelly RI, Brunton FR, Van Haaften S (2006) Bedrock Topography and Overburden Thickness Mapping, Southern Ontario, Ontario Geological Survey, Miscellaneous Release—Data 207.

Gao C (2011) Buried bedrock valleys and glacial and subglacial meltwater erosion in southern Ontario, Canadian Journal of Earth Sciences. doi:10.1139/E10-104.

Gat JR, Bowser CJ, Kendall C (1994). The contribution of evaporation from the Great Lakes to the continental atmosphere: estimate based on stable isotope data. Geophysical Research Letters, 21 (7): 557-560.

Gautrey SJ (2004). Evidence to support pre or early Wisconsinan genesis of a productive karst system beneath the City of Guelph; in Geological Association of Canada–Mineralogical Association of Canada, Joint Annual Meeting – Lake-to-Lake, Brock University, St. Catharines, ON. p 29.

Gibson B, Amos RT, Blowes DW (2010) Reactive transport modeling of isotope fractionation in permeable reactive barriers. Environmental Science and Technology 45:2863-2870.

Grand River Source Protection (2015) Chapter 8: Guelph Region, Approved Assessment Report (https://www.sourcewater.ca/en/source-protection-areas/resources/Documents/Grand/Feb2017_GRSPA_Updated-AR_Sections8_s51_clean.pdf) 100p., accessed November 2018.

Grasby SE, Betcher RN (2002) Regional hydrogeochemistry of the carbonate rock aquifer, southern Manitoba. Canadian Journal of Earth Science 39: 1053-1063.

Grassineau NV, Mattey DP, Lowry D (2001) Sulfur isotope analysis of sulfide and sulfate minerals by continuous flow-isotope ratio mass spectrometry. Analytical Chemistry, 73(2): 220-225.

Grey-Sauble Conservation Authority (2015) Saugeen, Grey Sauble, Northern Bruce Peninsula Source Protection Region, Conceptual Water Budget, http://home.waterprotection.ca/wp-content/uploads/2017/03/2008_02_Final-Draft-Conceptual-Water-budget.pdf, accessed March 2018.

Greenhouse JP, Karrow PF (1994) Geological and geophysical studies of buried valleys and their fills near Elora and Rockwood, Ontario, Canadian Journal of Earth Sciences 31: 1838-1848.

Gross MR, Engelder T (1991) A case for neotectonic joints along the Niagara Escarpment, Tectonics, 10:631-641.

Halford KJ, Weight WD, Schreiber, RP (2006) Interpretation of transmissivity estimates from single-well pumping aquifer tests, Ground Water 44(3): 467-471.

Hamilton, SM 2015. Ambient groundwater geochemistry data for southern Ontario, 2007-2014; Ontario Geological Survey, Miscellaneous Release – Data 283-- Revised.

Hantush MS (1964) Hydraulics of wells, Advances in Hydroscience 1: 281-433.

Hardie LA (1987) Dolomitization: a critical view of some current views. Journal of Sedimentary Petrology, 57:166-183

Helsel DR, Hirsch RM (1992) Statistical methods in water resources. Elsevier, Amsterdam, the Netherlands.

Horwitz EP, Gale NH (1994) A lead selective extraction chromatographic resin and its application to the isolation of lead from geological samples, Analytical Chimica Acta, 292: 263-273.

Hostetler PB (1964) The degree of saturation of magnesium and calcium carbonate minerals in natural waters: International Association of Scientific Hydrology, Commission of Subterranean Waters Publication 64:34-49.

Huntley D, Nommensen R, Steffey D (1992) The use of specific capacity to assess transmissivity in fractured-rock aquifers, Ground Water 30(3): 396-402.

International Atomic Energy Association (IAEA) 2015 Global Network of Isotopes in Precipitation, Water Isotope System for Data Analysis portal, https://nucleus.iaea.org/Pages/GNIPR.aspx, accessed October 2017.

Inskeep WP, Bloom PR (1985) An evaluation of rate equation for calcite precipitation kinetics at $_{P}CO_2$ less than 0.01 atm and pH greater than 8. Geochimica et Cosmochimica Acta, 49:2165-2180.

Jacob CE (1946) Drawdown test to determine effective radius of artesian well, Transactions, American Society of Engineers 112(2321): 1047-1064.

Jambor JL, Dutrizac JE (1998) Occurrence and constitution of natural and synthetic ferrihydrite, a widespread iron oxyhydroxide. Chemical Reviews (98) 2549-2585.

Jiminez-Madrid A, Castano S, Vadillo I, Martinez C, Carrasco F, Soler A (2017) Applications of hydro-chemical and isotopic tools to improve definitions of groundwater catchment zones in a karstic aquifer: A case study, Water, doi:10.3390/w9080595.

Karrow PF (1973) Bedrock topography in southwestern Ontario: a progress report; Geological Association of Canada, Proceedings 25, 67-77, Geological Society of America Bulletin 79, 889-910.

Katz BG, Lee TM, Plummer NL, Busenberg E (1995a) Chemical evolution of groundwater near a sinkhole lake, northern Florida, 1. Flow patterns, age of groundwater, and influence of lake water leakage, Water Resources Research 31: 1549-1564.

Katz BG, Plummer NL, Busenberg E, Revesv KM, Jones BF, Lee TM (1995b) Chemical evolution of groundwater near a sinkhole lake, northern Florida, 2. Chemical patterns, mass transfer modeling, and rates of mass transfer reactions, Water Resources Research 31: 1565-1584.

Katz BG, Eberts SM, Kauffman LJ (2011) Using Cl/Br ratios and other indicators to assess potential impacts on groundwater quality from septic systems: A review and examples from principal aquifers in the United States, Journal of Hydrology, 397: 151-166.

Keller, C, Cherry JA, Parker, BL (2014) New method for continuous transmissivity profiling in fractured rock, Ground Water 52 (3): 352-367.

Krothe NC, Libra RD (1983) Sulfur isotopes and hydrochemical variations in spring waters of southern Indiana, Journal of Hydrology, 61: 267-283.

Kunert M, Coniglio M, Jowett EC (1998) Controls and age of cavernous porosity in Middle Silurian dolomite, southern Ontario, Canadian Journal of Earth Sciences 35: 1044–1053.

Lee VL, Priebe EH, Brunton FR, Piersol J, Monier-Williams M, Pendleton B, Bingham M, Keller C, Sharpe I (2011) Bedrock aquifer mapping of the Niagara Escarpment cuesta: installation and sampling of multi-level monitoring wells; In Summary of Field Work and Other Activities 2011, Ontario Geological Survey, Open File Report 6270, pp.31-1 to 31-6.

Li XD, Liu CQ, Harue M, Li SL, Lio XL (2010) The use of environmental isotopic (C,Sr,S) and hydrochemical tracers to characterize anthopogenic effects on karst groundwater quality: A case study of the Shuicheng Basin, SW China, Applied Geochemistry 25: 1924-1936.

Lucia FJ (1983) Petrophysical parameters estimated from visual descriptions of carbonate rocks: a field classification of carbonate pore space, Journal of Petroleum Technology, March: 626-637.

Mace RE (1997) Determination of transmissivity from specific capacity tests in a karst aquifer, Ground Water 35(5): 738-742.

MacGregor K (1976) Caves of Ontario; Cave Exploration in Canada – A special issue, Canadian Caver Magazine. p. 39-54.

MacRitchie SM, Pupp C, Grove G, Howard KWF, Lapcevic P (1994) Groundwater in Ontario: hydrogeology, quality concerns and management; Environment Canada, NHRI Contribution No. CS-94011:117p.

Majoube M (1971) Fractionation of oxygen-18 and deuterium in water and its vapour. Journal of Chemical Physics 197:1423-1436

Matrix Solutions Incorporated (2014) City of Guelph tier three water budget and local area risk assessment, appendix B, groundwater flow model report, prepared for Lake Erie Source Protection Region, unpublished consulting report: p.96.

Mayer KU, Frind EO, Blowes DW (2002) Multicomponent reactive transport modeling in variably unsaturated porous media using a generalized formulation for kinetically controlled reactions. Water Resources Research 38(9): 13-1 to 13-21.

McNutt RH, Frape SK, Dollar P (1987) A strontium, oxygen and hydrogen isotopic composition of brines, Michigan and Appalachian Basins, Ontario and Michigan, Applied Geochemistry 2: 495-505.

Meier, PM, Carrera, J, Sanchez-Vila, X (1998) An evaluation of Jacob's method for the interpretation of pumping tests in heterogeneous formations; Water Resources Research 34(5):1011-1025.

Meyer JR, Parker BL, Arnaud E, Runkel AC (2016) Combining high resolution vertical gradients and sequence stratigraphy to delineate hydrogeologic units for a contaminated sedimentary rock aquifer system, Journal of Hydrology 534: 505 – 523.

McLaughlin PI, Brett CE, Wilson MA (2008) Hierarchy of sedimentary discontinuity surfaces and condensed beds fromt eh middle Paleozoic of eastern north America: implications for cratonic sequence stratigraphy, in Dyanamics of Epeiric Seas, Geological Association of Canada, Special Paper 48.

Michalski A, Britton R (1997) The Role of Bedding Fractures in the Hydrogeology of Sedimentary Bedrock-Evidence from the Newark Basin, New Jersey, Groundwater 35(2): 318 -327.

Muldoon MA, Simo JJ, Bradbury KR (2001) Correlation of hydraulic conductivity with stratigraphy in a fractured-dolomite aquifer, northeastern Wisconsin, USA, Hydrogeology J., 9: 570 – 583.

Nancollas GH, Reddy MM (1971) The crystallization of calcium carbonate, II. Calcite growth mechanism. Journal of Colloid Interface Science, 37:824-829.

National Research Council. 1996. Rock Fractures and Fluid Flow: Contemporary Understanding and Applications. Washington, DC, The National Academies Press. p 568.

Neuman SP (1982) Statistical characterization of aquifer heterogeneities: an overview, in Narasimhan, T.N., ed., Recent trends in hydrogeology: Boulder, Colorado, Geological American Geophysical Union, Society of America Special Paper 189, 16: 519-524.

O'Connor DR (2002) Part I, Report of the Walkerton Inquiry: The Events of May 2000 and Related Issues. Queen's Printer for Ontario.

Ontario Geological Survey (2010) Surficial geology of southern Ontario; Ontario Geological Survey, Miscellaneous Release— Data 128 – Revised.

Ontario (1996) Procedure D-5-5: Technical Guideline for Private Wells: Water Supply Assessment, https://www.ontario.ca/document/d-5-5-private-wells-water-supply-assessment , accessed June, 2017.

Ontario (2003) Ontario Water Resources Act, Regulation 903: Wells, as amended by R.S.O. 2007, 2009, 2010, 2013, 2014.

Ontario (2006) Clean Water Act https://www.ontario.ca/laws/statute/06c22 , accessed November 2018.

Ontario (2015) Chapter 13: Well Records, Documentation, Reporting and Tagging; in Water Supply Wells- Requirements and Best Management Practices, Ministry of Environment and Climate Change. https://dr6j45jk9xcmk.cloudfront.net/documents/4970/m-wwbmp-chapter-13-well-records-april-2015.pdf, accessed March 2018.

Ontario (2017a) https://www.ontario.ca/page/source-protection, Ministry of Environment and Climate Change, accessed September 15, 2017.

Ontario (2017b) https://news.ontario.ca/ene/en/2017/01/ontario-taking-next-step-to-protect-water-resources.html, Ministry of Environment and Climate Change news release, accessed October 2017.

Panton JH (1889) The caves and potholes at Rockwood, Ontario, In: Proceedings of the Canadian Institute, third series (6): 244-253.

Parkhurst DL, Appelo CAJ (1999) User's guide to PHREEQC—A computer program for speciation, reaction-path, 1D-transport, and inverse geochemical calculations, US Geological Survey Water Resources Investigation Report 99-4259, 312p

Perrin J, Parker BL, Cherry JA (2011) Assessing the flow regime in a contaminated fractured and karstic dolostone aquifer supplying municipal water, Journal of Hydrology 400: 396 – 410.

Person M, McIntosh J, Bense V, Remenda VH (2007) Pleistocene hydrology of north America: the role of ice sheets in reorganizing groundwater flow systems. Reviews of Geophysics 45, RG3007, doi:10.1029/2006RG000206.

Piersol J, Petrie J (2011) City of Guelph Tier III Assessment Characterization and Final Report, Appendix A; https://www.sourcewater.ca/en/source-protection-areas/resources/Documents/Grand/GGET-Tier-Three-Risk-Assessment---Appendix-A-A_2017_03.pdf Golder Associates Limited. p 66. Plummer LN (1977) Defining reactions and mass transfer in part of the Floridan Aquifer. Water Resources Research, 13: 801-812.

Plummer LN, Wigley TML, Parkhurst DL (1978) The kinetics of calcite dissolution in CO2-water system at 5 to 60 degrees C and 0.0 to 1.0 atm CO2. American Journal of Science, 278:179-216

Plummer LN, Wigley TML (1976) The dissolution of calcite in CO2-saturated solution at 25 degrees C and 1 atmosphere total pressure. Geochemica et Cosmochimica Acta, 40: 191-201

Priebe EH, Brunton FR (2016) Regional-scale groundwater mapping in the early Silurian carbonates of the Niagara Escarpment: Final update: in Summary of Field Work and Other Activities, 2016, Ontario Geological Survey, Open File Report 6323, p.29-1 to 29-10.

Priebe EH, Lee VL (2016) Groundwater hydrochemistry data for multi-depth well sampling in the Early Silurian carbonates of the Niagara Escarmpent cuesta; Ontario Geological Survey, Miscellaneous Release—Data 337

Priebe EH, Neville CJ, Brunton FR (2017a), Discrete, high-quality hydraulic conductivity estimates for the Early Silurian carbonates of the Guelph region, Ontario Geological Survey, Groundwater Resources Study 16.

Priebe EH, Neville CJ, Rudolph DL (2017b) Enhancing the spatial coverage of a regional high-quality hydraulic conductivity dataset with estimates made from domestic water-well specific-capacity tests. Hydrogeology Journal, 26:395-406.

Priebe EH, Brunton FR, Rudolph DL, Neville CJ (2018) Geological controls on hydraulic conductivity distribution in a karst-influenced carbonate bedrock groundwater system, southern Ontario, Canada. *in press* at Hydrogeology Journal.

Prommer H, Stuyfzand PJ (2005) Identification of temperature-dependent water quality changes during a deep well injection experiment in a pyritic aquifer. Environmental Science and Technology 39: 2200-2209

Prudic DE (1991) Estimates of hydraulic conductivity from aquifer-test analyses and specific-capacity data, Gulf Coast Regional Aquifer Systems, South-Central United States, USGS Water-Resources Investigations Report 90-4121.

Quackenbush, P. and Gemin, J. 2014. The Corporation of the City of Guelph Water Supply Master Plan Update, http://guelph.ca/wp-content/uploads/RPT-2014-05-29-GuelphWSMP-60287843-DraftFinalCOMPLETEREPORTwithAPPENDICES.pdf AECOMCanada Limited and Golder Associates Limited, accessed January 2017.

Razack M, Huntley D (1991) Assessing transmissivity from specific capacity in a large and heterogeneous alluvial aquifer, Ground Water 29(6): 856-861.

Rivera A (2013) Canada's Groundwater Resources, Fitzhenry and Whiteside Limited.

Rovey CW, Cherkauer DS (1994a) Relation between hydraulic conductivity and texture in a carbonate aquifer: observations, Groundwater 32(2): 53-62.

Rovey CW, Cherkauer DS (1994b) Relation between hydraulic conductivity and texture in a carbonate aquifer: Regional continuity, Groundwater 32(2): 227-238.

Rowell, D.J. 2015. Aggregate and industrial mineral potential of the Guelph Formation, southern Ontario; Ontario Geological Survey, Open File Report 6307, 66p.

Schlager W (2005) Carbonate sedimentology and sequence stratigraphy, Society for Sedimentary Geology, Concepts in Sedimentoloty and Paleontology No. 8, p.208.

SciVal (2011) Confronting the global water crisis through research, https://www.elsevier.com/__data/assets/pdf_file/0018/53082/Water-Resources_WP_lr.pdf, accessed March 2018.

Seibert S, Descourviers C, Skrzypek G, Deng H, Prommer H (2012) Model-based analysis of ^{34}S signatures to trace sedimentary pyrite oxidation during managed aquifer recharge in a heterogeneous aquifer. Journal of Hydrology, 548:368-381.

Seibert S, Atteia O, Salmon SU, Siade A, Douglas G, Prommer H (2016) Identification and quantification of redox and pH buffering processes in a heterogeneous, low carbonate aquifer during managed aquifer recharge. Water Resources Research 52:4003-4025

Shafer W (2001) Predicting natural attenuation of xylene in groundwater using a numerical model. Journal of Contaminant Hydrology, 52:57-83

Sharpe DR, Piggot A, Carter TR, Gerber RE, MacRitchie SM, de Loe R, Strynatka S, Zwiers G (2013) Chapter 12: Southern Ontario Hydrogeological Region in Canada's Groundwater Resources, Fitzhenry & Whiteside, Canada, 804p.

Sibson R (1981) A brief description of natural neighbour interpolation, Chapter 2 in Interpolating Multivariate Data. John Wiley & Sons, New York, pp.21-36.

Sibul, U., Walmsley, D., Szudy, R. 1980. Groundwater resources in the Grand River Basin; Technical Report 10, Ontario Ministry of The Environment, 200p.

Sillen LG, Martell, AE (1964) Stability constants of metal-ion complexes: Chemical Society [London] Special Publication 754p.

Singer SN, Cheng CK, Scafe MG (2003) The hydrogeology of southern Ontario, second edition, Environmental Monitoring and Reporting Branch, Ontario Ministry of the Environment, https://archive.org/details/hydrogeologyofso00snsiuoft.

Singer SN, Cheng CK, Scafe MG (2003) The Hydrogeology of Southern Ontario, Second Edition. Environmental Monitoring and Reporting Branch, Ontario Ministry of the Environment, 200p.

Singhal BBS, Gupta RP (2010) Applied Hydrogeology of Fractures Rocks, 2nd Edition, Springer.

Straw A (1968) Late Pleistocene glacial erosion along the Niagara Escarpment of southern Ontario. Geological Society of America Bulletin, 79: 889–910. doi:10.1130/0016-7606(1968)79[889:LPGEAT]2.0.CO;2.

State of California (2001) How to fill out a well completion report, Department of Water Resources, http://www.water.ca.gov/pubs/groundwater/how_to_fill_out_a_well_completion_report/wcr_instruction_pamphlet_2_.pdf , accessed June, 2017.

Steefel CI, van Cappellen PV (1998) Reactive transport modeling of natural systems. Journal of Hydrology, 209:1-7.

Sun RJ, Weeks JB, Grubb HF (1997) Bibliography of the Regional Aquifer-System Analysis Program of the US Geological Survey, 1978-1996, Water Resources Investigation, https://water.usgs.gov/ogw/rasa/html/introduction.html

Taylor CB (1977) Tritium enrichment of environmental waters by electrolysis: development of cathodes exhibiting high isotopic separation and precise measurement of tritium enrichment factors. Proceedings of the International Conference of Low-Radioactivity Measurements and Applications, Slovenski Pedagogicke Nakladatelstvo, Bratislava: pp.131-40.

Theis CV (1935) The relation between the lowering of the piezometric surface and the rate and duration of discharge of a well using groundwater storage, American Geophysical Union. 16: 519-524.

Theis CV (1963) Estimating the transmissivity of a water-table aquifer from specific capacity of a well, U.S. Geological Survey Water Supply Paper 1563-I: 332-336.

Toran L, Harris RF (1989) Interpretation of sulphur and oxygen isotopes in biological and abiological sulfide oxidation. Geochimica et Cosmochimica Acta, 53: 2341-2348.

Toth DJ, Katz BG (2006) Mixing of shallow and deep groundwater as indicated by the chemistry and age of karstic springs. Hydrogeology Journal, 14(6):1060-1080.

Uliana MM, Banner JL, Sharp JM Jr. (2007) Regional groundwater flow paths in Trans-Pecos, Texas inferred from oxygen, hydrogen, and strontium isotopes. Journal of Hydrology, 334:334-336.

Vail PR, Audemard E Bowman SA, Eisner PN, Perez-Cruz C (1991) The stratigraphic signatures of tectonics, eustasy and sedimentology--an overview. In Cycles and Events in Stratigraphy, ed. G Einsele, W Ricken, A Seilacher, pp. 617-59, Springer-Verlag.

van Cappellen P, Gaillard JF (1996) Biogeochemical dynamics in aquatic sediments. Reviews in Minerals and Geochemistry 34(1):335-376.

Walker RG, James NP (1992) Facies models: Response to sea level change. Geological Association of Canada, 409p.

Walton WC (1962). Selected analytical methods for well and aquifer evaluation, Illinois State Water Survey 49, p 91.

Watson DF, Philip GM (1985) A refinement of inverse distance weighted interpolation, Geoprocessing, 2:315–327.

Weber JN (1960) Ontario underground, Canadian Geographical Journal, 62(2):42-51.

White OL,Karrow PF (1971) New evidence for Spencer's Laurentian River. Proceedings of the 14th Conference of Great Lakes Research, pp. 394–400.

Wilde FD, Radtke DB, Gibs J, Iwatsubo RT (1998) National field manual for the collection of water-quality data: US Geological Survey Techniques of Water-Resources Investigations, book 9, chap. A-6.

Williamson MA, Rimstidt JD (1994) The kinetics and electrochemical rate-determining step of aqueous pyrite oxidation. Geochimica et Cosmochimica Acta 58(24): 5443-5454

Wyrick, GG, Borchers JW (1981) Hydrologic effects of stress-relief fracturing in an Appalachian Valley. United States Geological Survey, Water-Supply Paper 2177, 53p.

Xie X, Wang Y, Ellis A, Su C, Li J, Li M, Duan M (2013) Delineation of groundwater flow paths using hydrochemical and strontium isotope composition: A case study in high arsenic aquifer systems of the Datong basin, northern China. Journal of Hydrology, 476:87-96.

Younger PL (1993) Simple generalized methods for estimating aquifer storage parameters, Quarterly Journal of Engineering Geology 26:127-135.

Zheng Q (1999) Carbonate diagenesis and porosity evolution in the Guelph Formation, southwestern Ontario; unpublished PhD thesis, University of Waterloo, Ontario, 265p.

Zoback ML (1992) First- and second-order patterns of stress in the lithosphere. J. Geophys. Res., 97: 11,703-l 1,728 and map.